

**NEUROLOGICAL DISEASE DIAGNOSIS AND TREATMENT VIA PRECISE
ROBOTIC INTERVENTION**

A Dissertation
Presented to
The Academic Faculty

By

Waiman Meinhold

In Partial Fulfillment
of the Requirements for the Degree
Doctor of Philosophy in Robotics
Woodruff School of Mechanical Engineering

Georgia Institute of Technology

August 2021

© Waiman Meinhold 2021

**NEUROLOGICAL DISEASE DIAGNOSIS AND TREATMENT VIA PRECISE
ROBOTIC INTERVENTION**

Thesis committee:

Dr. Jun Ueda
Mechanical Engineering
Georgia Institute of Technology

Dr. Frank Hammond
Mechanical Engineering
Georgia Institute of Technology

Dr. Jaydev Desai
Biomedical Engineering
Georgia Institute of Technology

Dr. Ai-Ping Hu
GTRI
Georgia Institute of Technology

Dr. Mehmet Kurt
Mechanical Engineering
Stevens Institute of Technology

Dr. John Oshinski
Radiology and Imaging Sciences
Emory University

Date approved: May 13, 2021

I believe that I am not saying anything to my colleagues that is startlingly new, most of them are familiar with this phenomenon.

Wilhelm Erb , 1875

For my wife Terra.

ACKNOWLEDGMENTS

The success of the work reported here is undoubtedly due to the mentorship of my advisor, Dr. Jun Ueda. His enthusiasm and guidance enabled not only the results contained in the following pages, but also my personal development as a researcher.

I would like to thank the members of my thesis committee for their help in preparation of this work, both for contributions informing the direction as well as material support in the form of laboratory equipment and imaging facility connections.

A particular debt of gratitude is owed to each of the members of the Biorobotics and Human Modeling Laboratory, former and present. This work would not have been possible without the help of each and every one of them.

Many collaborators played essential roles in the completion of various parts of this work. Efe Ozkaya worked closely in the evaluation of the MRE actuators, carrying out many of the MRI experiments. Joseph Lee and Siyu Li wrote the VR visualization code for the MRI guided robot interface. Daniel Martinez wrote the super resolution positioning code and carried out many of the benchtop and MRI experiments.

I would also like to thank my parents for the role they have played in offering encouragement and advice. Simply put, this work would not exist without their guidance and support.

I gratefully acknowledge the support for this work offered by the National Science Foundation under grant numbers 1662029 and 1545287, and by the CDMRP under PR192452. Any views and conclusions contained herein are those of the author, and do not necessarily represent the official positions, express or implied, of the funders.

TABLE OF CONTENTS

Acknowledgments	v
List of Tables	xi
List of Figures	xii
Summary	xix
Chapter 1: Introduction	1
1.1 Aims	1
1.1.1 Aim 1 - Enhanced neurological diagnosis and treatment via improved peripheral stimulation methods	1
1.1.2 Aim 2 -Development of a new robot morphology for high resolution intervention in the spinal cord	1
1.1.3 Aim 3 - Development of a novel magnetic resonance elastography actuator and positioning system	2
1.2 Motivation	2
Chapter 2: Aim 1: Enhanced neurological diagnosis and treatment via improved peripheral stimulation methods	5
2.1 Introduction	5
2.2 Location detection	5
2.2.1 Frequency content of hammer acceleration	6

2.2.2	Mechanical models for location detection	9
2.2.3	Spring-damper model	9
2.2.4	Hertz contact model	10
2.2.5	Tapping device	12
2.2.6	Model results	13
2.2.7	Learned models for location detection	16
2.2.8	SVM classifier	17
2.3	Human performance in DTR elicitation	18
2.3.1	Automated tapping experiments	19
2.3.2	Human operator experiments	21
2.3.3	Human and robotic stimulation variability	21
2.3.4	Hammer velocity measurement and tapping energy calculation	22
2.3.5	Tapping tension force	23
2.3.6	Expert and novice stimulation intensity variability	23
2.3.7	Timing evaluation	26
2.4	Diagnostic uses of the DTR	29
2.4.1	Layperson grading	30
2.4.2	Tapping assistance application	33
2.4.3	Tendon hammer design and evaluation	34
2.4.4	Materials cost and distribution	36
2.4.5	Application design and functionality	37
2.5	Therapeutic uses of tendon tapping	37
2.5.1	Paired response therapies	38

2.5.2	SSEP modulation	40
2.6	Aim 1 discussion	43
2.7	Future work	44
2.7.1	Alternative models	44
Chapter 3: Aim 2: Development of a new robot morphology for high resolution intervention in the spinal cord		46
3.1	Introduction	46
3.2	Robot design	48
3.2.1	Mechanical design	48
3.2.2	Kinematics	51
3.2.3	Image Jacobian	52
3.2.4	Workspace analysis	53
3.2.5	Actuators	54
3.3	Control	54
3.3.1	Fiducials	56
3.3.2	Hysteresis and actuation variability	58
3.3.3	MRI based visual servoing control	63
3.3.4	4 Axis repeatability	64
3.3.5	Camera based positioning	65
3.3.6	MRI positioning feedback experiments	67
3.3.7	Accuracy discussion	68
3.4	Target selection interface and system design	69
3.4.1	Clinical preferences	70

3.4.2	Surgical freedom simulation	70
3.4.3	VR environment for target selection	72
3.5	MRI imaging considerations	79
3.5.1	MRI image quality	79
3.5.2	Image and positioning time	79
3.6	Super resolution positioning	80
3.6.1	Super resolution offset matrix generation	81
3.6.2	Super resolution image construction	82
3.7	Applications beyond cellular therapeutics	87
3.7.1	Radiofrequency ablation	87
3.7.2	MRE	88
3.8	Aim 2 summary	89
3.9	Future work	89
3.9.1	Animal model validation	89
3.9.2	Patient mounting	90
 Chapter 4: Aim 3: Measurement of in-vivo tissue properties via the development of a new Magnetic Resonance Elastography actuator		 92
4.1	Magnetic resonance elastography background	92
4.2	MRE actuators	93
4.2.1	MRE actuator specifications	93
4.2.2	MRE actuator design	94
4.2.3	Finite element analysis	97
4.2.4	Fabrication	101

4.2.5	Frequency tuning experimental validation	101
4.2.6	MRI evaluation of piezoelectric drivers	102
4.3	5 DOF positioning of MRE actuators	106
4.3.1	Planned procedure workflow	106
4.3.2	Mechanical design	107
4.3.3	Control	108
4.3.4	4 + 1 control scheme	112
4.3.5	Benchtop positioning experiments	113
4.3.6	Two phase positioning control	115
4.3.7	MRI evaluation	117
4.4	Aim 3 summary	118
4.5	Future work	119
Chapter 5: Conclusion		120
5.1	Future work	121
Appendices		122
Appendix A:	SSEP prediction from stimulation intensity	123
Appendix B:	Robot mounting and control images	131
Appendix C:	Adjustable resonant frame	134
References		135
Vita		144

LIST OF TABLES

2.1	Classification accuracy for each subject	18
2.2	Velocity and kinetic energy of automated hammer	23
2.3	Force evaluation results	23
2.4	Timing evaluation results	29
2.5	Novice survey results by reflex grade	32
2.6	SSEP stimulus intensity	41
2.7	SSEP peak-peak amplitudes	43
3.1	Workflow of benchtop and MRI experiments	83
3.2	Results of benchtop and MRI experiments	87

LIST OF FIGURES

2.1	Peripheral stimulus diagram, the afferent response to both electrical stimulation of the nerve and mechanical tapping of the tendon are shown	6
2.2	Mean amplitude spectrum of robotic tapping on two human subjects, shaded portions represent one standard deviation	7
2.3	χ^2 associated p values for each frequency, computed via MATLAB command Chi2gof, the two values for α shown are the Bonferroni corrected value ($0.05/n$) as well as the standard $\alpha = 0.05$	8
2.4	Spring-damper model k is the combined effective stiffness of the hammer and impacted tissue, while C is the effective damping constant	9
2.5	Hertz contact model, The sphere represents the hammer head, while the plane represents the impacted tissue; m is the hammer mass, R its radius, E and ν represent the hammer and tissue's elastic modulus and Poisson's ratios respectively.	11
2.6	Nonlinear spring adaptation of the Hertz contact model	12
2.7	Instrumented hammer and tapping robot, frames show position of the hammer during the tapping motion	13
2.8	Mean and STD values for effective stiffness after 150 trials on DS10 and DS30 silicone as computed by fitting the spring-damper model	14
2.9	Mean and STD values for damping constant after 150 trials on DS10 and DS30 silicone, from the spring-damper model	14
2.10	silicone effective modulus estimated from the Hertz contact model	14
2.11	Human effective modulus estimated from the Hertz contact model	15
2.12	Human effective stiffness estimated from the spring-damper model	15

2.13	Comparison of estimated modulus and impact velocity	16
2.14	Representative feature vector used as training data for the SVM classifier . .	17
2.15	Mock tendon experimental setup	19
2.16	Human operator experimental setup	20
2.17	Force result histogram, maximum force normalized to the mean of the hard automated taps	24
2.18	Expert and novice tendon tapping acceleration variability	25
2.19	Timing result histogram	27
2.20	Single operator tap intervals	28
2.21	Example survey question with obscured hammer impact and 0-4 grading choices.	31
2.22	Survey results A) Mean score for each true score, B) Mean number of errors for each true score, * represents $p < 0.05$	32
2.23	Proposed remote deep tendon reflex exam system A) Remote portion with smart hammer assisted reflex elicitation and grading, B) Clinical portion, with clinician receiving assessed scores and communicating with patient, C) Tapping application screen.	34
2.24	Picture of the smart tendon hammer used throughout this work.	35
2.25	Tapping feedback and data collection application, A) Result after success- ful tap, B) Result after an incorrect tap, the red and green lines represent the acceleration of the most recent incorrect and correct taps respectively. .	36
2.26	SSEP measurement conditions	40
2.27	Single subject SSEP results	42
3.1	MRI visual feedback schematic, a) 3T MRI and robot, b) closeup of robot, c) silicone and ABS spinal phantom produced from CT data [51], d) patient orientation, e) control room diagram	49
3.2	Parallel plane robot, a) robot and b) positioning mechanism	50

3.3	Forward kinematics diagram	52
3.4	Positioning range for varied actuator travel and plane distances.	53
3.5	Top plane positioning variables, a) shows the robot positioning parameters, b) shows the image plane in red and positioning variables measured via image	54
3.6	Workspace of the robot	55
3.7	Robot stage design, x axis motion shown in blue, yaxis motion shown in yellow	56
3.8	a) Full robot CAD model with upper and lower stages shown b) Robot with salient dimensions	57
3.9	Fiducial markers used in this work, A) offset spherical fiducial, B) inline spherical fiducial, C) collar fiducial	57
3.10	Single stage open-loop positioning performance evaluation setup	58
3.11	Repeatability of X actuator motions	59
3.12	Repeatability of Y actuator motions	60
3.13	Hysteresis of X actuator motions	61
3.14	Hysteresis of Y actuator motions	61
3.15	Representative hysteresis loops for 4 measurement positions	63
3.16	Laser position sensor experimental setup	65
3.17	Repeatability results, red dots and green lines represent the 5 evaluated robot configurations, the plotted spheres have radii equivalent to the mean standard deviation for each of the configurations	66
3.18	Positioning results for a) Camera based servoing and b) MRI guided servoing	67
3.19	Positioning results with laser position feedback	68
3.20	2D planned needle trajectory with target, and current and target needle tra- jectories shown	70
3.21	Surgical freedom simulation results with all potential trajectories shown . . .	72

3.22	Surgical freedom simulation results with robot and vertebrae model, an example needle path is shown in green	72
3.23	The VR guided system reported in this work, A) The image guidance system and B), the robot actuation scheme	73
3.24	VR Image processing and procedural steps, A) DICOM data sampled for bone material, B) Material choice and reference frame selection interface, C) Full DICOM image of a gelatin phantom, D) Selected trajectory to the target D) Detected robot configuration, plane heights and target configuration, E) Program output to controller, current and targeted robot fiducial locations each in Cartesian form	75
3.25	MRI phantom and contrasting fiducials mounted to the needle guide below each joint	77
3.26	Axial MRI view of the phantom	78
3.27	VR planned needle trajectory with target, and current and target needle trajectories shown	78
3.28	Images of the cylindrical phantom with and without the robot, regions used in the calculation of SNR are shown, with the signal intensity taken from the green circles and noise taken from red circles.	80
3.29	MRI view of stage fiducials and silicone spinal cord phantom, The vantage point shown is the one used for image-based visual servoing control.	81
3.30	MRI SR reconstruction, a) first image with no spatial shift, b-d) three spatially shifted images with arrow representing magnitude and direction of spatial shift relative to first image. box represents 1 pixel e) SR reconstruction.	82
3.31	Benchtop experimental set up, b) Base resolution image acquired from experiment c) Target mounted below robot d) Super resolution image reconstructed from benchtop experiments.	85
3.32	Experimental results, base resolution targeting in blue, interpolated targeting in green and super resolution targeting in red, circles represent the standard deviation of each group, a) Benchtop results, b) MRI results.	86
3.33	MRI experimental set up, b) Fiducial marker attached to top plane of robot, c) Super resolution image reconstructed from MRI experiments with a circle plotted based on image finding algorithm.	87

3.34	Animal model mounting and positioning pilot testing	90
3.35	Robot mounting via K wire	91
4.1	Magnetic resonance elastography imaging methodology	93
4.2	Tunable resonant actuator frame	96
4.3	Effect of wall thickness in tuning range; red box shows the chosen value of 0.5 mm	97
4.4	Resonance tuning mechanism; A) APA 150M frame, B) Piezoceramic stack, C) Linear piezoelectric actuator, D) 655 bronze frame	98
4.5	1) Bronze resonant frames and 2) APA 150M actuator and resonant frame	99
4.6	Mode Shapes and associated frequencies, 1 mm mass location	99
4.7	Mode Shapes and associated frequencies, 5 mm mass location	100
4.8	Mode Shapes and associated frequencies, 10 mm mass location	100
4.9	3rd resonant mode displacement for each frame	101
4.10	Experimental setup for MRE actuator resonant frequency measurements	102
4.11	Amplitude spectrum for 1mm and 10mm frames	103
4.12	Estimated and measured resonant frequency for each mass location	103
4.13	Silicone phantom and casting process	104
4.14	MRI evaluation setup	105
4.15	MRI evaluation images A) Magnitude image, B) Computed displacement image, C) Stiffness map, mean shear stiffness in the center ROI is 0.78 kPa	106
4.16	Workflow for robotic positioning of MRE drivers	107
4.17	5 DOF MRE actuator positioning robot, A) Completed prototype, and B) CAD model	108
4.18	MRI scan of the positioning robot, with planar collar fiducials and endpoint fiducial.	109

4.19	Kinematics diagram of the MRE positioning robot	109
4.20	Two stage driver positioning process	112
4.21	Benchtop experimental setup	114
4.22	Benchtop experimental results, both position and orientation error over 10 updates for two different target locations	115
4.23	Benchtop RGB-D fiducial mounted to robot, endpoint position and orientation were found via the center positions of the two spheres	116
4.24	Benchtop experimental results, orientation and position over the planar and 5th degree of freedom positioning protocol, mean and standard deviation	117
4.25	Experimental Setup.	118
4.26	Displacement fields and associated robot configurations	119
A.1	Representative predictions and EEG data for 4 individual taps	125
A.2	Standard prediction method and LSTM network predictions of individual SSEPs	126
A.3	Mean RMSE results for the prediction of individual EEG responses to tapping from acceleration, mean is the standard SSEP signal combining all stimulus averaged trials, prediction is the individual LSTM network prediction from hammer acceleration	127
A.4	LSTM predicted EEG and recorded EEG for individual trials at 2 tapping stimulation intensities	128
A.5	Standard prediction method and LSTM network predictions of individual SSEPs	129
B.1	Control room showing scanner, animal model and 2D image views	131
B.2	Robot Mounting	132
B.3	Camera setup	132
B.4	Radiograph	133

C.1 Resonant frame 134

SUMMARY

The central goal of this work is the development and application of precise robotic interventions to the human nervous system. This work makes contributions in the areas of diagnosis, imaging, and treatment, of the brain, peripheral nervous system and spine, through the development of new robotic devices, smart systems, analysis methods and actuators.

Human variability is one of the most challenging aspects of technological innovation for healthcare. Because of the manual nature of healthcare delivery today, clinician variability is at least as important as patient variability. To further neurological diagnosis and interventions, robotic systems must mitigate or complement human variability. This work reports the development of robotic systems and methods towards that goal in a variety of neurological applications.

In the deep tendon reflex, variability in stimulation intensity must be characterized, and automation can reduce variability in timing for rehabilitative applications. Magnetic resonance imaging guidance provides a feasible method for performing procedures dealing with sensitive and complex anatomy in a repeatable manner. In magnetic resonance elastography (MRE) actuator design, positioning and tuning of drivers to individual tissues and patients provides the necessary flexibility to extend the use of MRE.

While the tendon reflex has been known for nearly 150 years, the diagnostic and particularly, therapeutic utility of the reflex is still being explored. This work starts with the development of analysis methods for tendon tapping location detection, along with an instrumented hammer and assistive application for extending the diagnostic utility of the reflex to remote examination. Through an evaluation of human tapping performance and the development of a robotic tapping device, the potential of reflex elicitation to aid in rehabilitation is also reported. In a more direct intervention, an MRI guided robot for direct injection of cellular therapeutics is developed and evaluated. The unique structure of

the robot provides the opportunity not only for high repeatability and accuracy, but also the implementation of super resolution imaging and positioning. The mechanical properties of the spine are also assessed in MRI. As MRE moves beyond larger tissues and into stiffer regions with smaller geometries, higher driving frequencies are necessary. To achieve this, a tunable resonance piezoelectric MRE actuator is developed and evaluated. The MRI guided robot is then combined with an MRE actuator to produce a system for the automated positioning of MRE drivers within the MRI scanner.

- Chapter 1 will describe the motivations and background for this work.
- Chapter 2 will detail the development of tendon tapping analysis methods and devices for both diagnostic and therapeutic uses.
- Chapter 3 will discuss the development and evaluation of an MRI guided 4 DOF needle guide positioning robot for intraspinal injections.
- Chapter 4 will report the development of a tunable resonance MRE actuator and design of a 5 DOF robot for active positioning of MRE drivers.
- Chapter 5 will conclude the document and propose future work to enhance and extend the reported results.

CHAPTER 1

INTRODUCTION

1.1 Aims

This work seeks to develop methods for precise robotic diagnosis and intervention in the human nervous system. The objectives and contributions of the work are delineated in 3 aims :

1.1.1 Aim 1 - Enhanced neurological diagnosis and treatment via improved peripheral stimulation methods

The first aim of this work is measurement and reinforcement of brain and spinal cord integrity via tendon tapping. This is achieved by the development of analysis methods for conventional (manual) tendon tapping, as well as the production of a robotic precision stimulation device for physiological investigation of the rehabilitative potential of deep tendon reflex stimulation and a system for remote reflex examination. The primary contributions to the present knowledge in the field are the analysis methods, remote tapping system and physiological data collection methods and results.

1.1.2 Aim 2 -Development of a new robot morphology for high resolution intervention in the spinal cord

The second aim of this work is development of a 4 degree of freedom positioning robot for use in MRI guided injections. This work was evaluated in both benchtop accuracy experiments and phantom and animal model testing. This project resulted in contributions to the field of MRI guided robot design and control.

1.1.3 Aim 3 - Development of a novel magnetic resonance elastography actuator and positioning system

The final aim of this work is the development of both a tunable high frequency MRE actuator and active positioning system for measurement of in-vivo tissue properties in MRI. This tunable resonance MRE actuator is validated in simulation, benchtop and MRE imaging. The primary contribution is in the area of MRE actuator and system design.

1.2 Motivation

Mechanical testing of the human body is one of the oldest diagnostic methodologies, with the invention of thoracic percussive tests by Leopold Auenbrugger in 1761 often considered the genesis of modern physical diagnosis [1]. Auenbrugger developed a method of tapping the chest of patients and observing the audible response in order to diagnose cardiovascular and other diseases. Although scientific and clinical practices have advanced significantly in the last 260 years, the core premise, the use of mechanical interaction and observation to investigate, diagnose and treat an illness forms the basis for the work presented here.

The primary motivation of this work is the application of mechanical modeling, design and automation to the diagnosis and mitigation of disease. A critical component is the use of modeling and mechanical interaction to assess tissue properties in order to both interrogate disease progression, as well as guide intervention. With the development of new imaging techniques and therapeutic approaches, accompanying advances in robotics are necessary to enable the full realization of novel therapeutic potential.

The rehabilitation techniques of paired associative stimulation (PAS) and repetitive facilitation exercise (RFE) have effectively created a new intervention paradigm utilizing paired stimulations to facilitate plasticity and restore synaptic excitability. The use of manual tendon tapping to diagnose neurological disorders has been a standard part of neurological examination since the reporting of the deep tendon reflex by Erb and Westphal in 1875

[2, 1]. However, manual tapping with a handheld hammer has also remained the standard methodology since the invention of the reflex hammer by John Taylor a few years later in 1888 [2, 1]. While the traditional PAS paradigm has proven effective with peripheral stimulation provided by electrical stimulation, investigation of mechanical peripheral stimulation for PAS has been hampered by the lack of an automated method for precision delivery of stimulus to the muscle fibers. The development of an automated tendon tapping device embodied with the ability to analyze tapping locations is critical to the further exploration and effectiveness of mPAS and other paired stimulation techniques, both for physiological investigation and rehabilitation.

In a parallel (but higher frequency) application, the advent of new MRI imaging techniques necessitates the development of precise actuators for tissue interrogation. The development of magnetic resonance elastography (MRE) enabled clinicians to diagnose and track the progression of liver fibrosis via MRI mitigating the need for invasive biopsy procedures [3]. Although the ability to non-invasively image tissue properties produced a paradigm shift in liver disease treatment, adaptation of the technique to other diseases was stymied by the lack of available actuation modalities [4]. Significant advancements in the design of MRE actuators are necessary to both improve efficacy and enable use in stiffer target tissues, such as the intervertebral discs. Additionally, current MRE drivers are statically positioned, and the development of a system for active driver positioning is of particular benefit to higher frequency applications.

Another focus of this work again involves neurological disorders and MR imaging, but is primarily concerned with direct intervention. Cellular therapeutics are a promising avenue for the treatment of conditions such as amyotrophic lateral sclerosis (ALS) [5, 6]. However the target for these therapeutics is the ventral horn of the spinal cord, a relatively inaccessible location, particularly in medically fragile ALS patients. While MRI guided injections have the potential to mitigate the invasive nature of traditional surgery to expose the spinal cord, manual needle positioning under MRI guidance is time consuming and

difficult [6]. The aim of this work is to develop an MRI guided needle positioning robot for use in intraspinal injection procedures.

CHAPTER 2

AIM 1: ENHANCED NEUROLOGICAL DIAGNOSIS AND TREATMENT VIA IMPROVED PERIPHERAL STIMULATION METHODS

2.1 Introduction

The tendon stretch reflex (DTR) is the sensory and motor response caused by a rapid stretching of the tendon, usually stimulated via reflex hammer. A diagram of the tendon reflex and associated neural pathways is shown in Figure 2.1. Stimulation of the tendon reflex is a common clinical practice in the standard neurological exam, assessment of trauma, and rehabilitation [7, 8, 9]. Although some quantitative or partially quantitative methods exist in both the diagnostic and therapeutic arenas, the bulk of tendon stretch response stimulation is done in a subjective manner. This subjectivity both reduces the diagnostic utility of the test and is a significant impediment to the therapeutic use of reflex elicitation. In particular, a lack of the ability to control stimulus intensity as measured by sensory response precludes the use of this as either an investigatory or therapeutic parameter. This work seeks to improve the characterization and repeatability of stimulus delivery in tendon tapping to enable broader diagnostic and therapeutic uses.

2.2 Location detection

Impact location is a critical factor in stimulation of the DTR. As such, automated detection of impact location is essential to the development of any analysis methods for tapping assistance. In this work, impact location is defined by the impacted tissue, with the target location the tendon apex, as is standard in DTR elicitation. The following section includes a feasibility analysis for automated location detection from acceleration measurements, mechanical model based detection methods and learned models.

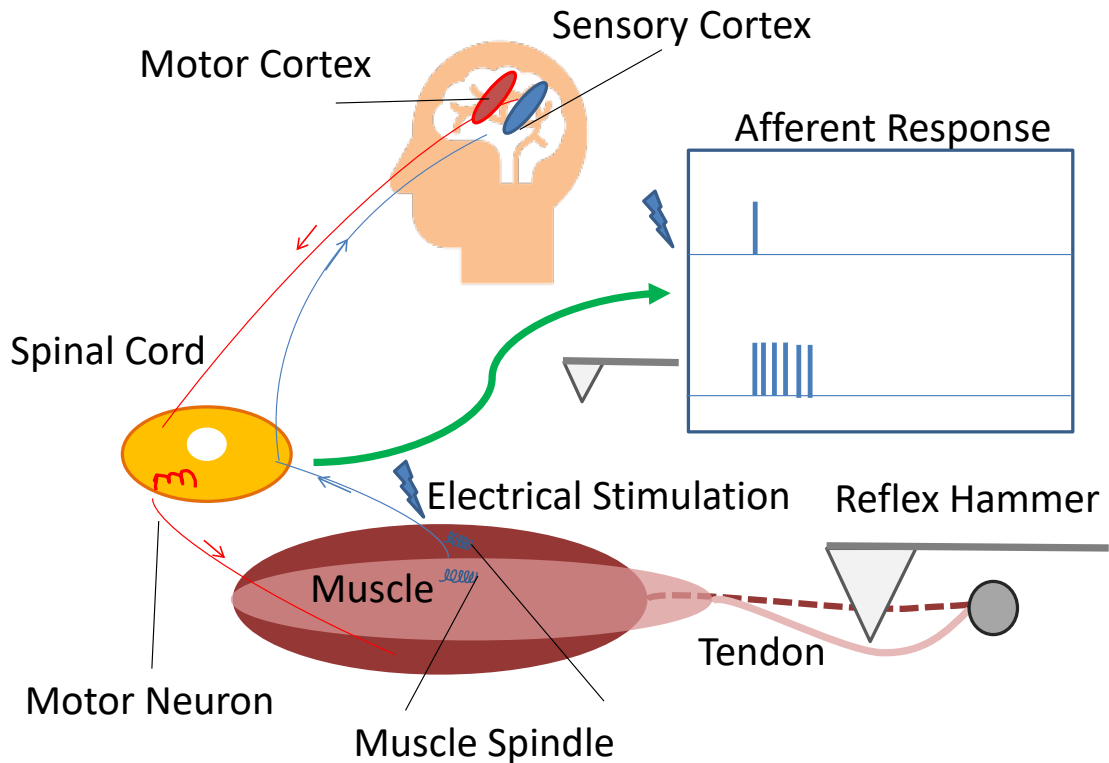


Figure 2.1: Peripheral stimulus diagram, the afferent response to both electrical stimulation of the nerve and mechanical tapping of the tendon are shown

2.2.1 Frequency content of hammer acceleration

The primary aim of the technical developments reported here is the accurate classification of tendon tapping from hammer acceleration measurements. It is essential that the information to discriminate between correct and incorrect stimulation is contained within the readily measurable hammer acceleration. In the case of the wireless instrumented hammer and mobile application described later in subsection 2.4.2, Bluetooth communication is the primary limiting factor for the sample rate. To evaluate the practicality of classification via streamed acceleration measurements (limited to 200Hz), a human tapping data set was collected at 800Hz using a previously developed automated tapping device [10]. 50 taps were analyzed from two locations on each of the two subjects, the apex of the right Achilles tendon, and an adjacent location. Acceleration during impact and the following

0.2 seconds were recorded. All data collection occurred under an institutionally approved protocol (GT# H17264).

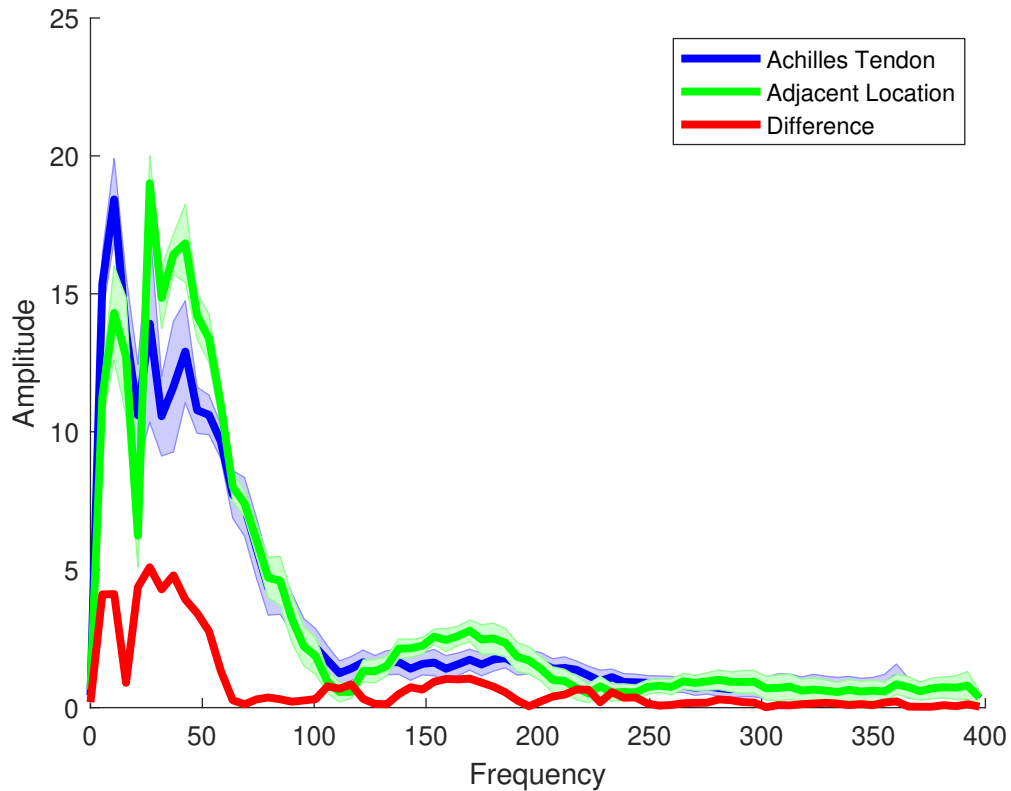


Figure 2.2: Mean amplitude spectrum of robotic tapping on two human subjects, shaded portions represent one standard deviation

The frequency content of each tap was ascertained by discrete Fourier transform (*fft*, MATLAB, MathWorks Inc, USA). Mean results for both subjects, along with the difference between the two means, are shown in Figure 2.2. Clear separation between the tendon and incorrect location is apparent up to about 60 Hz, which indicates that the 200Hz sampling rate is more than sufficient for tapping classification. A t-test confirmed ($p < 0.001$) that the mean power of the first 50Hz of the spectrum was significantly different between the on tendon and off tendon conditions. There was a significant difference ($p < 0.01$) in the mean powers from 50 Hz to 400 Hz, but not from 100 Hz to 400 Hz ($p > 0.05$). For the statistical tests, power in the respective bandwidths was computed for each tap, then the

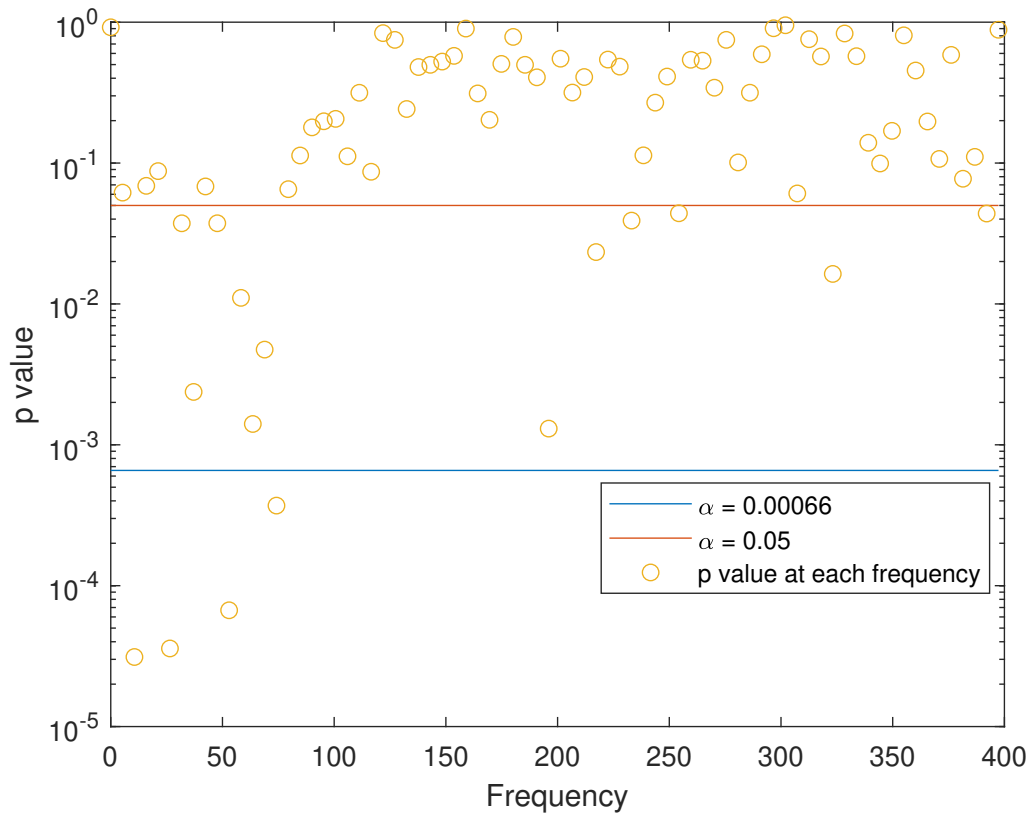


Figure 2.3: χ^2 associated p values for each frequency, computed via MATLAB command Chi2gof, the two values for α shown are the Bonferroni corrected value ($0.05/n$) as well as the standard $\alpha = 0.05$

groups of 100 were tested against the null hypothesis that there was not a difference in the population means. The results of a χ^2 test for the full frequency range are shown in Figure 2.3. Although the reported results pertain only to the Achilles tendon, it is expected that other tendons produce similar acceleration profiles and frequency spectra.

Both the waveform and amplitude of the frequency response contain important information for differentiating the two locations. The waveform most likely contains differences in frequency dependent damping, while differences in amplitude are most likely due to the level of impedance matching between the hammer and tissues. These properties are each individually viable choices for location classification, while acceleration time series contains both frequency and amplitude information, such that any classifier utilizing acceleration

time series inherently leverages both domains.

2.2.2 Mechanical models for location detection

The preceding section demonstrated that it should be feasible to differentiate impact locations from hammer acceleration. Two different mechanical models were evaluated for their ability to discriminate between different tissue types. The two models were a mass-spring-damper model and a Hertz contact model (nonlinear spring).

2.2.3 Spring-damper model

Because of the viscoelasticity inherent in many human tissues, a parallel spring dashpot model was evaluated for use in the tendon impact problem. This basic model of the impact as the interaction of a mass with initial velocity and a spring and damper in parallel is shown in Figure 2.4. The equations of motion are governed by m , C and K . Where m is the mass of the hammer, C is the effective damping constant and K is the effective spring constant.

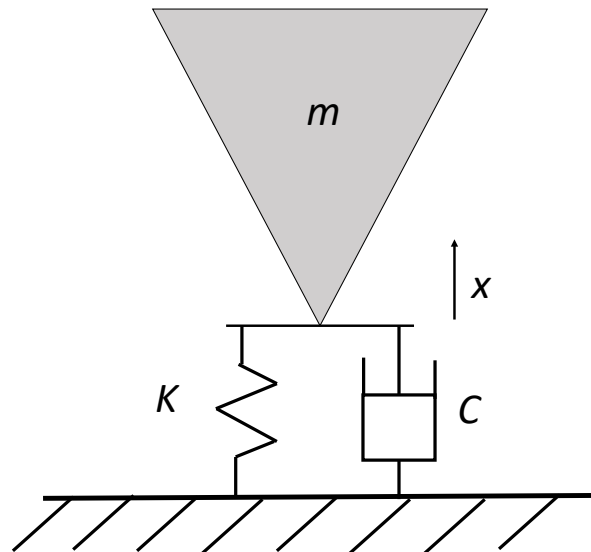


Figure 2.4: Spring-damper model k is the combined effective stiffness of the hammer and impacted tissue, while C is the effective damping constant

The equation of motion for the system in Figure 2.4 can then be found,

$$m\ddot{x} = -Kx - C\dot{x} + F \quad (2.1)$$

with initial conditions $\dot{x}_0 = V_0, x_0 = 0$ and constant applied force F . It should be noted that $x < 0$ during contact with the tissue .

It is important to note that the above model has the significant benefit of an analytical solution for $x(t)$. The contact area between the hammer and substrate is assumed constant, and both materials are modeled as linearly elastic springs. Both of these are clear simplifications of the more complicated system. In addition to these assumptions, this model does not enable the computation of material properties from the acceleration data without knowledge of some of the dimensions of the two bodies.

2.2.4 Hertz contact model

Although the above spring-damper model captures the important dissipative characteristics of the impacted tissue, it does not characterize the changing contact area with penetration depth. In addition, because the effective stiffness and damping are measured, assumptions about the geometry must be made to extract material properties. Instead, a contact model was proposed to capture these changes in contact area and thus more easily estimate material properties of the impacted tissue.

Contact between an elastic sphere and an elastic half space is a canonical problem in contact mechanics, and analytic solutions for contact force exist [11]. The sphere-half space model is shown in Figure 2.5

The force between an elastic sphere and elastic half space can be calculated analytically [11] as

$$P = \frac{4}{3}E^*R^{\frac{1}{2}}\delta^{\frac{3}{2}} \quad (2.2)$$

where P is the contact force, E^* is calculated from the Poisson's ratios and Young's moduli

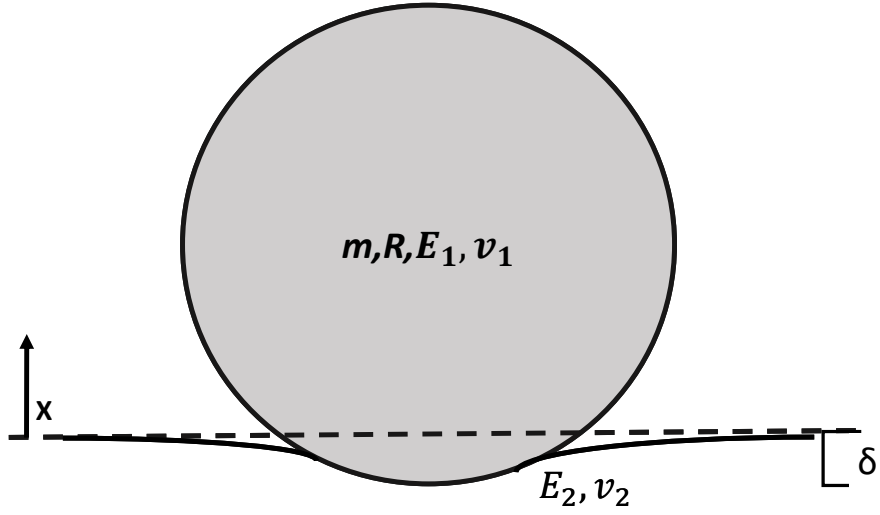


Figure 2.5: Hertz contact model, The sphere represents the hammer head, while the plane represents the impacted tissue; m is the hammer mass, R its radius, E and ν represent the hammer and tissue's elastic modulus and Poisson's ratios respectively.

of the two bodies, R is the sphere radius and δ is the indentation depth. With hammer acceleration and dynamic information, δ can be calculated, R is known, and P can be computed with the mass and acceleration orthogonal to the contact plane. The unknown parameter in Equation 2.7 is then E^* . Rearranging gives E^* for a given δ and contact force, P

$$E^* = \frac{3}{4} P R^{-\frac{1}{2}} \delta^{-\frac{3}{2}}. \quad (2.3)$$

As stated earlier, E^* is constructed from the material properties of the sphere and half space [11]. With the subscripts referring to the sphere and half space respectively

$$\frac{1}{E^*} = \frac{1 - \nu_1^2}{E_1} + \frac{1 - \nu_2^2}{E_2}. \quad (2.4)$$

Finding E_2 may allow estimation of stimulus location relative to the tendon apex.

The equation of motion governing the hammer during impact is then

$$m\ddot{x} = -\frac{4}{3}E^*R^{\frac{1}{2}}x^{\frac{3}{2}}. \quad (2.5)$$

Fitting the solution of Equation 2.5 to experimental data allows determination of E^* , and with a known E_1 , v_1 , v_2 , and R , the unknown sample's modulus, E_2 can be computed.

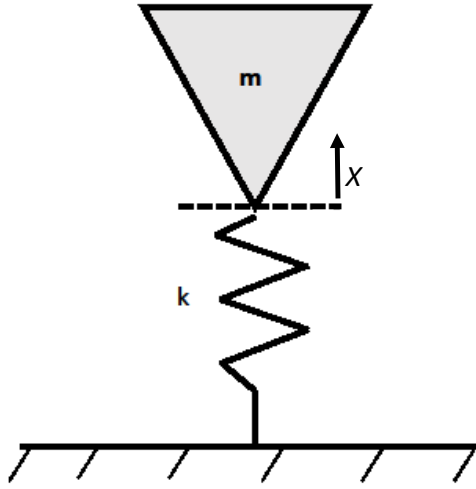


Figure 2.6: Nonlinear spring adaptation of the Hertz contact model

Equation 2.5 can equivalently describe a nonlinear spring where the stiffness $K = \frac{4}{3}E^*R^{\frac{1}{2}}$, and spring force is described by $Kx^{\frac{3}{2}}$, this is shown in Figure 2.6. Unfortunately, a closed form solution of Equation 2.5 does not exist, however the above method can be used numerically to estimate E_2 from the hammer acceleration during impact.

2.2.5 Tapping device

The tapping apparatus used in this work is shown in Figure 2.7. The instrumented hammer is driven by a geared DC motor via a flexible shaft coupling and drive shaft rigidly fixed to the hammer handle. An analog signal is sent to a motor controller in current control mode. (16A20AC, Advanced Motion Controls, Camarillo, USA). The hammer is driven downward for 300ms and then returned to its original raised position. A mechanical stop

is used in the raised position to ensure consistency between trials, negating the need for position feedback. The times shown in Figure 2.7 represent the time from the beginning of the tapping motions, the time used for all computations actually begins at the moment of impact, or $t = .30$ in the figure.

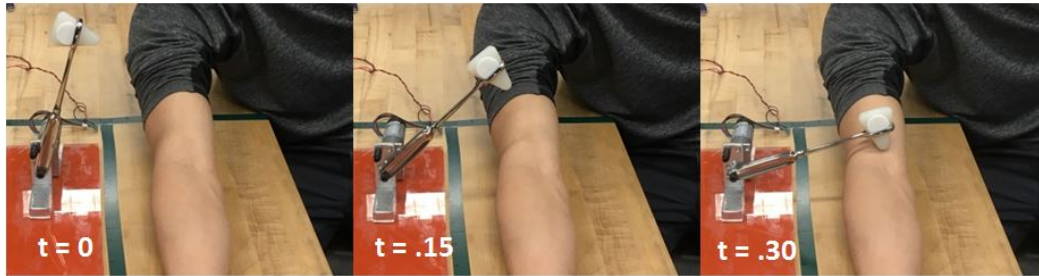


Figure 2.7: Instrumented hammer and tapping robot, frames show position of the hammer during the tapping motion

2.2.6 Model results

Both of the above models were fit to experimental acceleration data. Results from the two silicone rubber sample are shown in Figure 2.8, Figure 2.9, and Figure 2.10. Both figures represent the results from 100 taps on each of the two samples with the tapping device. The same models were fit to the experimental Achilles tendon tapping data from the two human subjects, with results shown in Figure 2.11 and Figure 2.12. It should be noted that in all cases the classification performance is the metric of interest, not the true values of stiffness, damping constant or modulus.

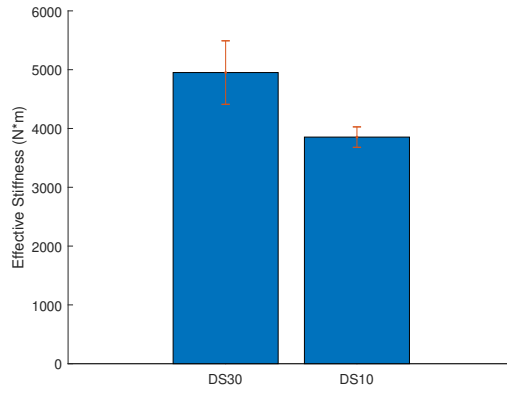


Figure 2.8: Mean and STD values for effective stiffness after 150 trials on DS10 and DS30 silicone as computed by fitting the spring-damper model

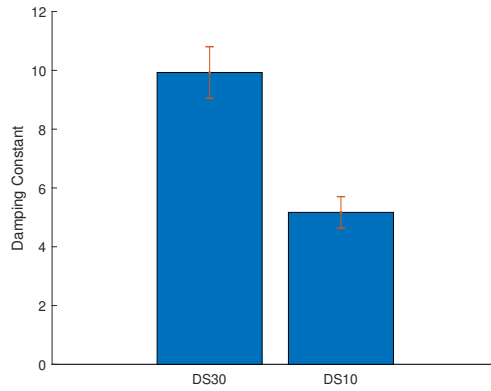


Figure 2.9: Mean and STD values for damping constant after 150 trials on DS10 and DS30 silicone, from the spring-damper model

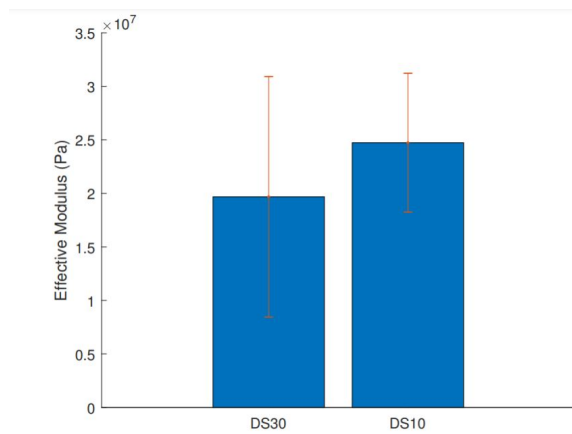


Figure 2.10: silicone effective modulus estimated from the Hertz contact model

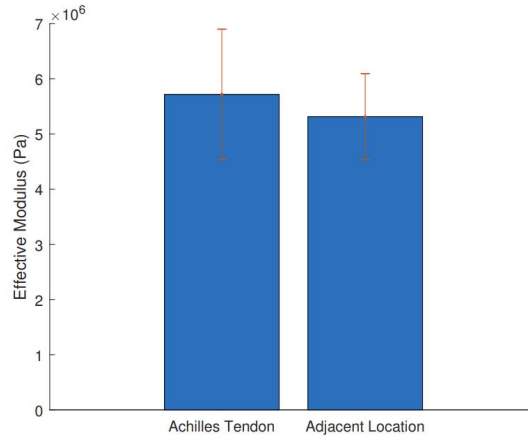


Figure 2.11: Human effective modulus estimated from the Hertz contact model

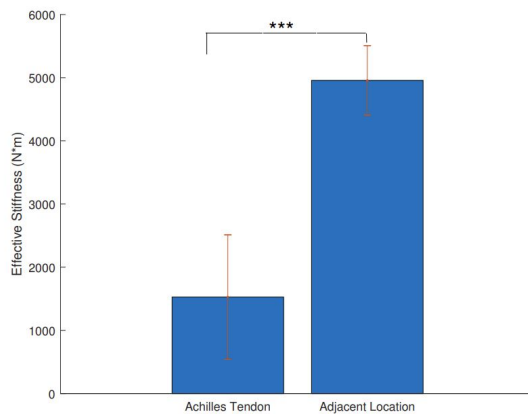


Figure 2.12: Human effective stiffness estimated from the spring-damper model

Figure 2.13 shows the potential relationship between the fitted modulus and initial velocity values. It is likely that that this silicone rubber displays strain rate dependent changes in elastic modulus, however this dependence is difficult to disentangle from other simplifications in the model.

Figure 2.8, demonstrates the utility of both fitted parameters in differentiating the two silicone samples. Although actual values for the effective stiffness are not available, an empirical calculation based on the reported Shore A hardness of the silicones and the measured geometry of the hammer and samples was done as a point of reference. The spring constant of the DS30 silicone was estimated at 8685N/m while the DS10 silicone was estimated to have a 3137N/m spring constant. While the fitted values are not identical to the

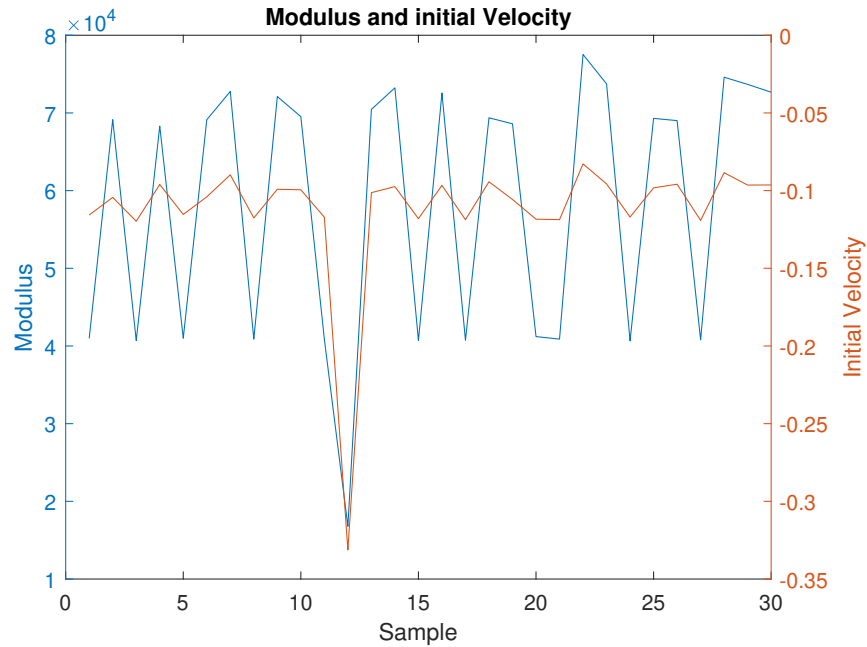


Figure 2.13: Comparison of estimated modulus and impact velocity

estimated ones, they are fairly close, and discrepancies could be due to geometry estimation errors. Damping constant information was not available, so the accuracy of the estimation of C is difficult to assess. Although the absolute accuracy of the spring damper modeling approach may be imperfect, it is clear from Figure 2.8 and Figure 2.9 that these parameters are effective for material classification.

The results shown from fitting the spring-damper model to the acceleration data effectively demonstrate that this method is capable of distinguishing between effective and ineffective stimulus based on the underlying material properties of the impacted tissue. The Hertz model fares relatively poorly in comparison, particularly on the human subject data. A discussion of model assumptions, fits and additional prospective models is provided below in subsection 2.7.1.

2.2.7 Learned models for location detection

While the analytical models demonstrated some utility for tapping location detection, the fit difficulties and relative ease of data collection motivated the use of a data driven approach

as well. Learned models were explored in the form of support vector machines (SVM).

2.2.8 SVM classifier

To evaluate the classification of tendon tapping location from streamed acceleration data, an additional set of human trials were carried out. Each subject underwent 100 taps from an instrumented tendon hammer, 50 taps to the right Achilles tendon, and 50 taps to a laterally adjacent location. A total of 8 healthy adult subjects participated in the experiments (mean age 36.5, 5 F), following an approved human subjects research protocol (GT# H20531).

An example of the feature vector used for the SVM based classifier is shown in Figure 2.14. The feature vector consists of 51 acceleration points, 2 prior to peak deceleration, and 49 after the peak deceleration.

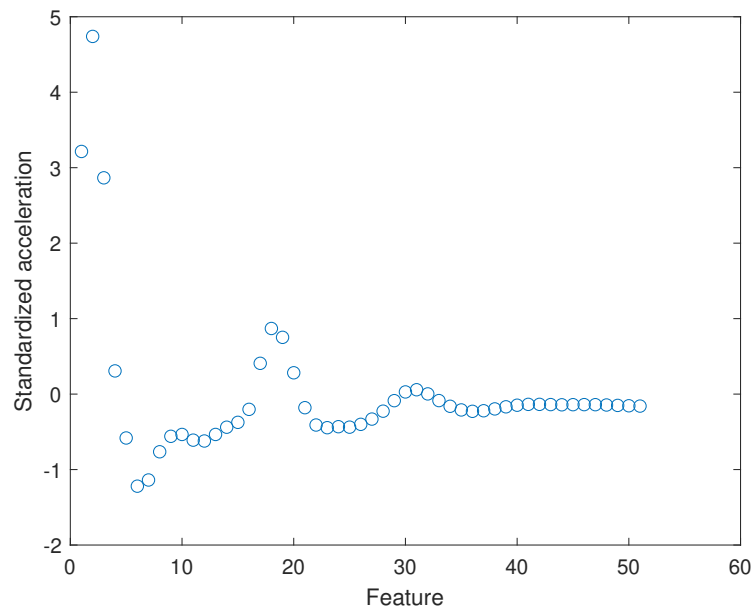


Figure 2.14: Representative feature vector used as training data for the SVM classifier

The large number of sample points and classification problem associated with traditional stimulus delivery during tendon tapping lends itself to SVM based classification. Although a large number of additional classification methods exist, SVM was chosen due to the portability of the model and the training speed. In order to evaluate the suitability

Table 2.1: Classification accuracy for each subject

Subject	1	2	3	4	5	6	7	8	Mean
Classification Accuracy (%)	100	98	86	90	98	100	67	93	91.5

of SVM classification of the tapping location, 8 different test/train datasets were produced, with a single subject comprising the test set and the remaining 7 making up the training set. The feature vector used consisted of the acceleration at each sample taken by the IMU. Each acceleration time series (feature vector) was standardized prior to training of the model. The models were trained in MATLAB, (fitsvm), with a linear kernel. Accuracy of the models was assessed as the accuracy in correctly classifying the 100 taps on the held out subject.

The linear SVM classification method produces a simple model of coefficient weights and an offset, which allows for easy transfer to a mobile application. Classification also can take place in near realtime, because of the computational simplicity. The accuracy of the trained SVM models for the achilles tendon is shown in Table 2.1.

Mean classification accuracy was 91.5% with a range of 67% when subject 7 was held out for testing to 100% on subjects 1 and 6. With the relatively small subject pool, the high accuracy demonstrates the suitability of the SVM based classification method for determining tapping impact location from streamed (200Hz) acceleration data.

2.3 Human performance in DTR elicitation

Both diagnostic and therapeutic stimulation of the DTR has traditionally been performed manually by clinicians [12, 13]. For this reason, an evaluation of the human performance on the factors relating to successful reflex elicitation, stimulation intensity and timing reliability is necessary. This was performed via benchtop experiments with both expert and novice participants. To compare stimulus intensity and timing performance between manual and automated tendon tapping, three different benchtop experiments were done, the first two sets compared tap timing and resultant tension force between human and robotic

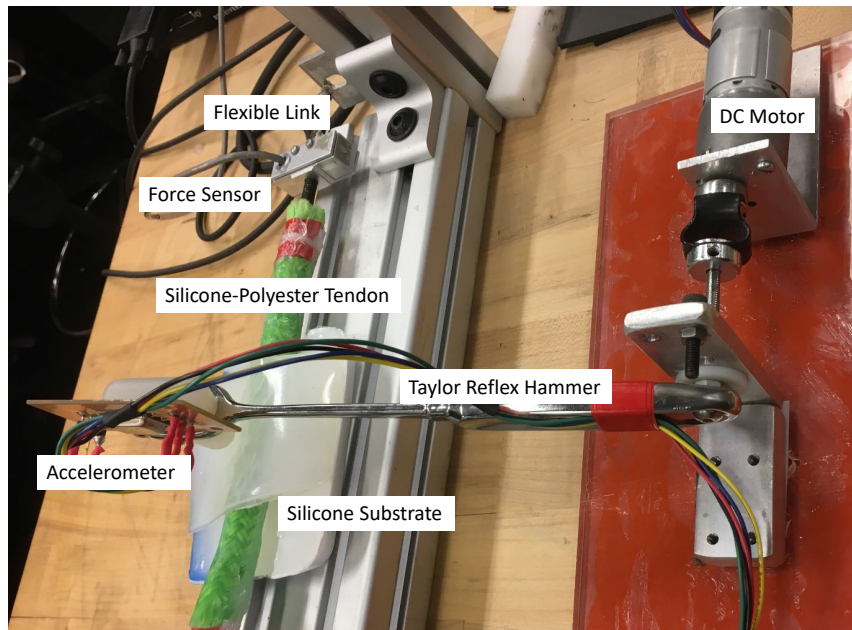


Figure 2.15: Mock tendon experimental setup

tapping. The last set compared tapping intensity between expert and novice users of an instrumented hammer.

2.3.1 Automated tapping experiments

An automated tendon tapping device and mock tendon were used to conduct benchtop experiments. The tendon tapping robot and experimental setup are shown in Figure 2.15. The robot was used to perform 1000 taps at three different constant torques on the apex of the silicone tendon. The hammer acceleration and tension in the mock tendon were measured at 800Hz. Taps were performed at a fixed 1Hz frequency. It is important to note the flexible coupling in Figure 2.15, as this allows the tension force to be measured throughout the tendon deflection. With a rigid mounting of the force sensor, much of the impact force is seen as torque instead of tension. This flexible coupling mirrors the instantaneous deflection of a tendon and consequent stretch of the muscle.

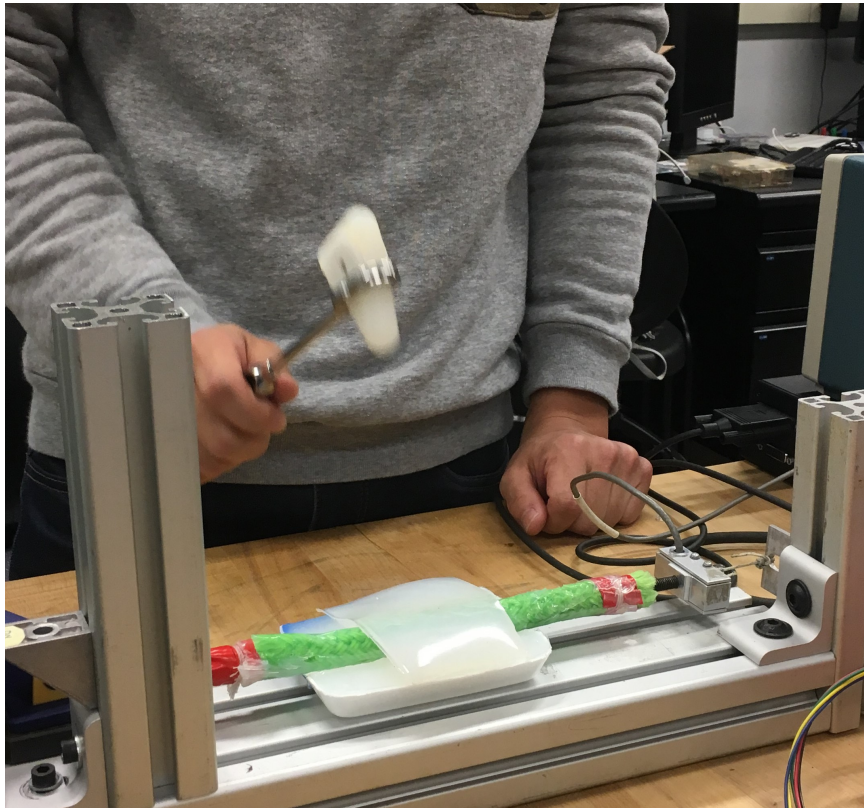


Figure 2.16: Human operator experimental setup

2.3.2 Human operator experiments

The above automated tapping experiments were repeated with human operators in order to compare intensity and timing variability. The experimental setup for these experiments is shown in Figure 2.16. Three human operators performed a series of 500 taps at approximately 1Hz to the apex of the silicone tendon. Operators did not have any formal experience or training in tendon reflex elicitation. Prior to beginning the experiments the operators were given a familiarization period in which they were able to view the output of the force sensor during tapping to gauge force levels. Operators were asked to attempt to maintain constant force between the taps, but were not provided force feedback after the familiarization period. These conditions mimic those that occur in most therapeutic uses of the tendon reflex, stimulation intensity and interval are ideally constant, but there is an absence of feedback to clinicians about their performance in these aspects [13].

2.3.3 Human and robotic stimulation variability

While impact force is an important factor in the evaluation of somatosensory input from a tendon tap, the actual sensory input stems from the stretching of muscle spindles, not the direct impact to the skin. To evaluate the sensory stimulation in a more realistic manner, the mock tendon in Figure 2.15 was coupled with a force transducer along the tendon axis. The maximum force during tapping was used here as a proxy for stimulation intensity, as stretch response is correlated with stimulation force parameters [14]. Maximum forces for each of the 3000 robotic taps and 1500 manual taps were recorded and compared. The force measured is the tension force in the tendon during the tapping, not the force at the tip of the hammer. While it is likely that both the force profile during impact and the maximum force are related to the stimulation intensity, in this work, maximum force is used.

2.3.4 Hammer velocity measurement and tapping energy calculation

To gain more insight into the hammer stimulus intensity at the three levels used for the above experiments, a second set was carried out to measure the hammer energy prior to impact. 100 consecutive taps were carried out at each of the three levels above, with position recorded by a magnetic position sensor (Fastrak, Polheums, Vermont, USA). The magnetic position sensor was mounted directly to the rubber hammer head, with one axis along the direction of motion. The same mock tendon was tapped, in order to maintain consistency in the energy at impact, as this is a function of the angular travel during tapping. The change of the tangential axis position was used to find the maximum velocity, which is the velocity at the sample prior to impact. For each of the three settings, the mean maximum velocity was found. With the known hammer length, angular velocity was calculated. The angular velocity along with hammer mass and dimensions were used to compute the kinetic energy by:

$$K.E. = \frac{1}{2}I\omega^2. \quad (2.6)$$

Where ω is the angular velocity and I is the moment of inertia. I was approximated as that of a uniform rod with a point mass at one end with the axis of rotation about the opposite end. I is then,

$$I = \frac{1}{3}M_r l^2 + M_h l^2 \quad (2.7)$$

where M_r is the mass of the handle, M_h is the mass of the hammer head, and l is the length of the hammer. The linear velocity and energy at impact for each of the three settings is shown in Table 2.2. From this it is clear that the three different constant torques chosen produce varying stimulus intensity levels. For the torque range chosen, energy at impact varies by 160%. Although the hammer kinetic energy prior to impact cannot be directly correlated to a specific force felt by individual muscle spindles, it provides a qualitative value to compare intensity between the three chosen levels.

Table 2.2: Velocity and kinetic energy of automated hammer

	Velocity [m/s]	Kinetic Energy [J]
Soft	1.93	0.079
Medium	2.25	0.107
Hard	2.45	0.127

2.3.5 Tapping tension force

Tension force was recorded during all tapping trials, with results normalized to the mean of the hardest automated taps. The tapping force results are shown in Figure 2.17 and Table 2.4. The results clearly show that the tapping robot is capable of delivering significantly more repeatable stimulation force, particularly at the higher end of the forces provided. The SSEP results shown later indicate that the sensory response to larger stimulation forces is higher, so these may be more important therapeutically. Coefficient of variation was used to determine variability, instead of standard deviation, because of the large difference in the mean force between manual and automated tapping.

Table 2.3: Force evaluation results

	Coefficient of Variation
Robot Soft	0.106
Robot Medium	0.054
Robot Hard	0.055
Human 1	0.108
Human 2	0.106
Human 3	0.178

2.3.6 Expert and novice stimulation intensity variability

As described above, the force applied by the tendon hammer to the tendon is the mechanism for eliciting the DTR. Stimulation variability is a confounding factor for the diagnostic utility of the procedure. In order to ascertain the potential for laypeople to perform this procedure remotely, manual stimulation variability was compared between an expert and a non-trained operator.

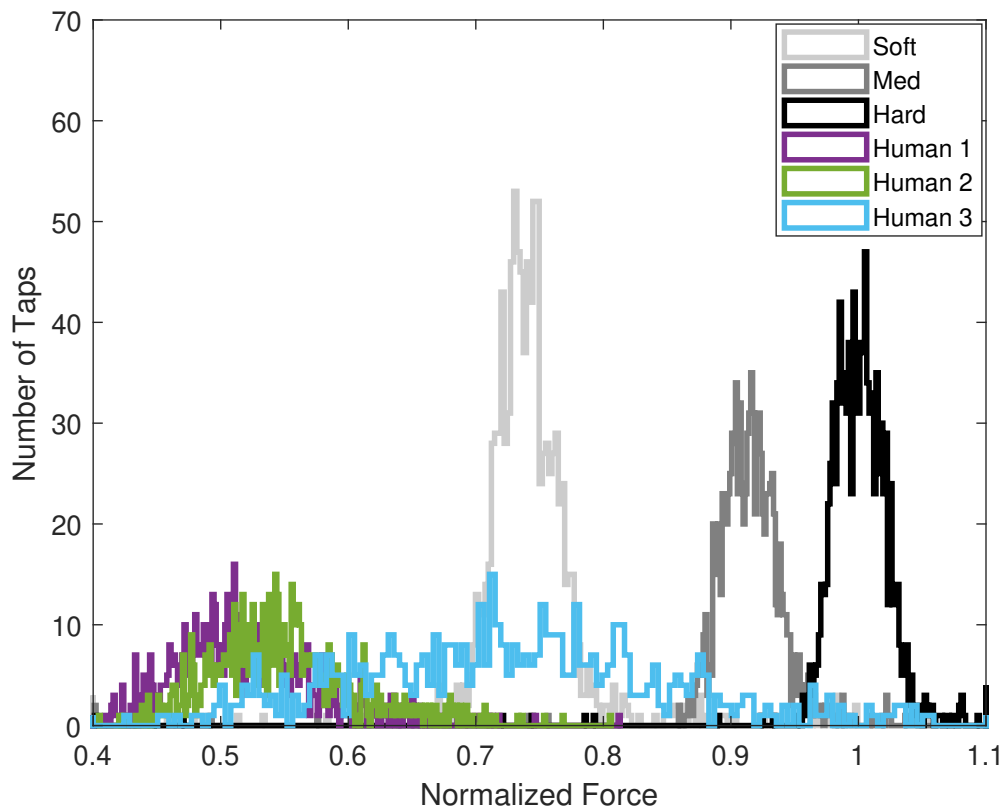


Figure 2.17: Force result histogram, maximum force normalized to the mean of the hard automated taps

A trained clinician performed a series of 50 taps with the instrumented medical hammer to a latex rubber tendon analog. The tendon analog was used to eliminate variability due to human subject movement or physiological factors. Acceleration was recorded from the embedded sensor at 100Hz. The repeatability of stimulation intensity was measured and compared. The relative standard deviation (RSD) of peak deceleration during impact was the metric used for comparison.

The performance of a novice operator in the same simulated tapping experiment was also assessed. A series of 50 taps to the surface of the latex rubber tendon was conducted, with the RSD of peak tapping acceleration again being the primary metric of comparison.

Tapping variability can be quantified in a number of ways. This evaluation concerned variability in the intensity of stimulation. In comparing tapping variability, the results in Figure 2.18 show comparable distributions between expert and novice accelerations, both before and during impact with the rubber tendon analog.

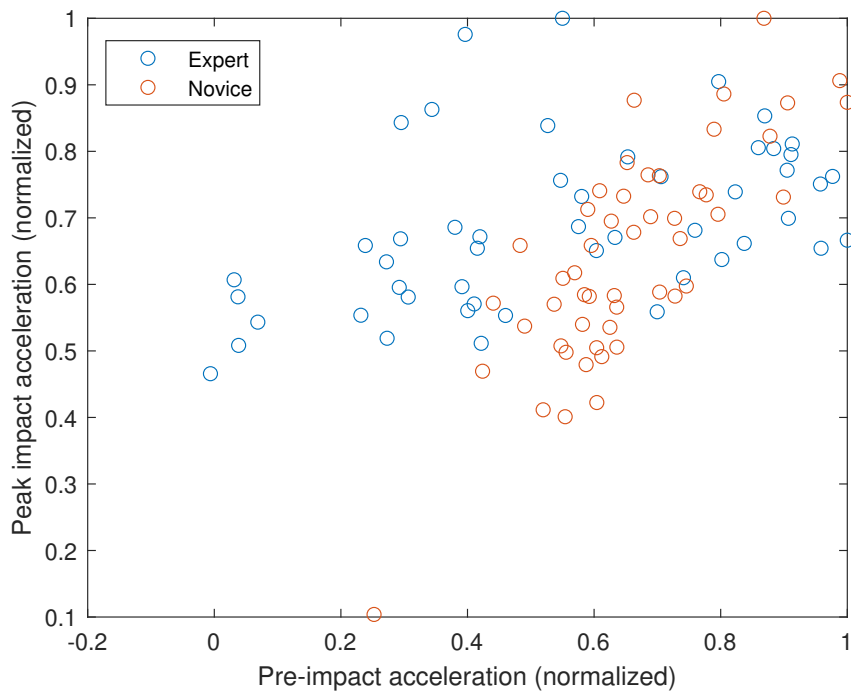


Figure 2.18: Expert and novice tendon tapping acceleration variability

Expert impact deceleration RSD was 18% while the novice deceleration RSD was 25%.

The variability in acceleration indicates that similar levels of variability in tapping force should be expected for expert tendon tapping. Novice impact acceleration variability was larger than the expert's, but still suitable for tendon reflex elicitation.

2.3.7 Timing evaluation

Impact timing is a critical factor in the therapeutic use of tendon tapping, because the theorized mechanisms behind DTR stimulation based rehabilitation requires temporal pairing with cortical stimulation [12, 13].

Impact time was calculated from force measurements, with the peak force times between each tap compared. While this peak force time relative to impact time may vary depending on the location and intensity of the tap, the interval between peaks should be constant for a given location and intensity. Variability in the time between hammer contact and maximum force measurement is thus included in the timing variability reported. The impact time was also found from the acceleration measurements, but using impact time instead of maximum force produced negligible differences in variability. Peak force time interval was then used as the metric for timing performance. This interval was computed for each trial for both the human operators and all three robot intensities.

Table 2.4 and Figure 2.19 show the results of the robot timing evaluation. The bin size for the human taps in both Figure 2.19 and Figure 2.17 is double the size of that for the robot taps, making the heights directly comparable. The distribution of robot stimulus timing is better than the manual tap timing, with a significant difference in the standard deviations shown in Table 2.4 ($p < .05$). While the manual results are widely distributed, the robot taps have similar distributions at all 3 intensity levels. This indicates that the tapping device can provide differing levels of stimulus with no change to timing interval or distribution.

Although the larger timing distribution for the human operators is clear from both Figure 2.19 and the larger variability in Table 2.4, it is also instructive to look at the timing

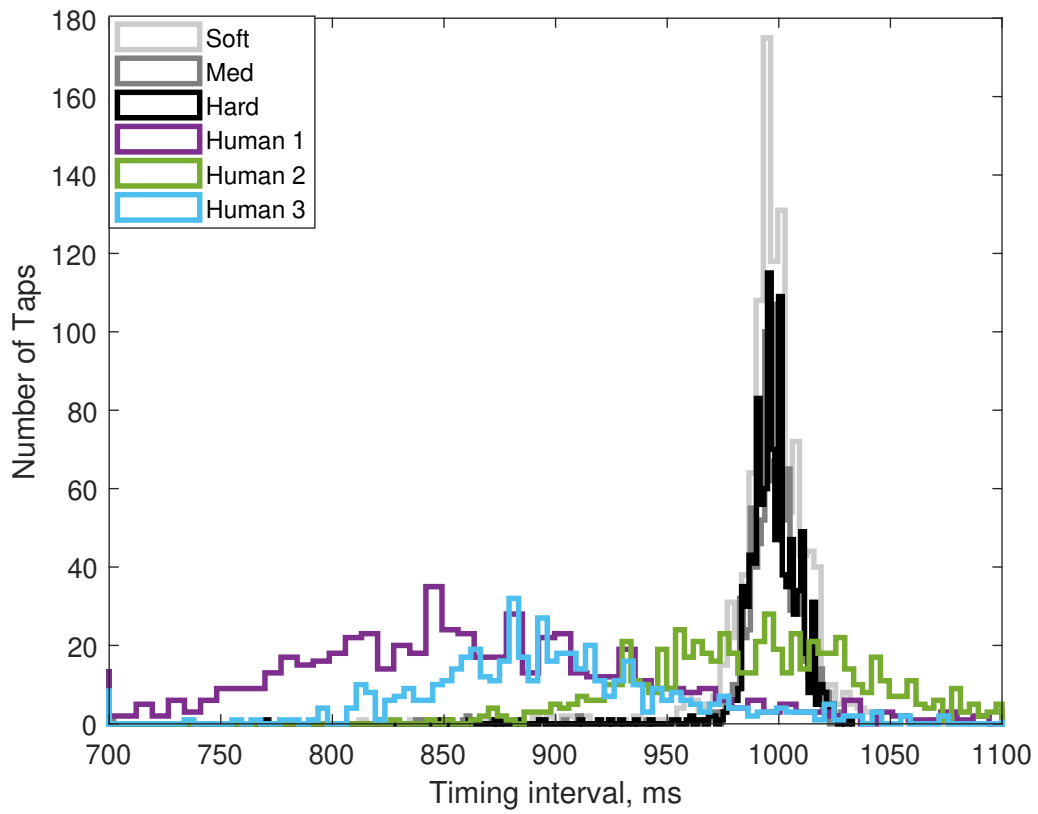


Figure 2.19: Timing result histogram

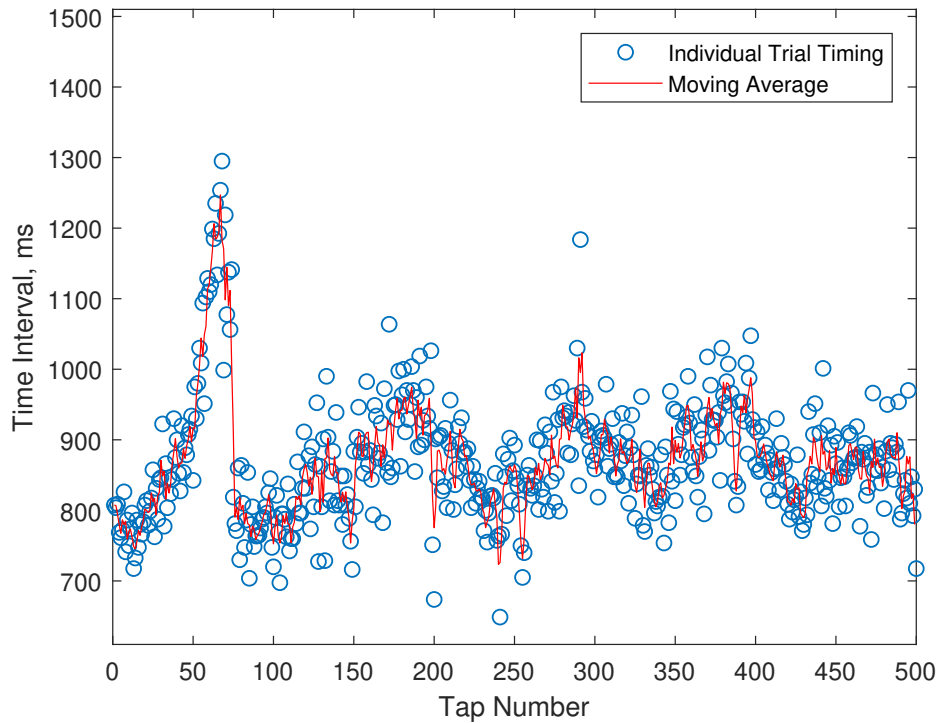


Figure 2.20: Single operator tap intervals

variability over the course of 500 taps. The timing results for an individual operator are shown in Figure 2.20. Time series data for the other two operators demonstrate a similar trend, with a Wald-Wolfowitz run test determining that the timing was not random ($p < 0.001$) in all three manual tapping trials. These results agree with prior work demonstrating difficulty in timing generation for a RFE analogous task [15].

The moving average of the time interval varies over the course of the short experiment. Because the rehabilitation techniques involving tendon stretch stimulus rely on precise timing and intensity control [12, 13], the variability over time may actually decrease the effectiveness. Inhibition can occur with incorrect timing between stimulations. If a meaningful number of stimulations are given at the right intensity, but incorrect interval, inhibition of the desired response could be induced, making subsequent stimulus less effective and even harming the patient.

Table 2.4: Timing evaluation results

	Standard Deviation [ms]	Mean [ms]
Robot Soft	18.8	996.3
Robot Medium	16.9	996.5
Robot Hard	17.9	996.3
Human 1	109.8	876.1
Human 2	58.8	994.3
Human 3	62.5	898.4

2.4 Diagnostic uses of the DTR

The original application of DTR stimulation in medicine was to evaluation of the associated reflex arcs, this is still the most common usage today [1]. The presence, strength, and timing of DTRs is commonly assessed as part of the evaluation of a multitude of chronic and acute conditions. The deep tendon reflexes are stimulated through an impact from a rubber tipped hammer, and observed visually, or physically in the case of reduced amplitude. The response can be used as a rapid test of spinal lesion level, as the sensory neurons synapse onto the motoneurons at known spinal levels. The reflex is also measured as part of the standard neurological exam. A number of conditions such as hypothyroidism, peripheral neuropathy, myoclonus and parkinsonism affect the reflex response [16, 8, 17]. While it is clear that the DTR is a useful clinical sign, the repeatability of this measurement in it's current form has been called into question [18].

The DTR exam involves manual stimulation of the reflex, then scoring or grading of the reflex on an ordinal scale. Essentially, the diagnostic DTR consists of a reflex stimulation portion, and a reflex observation portion. Clinicians rely on experience and training to complete both of these halves of the exam. Because two humans are involved in the procedure, there are numerous sources of variability in both the stimulation and grading sides of the response. Variability in the patient response both between patients and in the sensory response in an individual is common. However, another potential source of variability is the clinician performing the exam, both in terms of the stimulation intensity and

the reflex grading. Human variability in reflex elicitation is investigated in the preceding section, with novice and expert tapping found to be relatively comparable in terms of intensity variability. The performance of novices in grading reflexes was also assessed and compared to expert grading performance.

2.4.1 Layperson grading

Human subjects (N=9, 2 Expert, 7 Novice) were recruited to validate the ability of laypeople to grade reflex responses accurately, and to compare to trained expert performance. Experts had both formal training and clinical experience in DTR assessment. Reflex grading took place in a virtual environment, with video training and evaluation. All training and testing took place in an online, remote format. Participants were first given a training video with 3 repeated examples of a tap and a response, the impact location of the tendon hammer on the bicep tendon was obscured in all cases. The rating scale employed was the National Institute of Neurological Disorders and Stroke (NINDS) 0-4 scale. After reviewing the training video, participants were given 25 unlabelled tap videos to score, 5 for each of the 5 grades. Mean and median scores for each of the 5 were tabulated for each participant. All data collection took place under an institutionally approved protocol (GT# H20393).

An example of the survey questions presented to research participants is shown in Figure 2.21. Each survey question provided the 0-4 scale with descriptions from the NINDS scale. The grades assigned to each video example were confirmed by a clinical expert prior to beginning the human grading surveys.



- 0 - Reflex absent
- 1- Reflex slight, less than normal, including a trace respons
- 2- Reflex in lower half of normal range
- 3- Reflex in upper half of normal range
- 4- Reflex enhanced, more than normal, including clonus

Figure 2.21: Example survey question with obscured hammer impact and 0-4 grading choices.

Aggregate results for each reflex grade from the reflex grading survey are shown in Figure 2.22 and Table 2.5. The mean error across all 7 of the novice participants and 25 reflex videos graded was 0.205 on the 5 point scale. However, mean error provides only one descriptor of the results. A more clinically relevant statistic may be the number of instances

Table 2.5: Novice survey results by reflex grade

Ground Truth	0	1	2	3	4
Correct Responses (%)	97	94	69	71	71
Median Selection Accuracy (%)	100	100	71	86	86
Mean Selection Accuracy (%)	100	100	86	86	86
Responses Error ≤ 1 point (%)	100	100	100	100	97

in which multiple trials would still result in an incorrect grade. In that case, taking the mean and median of all 5 trials for each participant results in an incorrect grade in just 3 and 4 of the 35 cases respectively. Both experts who completed the survey did not have any errors. There was a significant difference ($p < 0.05$), between the number of errors in the 0 and 1 reflex grades and the 2 and 3 grades.

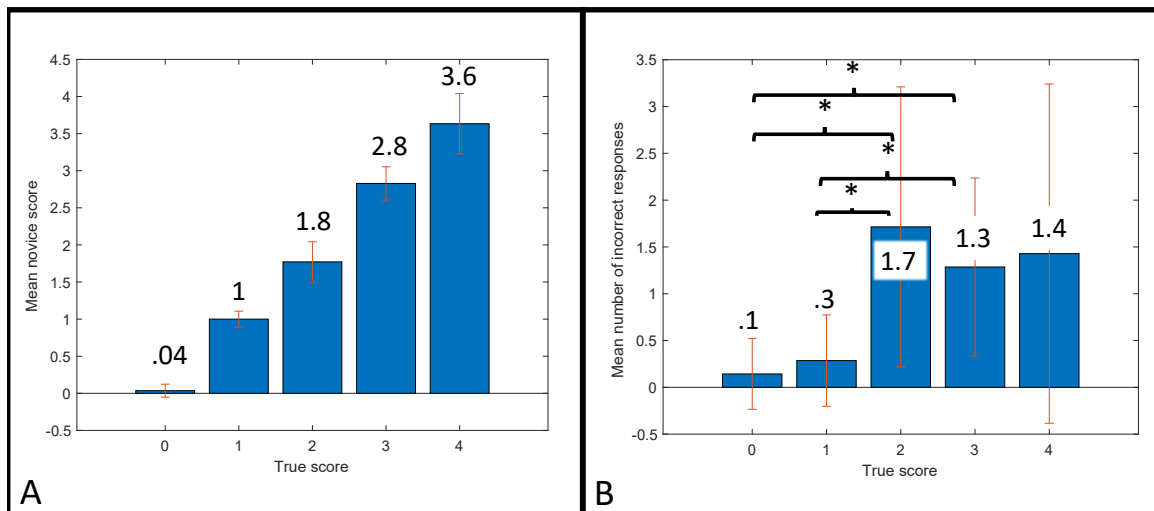


Figure 2.22: Survey results A) Mean score for each true score, B) Mean number of errors for each true score, * represents $p < 0.05$.

Although novice performance is not perfect, the results indicate grading errors after a number of trials are relatively rare. Most importantly, out of a total of 175 novice graded reflexes, only a single response was more than 1 point away from the ground truth. The significant difference between errors in the 0 and 1 groups and the 2 and 3 groups indicates

that areflexia or below normal reflexes are easier for novices to catch than the normal range. Although a larger sample size is needed before clinical deployment, it is important to consider the range of conditions that can cause reflex responses to be on the lower end of the scale. Only a single reflex, the bicep tendon reflex, was evaluated, however it is expected that the novice performance in grading other reflexes would be similar.

Although this portion of the work has centered on the reflex exam being performed in a completely remote manner, with both tapping and grading done by novices, an important result emerged from the survey results. Both experts were capable of grading reflexes from video with 100% accuracy. An alternative procedure where the novice provides the elicitation via smart hammer and assistive application, and a video of the response is sent to the clinician may deserve further study and development. As the COVID-19 pandemic continues to dictate the use of telemedicine, this initial novice human subjects work provides experimental indications that remote implementation of the tendon reflex examination is possible.

2.4.2 Tapping assistance application

One of the primary goals of this aim is to produce a smart tendon hammer system that can provide realtime feedback to the user about the nature of the stimulus they are providing. This is embodied in the smart hammer and mobile application developed and described here.

The remote DTR evaluation workflow and smart hammer system is shown in Figure 2.23. The system is intended to enable physical separation between patient and clinician, with a patient's caretaker serving as the novice participant delivering the tendon tapping and grading the reflex response. A smart hammer streams tapping accelerations to the mobile application, which then provides feedback to the operator about the tapping location. Once grades are recorded, they can be sent along with the associated tapping data to a clinician for review.

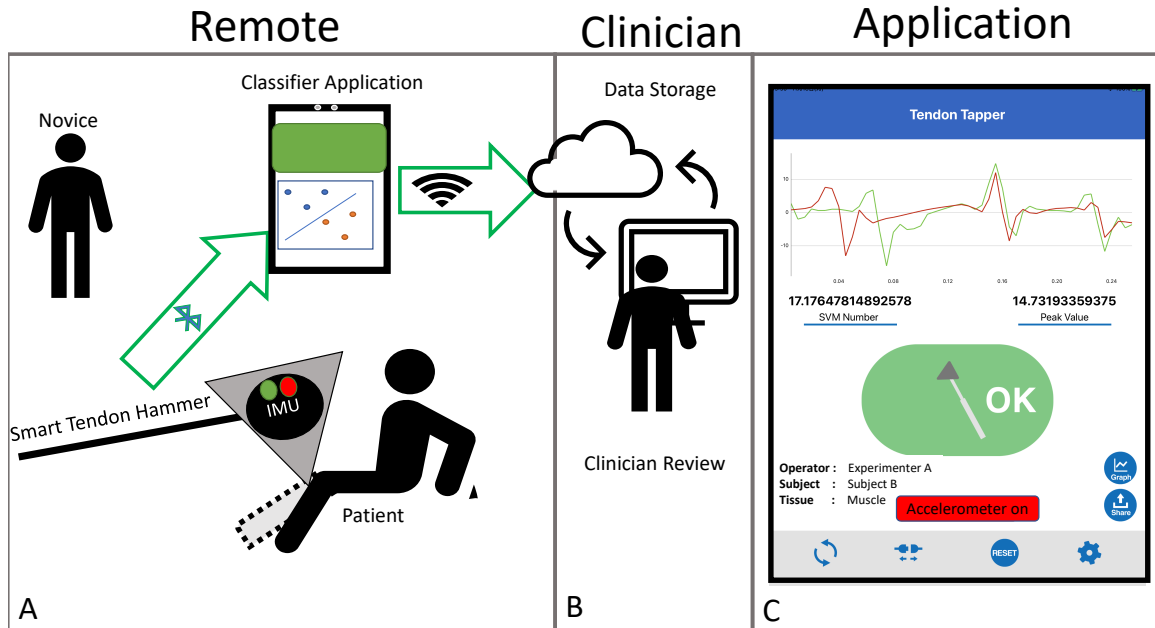


Figure 2.23: Proposed remote deep tendon reflex exam system A) Remote portion with smart hammer assisted reflex elicitation and grading, B) Clinical portion, with clinician receiving assessed scores and communicating with patient, C) Tapping application screen.

This method of remote tapping contains key differences from the standard tapping procedure that clinicians perform. In the traditional clinical tapping by an expert, this characterization of stimulus is done through experience and “feel”, primarily based on visual location of the impact site and the rebounding of the hammer in the clinician’s hand. The proposed system utilizes the smart hammer to collect and analyze the hammer acceleration in order to provide the same characterization of stimulus to a novice who lacks the experience and training of an expert.

2.4.3 Tendon hammer design and evaluation

A smart tendon hammer was used in the course of this work, and is shown in Figure 2.24. The hammer is a modified commercially available taylor reflex hammer (NITI-ON, Chiba, Japan) with a silicone head, stainless steel handle and wireless Inertial Measurement Unit (IMU) (Mbient Labs, San Francisco, USA) situated in a polymer case in the head. The IMU records 3-axis acceleration at up to 800Hz for data logged to the onboard memory,

or up to 200Hz for data streamed directly to a mobile device. The addition of the IMU to the commercial hammer requires only the removal of a disc of material out of the silicone head and inserting the IMU case, which can be done without any precision machining. The application is shown in Figure 2.25. Both the application screen and the indicator

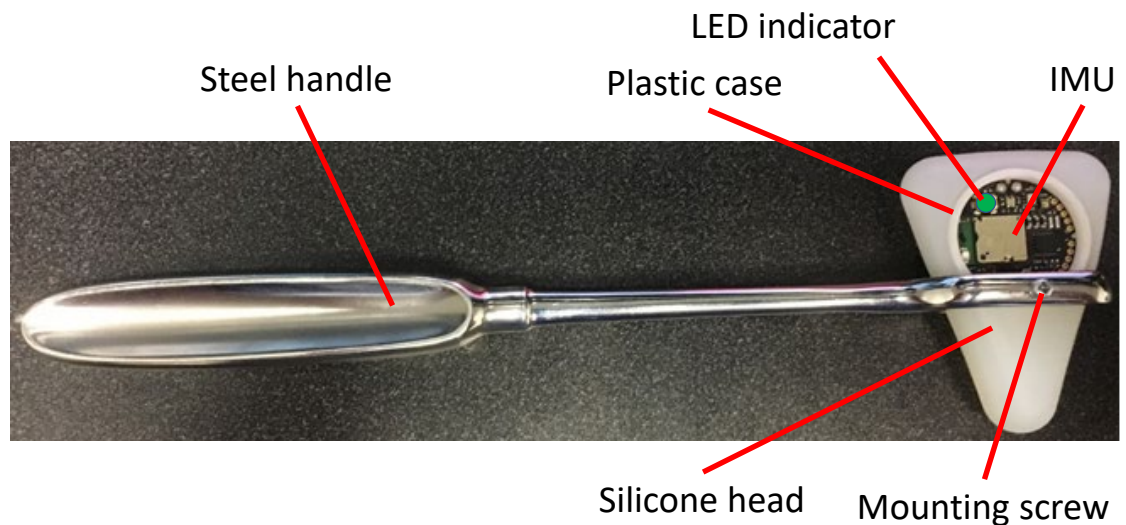


Figure 2.24: Picture of the smart tendon hammer used throughout this work.

light shown in Figure 2.24 turn green or red to indicate successful or incorrect tapping respectively. The icons and indicator light make it easy for novices to quickly recognize when they have performed the tapping incorrectly, regardless of where their attention is focused.

The hammer is manufactured by removing material from the silicone hammer head and inserting the plastic case containing the IMU. This material removal can be done by conventional milling, or through a stamping process with a thin metal tube of the appropriate diameter. Because of the elastic nature of the silicone, dimensional tolerances during machining are unimportant.

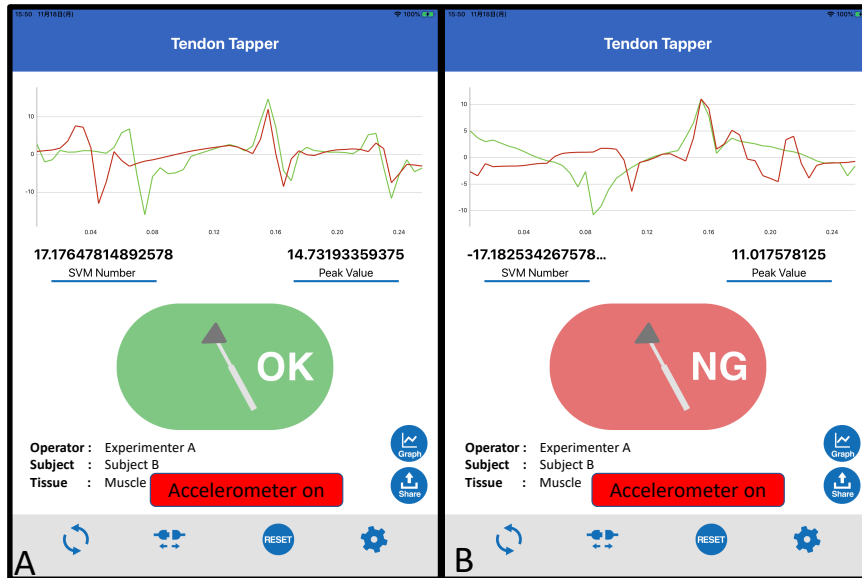


Figure 2.25: Tapping feedback and data collection application, A) Result after successful tap, B) Result after an incorrect tap, the red and green lines represent the acceleration of the most recent incorrect and correct taps respectively.

2.4.4 Materials cost and distribution

The Achilles tapping results and the associated statistical analysis demonstrate that sufficient information for classification is contained in the 100Hz acceleration signal. This has significant benefits for a distributed and remote method of DTR assessment. The 200Hz bandwidth allows for the use of relatively cheap IMUs as well as standard mobile phone data collection. The process of retrofitting a standard silicone Taylor hammer with an IMU requires only the coarse removal of silicone material to accommodate the IMU case, without any high tolerance machining operations. The ideal tool for communicating with the wireless IMU is a mobile application, as this is easily distributed, and does not require hardware beyond common mobile devices. With distribution of the devices to individuals requiring a DTR exam, physical proximity between patient and clinician is precluded, and sterilization of the hammer between uses is not necessary, because the low cost enables a one device per patient paradigm.

2.4.5 Application design and functionality

The mobile application developed here serves to classify tapping data directly from the hammer and provide feedback to the operator, novice or clinician. In the past, this application was designed primarily for research users, the version presented here has been adapted to aid novice users. The interface has been streamlined and simplified to avoid confusion. In addition to the tablet interface, LED indicators on the hammer body itself now indicate the success or failure of the prior tap. A diagram of the intended use is shown in Figure 2.23. The main function of the application is to stream acceleration data from the tendon hammer, detect and classify tendon strikes, then provide binary feedback in the form of a red or green indicator. Although much more information can be recorded, classification results are of the most use to a novice attempting DTR evaluation. The application allows user input of physiological information, as well as import of trained classifiers. These SVM classifiers take the form of a string of parameters defining a hyperplane, that are then used to classify each tap as either on target or incorrect. The development and implementation of the classifiers is described in subsection 2.2.8.

2.5 Therapeutic uses of tendon tapping

Although the vast majority of prior work on the DTR has been focused on diagnostic uses, there are many potential therapeutic uses as well. From the diagram in Figure 2.1, it is clear that there are both spinal level and cortical level responses. Therapeutic uses of the DTR typically focus on the cortical sensory response, rather than the spinal level response and muscle activation. Technically, DTR refers only to the reflex response, not the sensory component in the brain, however, in this work will continue to use DTR to refer to both, as it is functionally impossible to stimulate one and not the other unless the spinal cord is severed.

2.5.1 Paired response therapies

While the tendon reflex is distinct from the evoked response measured in the sensorimotor cortex resulting from the same stimulus, they are evoked in the same way, and can be observed concurrently. The tendon stretch response was initially thought to be exclusively spinal in nature, the cortical component is now well known [19, 20]. Somatosensory evoked potentials (SSEPs) capture the sensory response to peripheral stimulation, including tendon tapping, in the brain. SSEPs are used to measure the sensory response to peripheral stimulus through recording and time averaging of Electroencephalography (EEG) measurements. The most common method of stimulation for SSEPs is by transcutaneous electrical stimulation (TES) [21], however SSEPs are present following tapping of the skin, tapping of the tendon and stretching of the muscle[22].

The relatively few studies on SSEPs evoked by mechanical stimulation of the stretch response noted important latency and amplitude differences [23]. While this and other early work measured the SSEP induced by stretching of the target muscle, the stimulation was not provided in the clinically typical way, but by rapid joint torque changes[23, 24]. In practice, stimulation of the tendon stretch response is done via sharp impact with a tendon hammer, or manual pressing of the tendon by the therapist [9, 13]. It is important to measure the cortical response to the actual clinically used stimulation.

While electrical stimulation intensities can be compared between subjects by normalizing to motor twitch or perceptual threshold, there is not currently an analogous measure of intensity for mechanical stimulation. This lack of a clear stimulus intensity metric prevents comparison between subjects, and complicates systematic elucidation of intensity-response amplitude relationships.

Tendon stretch response elicitation has shown potential in augmenting the paired associative stimulation (PAS) stroke rehabilitation technique [15]. Wolters et al. previously utilized the N20-P25 SSEP complex to evaluate the effect of PAS timing on neural plasticity [12]. The latency of the complex is a critical factor for the clinical use of PAS, as

inhibition and excitation can occur with changes of even 15ms in timing [12].

It is also common clinical practice to stimulate the tendon stretch response during many other functional rehabilitation exercises, with limited quantitative evaluation. The theorized mechanism for therapeutic benefit is Hebbian learning. In this case, Hebbian learning is induced through stimulation of the somatosensory system (muscle spindle afferents), coinciding with motor neuron excitation (Either TMS or therapist provided instruction) [25]. Again, as with mechanically induced tendon response SSEPs, there is a lack of repeatable or known mechanical stimulus intensity. In addition, the relative timing of these two stimulations is critical to the success of PAS and other therapeutic techniques [12, 25].

In order to further develop PAS and other techniques involving mechanical tendon stimulation, it is critical to understand the differences between SSEPs evoked by electrical stimulation and mechanical tendon stimulation, and the effect of changes in stimulus intensity. Mechanical stimulus produces a dispersed afferent volley in comparison to the impulse response to electrical stimulation, a visual representation of this difference is shown in Figure 2.1. While this has been known since at least 1983 [26], and electrically induced SSEPs were recorded even earlier [27], limited work investigates the mechanism for this diffuse firing or its impact on SSEPs. However, the diffuse firing is in line with prior findings [15] that mechanically induced stimulation results in a larger time window for successful PAS.

Automation of this impact is a critical first step in evaluating the somatosensory response to standard tendon reflex elicitation. The necessity of automated tendon tapping was shown through the comparison of human tapping and automated tapping. Both stimulation intensity and tap timing were shown to be less variable with the automated device when compared to human operators. The automated device is capable of varying stimulus intensity, this capability was used to compare SSEPs evoked by two different mechanical stimulus levels to two different TES stimulation levels in a single subject.

2.5.2 SSEP modulation

A single healthy subject with no history of neurological impairment participated in the evaluation of evoked potentials. All stimulation and recording followed an institutional review board approved protocol (H14191). The subject was in a supine position, with the head slightly elevated (low Fowlers' position). The subject was given a fixed visual target in order to maintain alertness and reduce head movements. The neck was supported as shown, to reduce muscle activation during data collection.

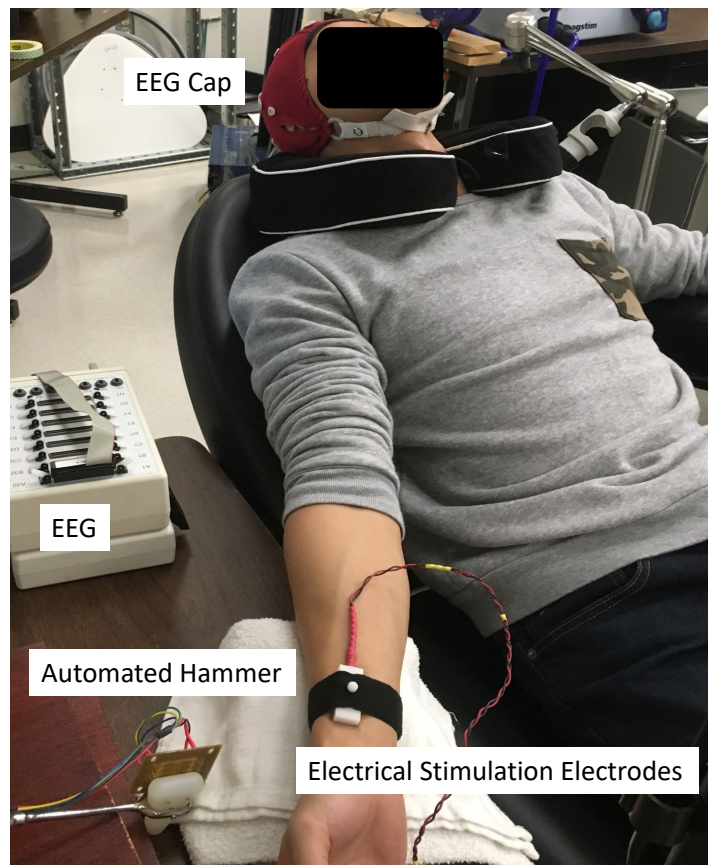


Figure 2.26: SSEP measurement conditions

Both electrical stimulation and mechanical stimulation via reflex hammer were conducted. A constant current stimulator was used (DS7AH, Digitimer, United Kingdom). Electrical stimulation was targeted to the right median nerve, with a standard electrode pair at 2cm distance. A pulse width of 100 μ s was used for both stimulation levels. Elec-

Table 2.6: SSEP stimulus intensity

Electrical	300 % Perceptual Current	Motor Twitch Current
	6.3 mA	15.3 mA
Mechanical	Low level	High level
	.079 J	.127 J

trode placement was at the location of minimal stimulus to induce the H reflex (motor twitch). Standard skin preparation was done prior to finding the perceptual and motor twitch thresholds. During SSEP measurement, current was set to 300% of the individual perceptual threshold as well as the individual motor twitch threshold. The maximal electrically evoked SSEP occurs around the sum of the motor twitch threshold and sensory threshold [28], however, for subject comfort, a lower stimulus intensity was used. The stimulus currents are listed in Table 2.6. 500 stimulations were done at both of the currents shown, the interval between stimulations was approximately 0.5s, for experimental expediency. The lower current stimulations were performed first, with a 5 minute break before the second, higher current, set of stimulations.

Mechanical stimulation was done via the instrumented and automated tendon tapping robot. Tapping was targeted to the right flexor carpi radialis (FCR) tendon. The tapping robot uses a DC motor to drive the silicone rubber hammer. Acceleration of the hammer was synchronized with EEG recording for time averaging. Synchronization of the hammer was done via trigger pulses sent from the DAQ (1401, Cambridge Electronic Design, Cambridge England) to the trigger input of the EEG (ActiveTwo, BioSemi, Amsterdam, Netherlands). Two different stimulation energy intensities were used, with levels shown in Table 2.6. Mechanical stimulations were done at a 1Hz frequency, with 250 stimulations done at each of the two levels.

Electroencephalography (EEG) was used to record the evoked potentials. Recording sites were chosen according to the international 10-20 convention [29]. Fz was the reference, and SSEPs were recorded from Cp3, 2cm posterior to C3 following a prior study of TES evoked SSEPs [12]. Results were trigger averaged to stimulus onset time, accelera-

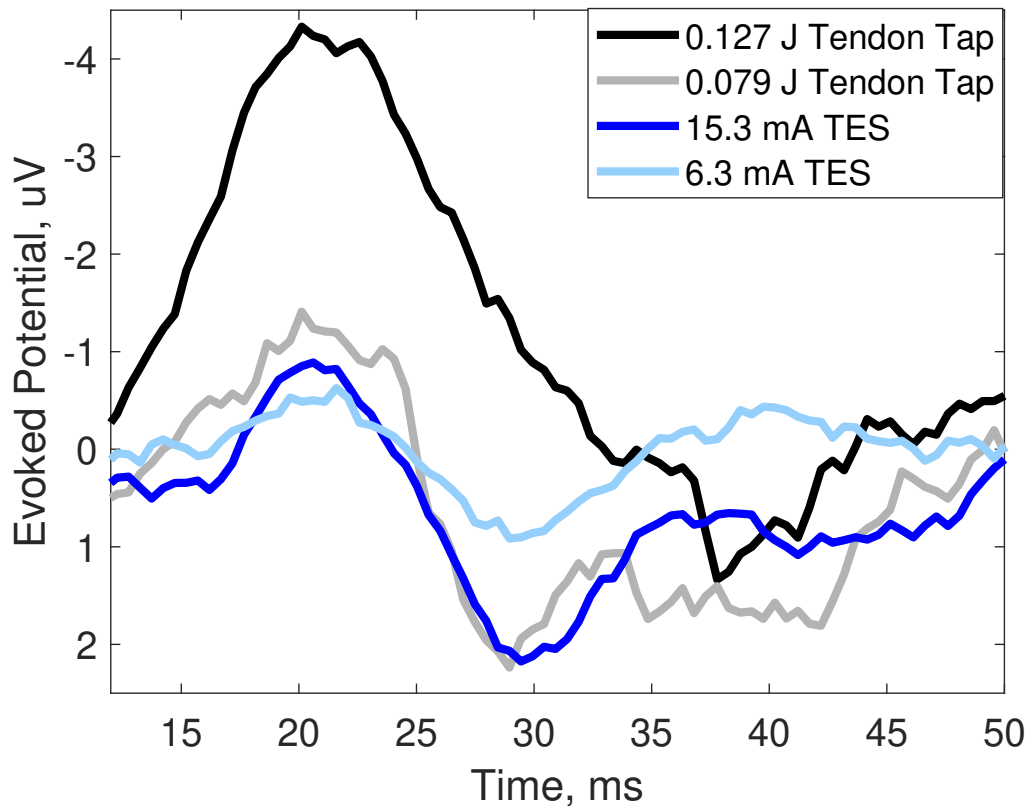


Figure 2.27: Single subject SSEP results

tion indicating impact for the mechanical stimulations and stimulus delivery time for the electrical stimulations. Signals were bandpass filtered to exclude both low frequency drift and high frequency noise. The TES evoked potentials were filtered with a lower cutoff frequency of 1Hz, while the lower cutoff of the mechanically induced SSEPs was 20Hz, due to the electromagnetic noise of the DC motor. The upper cutoff frequency was 1000Hz for both stimulation modalities.

Figure 2.27 shows the SSEP results. The electrical stimulation results shows the characteristic result reported by Wolters [12]. The mechanical stimulation evoked potential have both larger amplitudes and a broadened N20 peak when compared with the TES evoked potentials.

While a direct comparison to previously published results is difficult to make for the FCR tendon tapping response, the time averaged results generally agree with the known

Table 2.7: SSEP peak-peak amplitudes

	N20-P25 Amplitude [μV]
6.3 mA TES	1.55
15.3 mA TES	3.07
0.079 J Tendon Tap	3.65
0.127 J Tendon Tap	5.63

mechanism of distributed Ia fiber firing during tendon tapping [26]. The primary difference between electrical and mechanical stimulation is the temporally distributed nature of the Ia firing in tendon tapping, likely leading to the broadened peaks observed in Figure 2.27.

Table 2.7 gives the peak-peak amplitudes of the N20-P25 wave. For both electrical stimulation and tendon tapping, increases in stimulation intensity corresponded to an increase in the amplitude. This change in the amplitude indicates that the tapping robot is able to modulate the SSEP amplitude by adjusting the energy at impact.

The results reported encompass only a single healthy subject, but support further investigation of the tendon stretch response for rehabilitative purposes. The distributed nature of the N20-P25 peaks in particular may help to relax the strict timing demands necessary for paired stimulation techniques. In addition, it is clear that amplitude of the response changes with stimulation intensity. In the future the ability to modulate SSEP amplitudes may play a role in the development of new rehabilitation techniques involving tendon stimulation. Appendix A details some preliminary work towards this goal.

2.6 Aim 1 discussion

This chapter compared automated and manual tendon tapping, showing that automated tapping produces significantly better timing repeatably, as well as the ability to modulate stimulus intensity. The variable stimulus intensity during automated tapping was compared with electrical stimulation to measure SSEPs in a single subject, with the peak amplitudes modulated by stimulus intensity.

The comparison between automated and manual tapping demonstrated the significant

performance advantage of the automated tapping device. The robot demonstrated statistically significant improvements in timing compared to 3 human operators. In addition, the distribution of timing errors is non-random for the human tapping, which may have important impacts for therapeutic uses of tendon tapping. The robot demonstrated the ability to vary stimulus intensity, both in terms of tension force and hammer energy at impact.

This variable intensity property was used to compare SSEPs at 2 different intensity levels for both mechanical and electrical stimulation. Although only a single subject was evaluated, important differences in both shape and amplitude of the evoked potentials were noted. Varying the intensity of tapping appeared to modulate the amplitude of the SSEPs. The developed device and reported results both indicate the therapeutic potential of variable intensity tendon tapping.

The classification of tapping locations via SVM was reported, and implemented in a remote tapping application. The increased move to remote delivery of healthcare would be aided by further development and distribution of similar devices.

2.7 Future work

Completed work has demonstrated learned methods for tapping characterization [30], and the modulation of SSEPs with stimulus intensity [31]. More investigation of SSEP modulation is necessary to realize the full therapeutic potential of mechanical stimulation. This work treated the SSEP as only the trigger averaged signal after many trials. A start has been made toward the necessary interpretation and prediction of the individual responses in Appendix A.

2.7.1 Alternative models

The performance of the SVM based classification system was sufficient for the development of the assistive application, while the mass-spring-damper mechanical model was also capable of determining impact locations. For the purposes of this work, classifica-

tion accuracy is the primary performance metric, while exact tissue property estimation is not necessary. However, tissue property estimation from tapping impact may be a useful application in the future, and the results and methods developed can provide a foundation for these future developments. The models chosen for evaluation were mostly picked on the basis of simplicity for potential implementation in the mobile application. With tissue property estimation as the goal, models that better fit the impact dynamics should be considered.

The results presented above demonstrate that damping is likely an important factor in the mechanical models. Additionally, the Hertz model assumes small deformations and low friction, which may not fit the interaction between the hammer and skin. Work by Olsson in 2016 presented a large-deformation compensation method for contact between deformable spheres [32]. The key parameter of hardness is likely equal between the tendon hammer and impacted skin, at least for the hammers used in this work. Work on excised porcine muscle tissue has found a Kelvin-Voight model effective for fitting both effective stiffness and damping from experimental data [33]. Alternatively, exponential or polynomial models, while not mechanical, could also be explored with rigorous experimental determination of material properties.

CHAPTER 3

AIM 2: DEVELOPMENT OF A NEW ROBOT MORPHOLOGY FOR HIGH RESOLUTION INTERVENTION IN THE SPINAL CORD

3.1 Introduction

Aim 1 concluded with the investigation of therapeutic uses for tendon tapping to aid in neurological rehabilitation. Although the sensory pathway of the spinal cord is involved in this rehabilitative procedure, the spinal cord itself is not treated, only the brain. The second aim of this work involves the development of a precise image guided robot for direct interventions, including in the spinal cord.

Recent research developments have indicated the potential use of injected stem cells for treatment or mitigation of amyotrophic lateral sclerosis (ALS) and other diseases that affect the spinal cord [34, 35, 6]. It is critical that the cellular material is delivered directly to the site, with minimal targeting error, as cells injected into white matter are likely ineffective [5]. Two options to achieve this accuracy have been used, 1) open surgery, in which the spinal cord and injection site are visually located by the surgeon, and 2) manual MRI based needle positioning [35, 34]. The manual needle positioning method involves an iterative procedure in which the subject is imaged in the MRI scanner along with an adjustable frame. Correct targeting of the injection site requires multiple images, with the subject removed from the scanner each time so that the needle guide can be re-positioned, increasing procedure time to around 6 hours [6].

MRI based injection is preferable to open surgery, because of the ability to locate injection sites accurately and in a minimally invasive manner [6]. However, MRI compatibility places additional constraints on the design of needle positioning robots, particularly in the choice of actuators. Piezoelectric and pneumatic actuators are the two most common

choices.

Pneumatic actuators have the significant advantage of large ranges of motion and simple MRI compatibility, however relatively long transmission lines are necessary and this produces complications with remote sensing and control [36]. Piezoelectric motors are capable of providing high accuracy, but often must be used with a cable drive system because of reported concerns with image artifacts [37, 38]. Remote placement of actuators, even if cable lengths are relatively short, produces additional accuracy and rigidity concerns. Many MRI based needle positioning systems exist, with applications to biopsy as well as injection of therapeutics. Broadly speaking, previously developed systems can be grouped into passive manual frames and active automated positioning systems. Manually adjustable frames have been used with a degree of success to perform intraspinal injections [6]. The system reportedly was fabricated by modifying an existing frame for neurosurgery (Clear-Point SmartFrame, MRI Interventions). While the protocol used to perform intraspinal injections in a porcine model animal was effective, it was extremely time intensive, with pre-operative planning and injection taking 2.5 hours of the total 6 hour procedure [6].

The author is aware of only a single automated needle positioning system targeting the spinal cord as the injection site [39] although a wide range of needle positioning MR robots have been developed [37, 40, 41, 42, 43, 44, 45]. Monfaredi discussed a large number of MR compatible robots, primarily for prostate, brain and breast interventions [44]. The best accuracy of the reviewed robots was 23 μm , however, this system has only 3 degrees of freedom (DOF), insufficient for spinal cord applications [46]. In addition, concerns have been raised about the SNR reduction caused by the actuators when they are located close to the region of interest [38]. A reported parallel plane positioning mechanism utilizing piezoelectric ultrasonic motors demonstrated promising results, but was limited by the necessity of a cable driven actuation system, resulting in hysteresis [37].

One important benefit of a robotic needle guide in comparison with manual systems is the potential for significant reductions in injection procedure times. For example, in a

previous study utilizing manual needle positioning total procedure times were around 4 hours, with trajectory planning and needle insertion taking 2.5 hours [6]. A similar study in humans where surgery to expose the spinal cord was used required a minimum of 3 hours per procedure [34]. In contrast, the prior robotic positioning study required only 10 minutes for each positioning update with a total procedure time of about 70 minutes [39].

Although the MRI sequence used during the injection procedure provides up to 1.0 mm accuracy, the design of a robot with a significantly higher accuracy will allow super resolution (SR) injection. SR algorithms require multiple sub-pixel shifted images to reconstruct a higher resolution image. One SR algorithm that has found success across a number of imaging domains is iterative back propagation [47]. Previously reported SR MRI methods demonstrated promising results by inducing sub-pixel shifts in the scanner field of view (FOV) [48, 49]. However, the mechanics of most MRI protocols preclude the effective use of this type of FOV shift method along certain axis of the image[50]. In contrast, a robot capable of producing 3 dimensional spatial shifts with precision beyond the accuracy of the scanner will enable application of these methods along any image axis. Improved resolution of robot position through super-resolution reconstruction will enable injection repeatability beyond the scanner's imaging limits. Thus, the robot design process undertaken here aims to produce a system capable of accuracy an order of magnitude greater than that of the MRI.

3.2 Robot design

3.2.1 Mechanical design

The planned robot and visual feedback system design is shown in Figure 3.1. The design and control of the robotic system is described in more detail in this section and the next.

The robot design produced is a parallel plane structure consisting of two nearly identical X-Y stages which position two ball joints. Robot design prioritized MRI compatibility and structural rigidity to ensure accuracy and avoidance of contamination of the MRI images

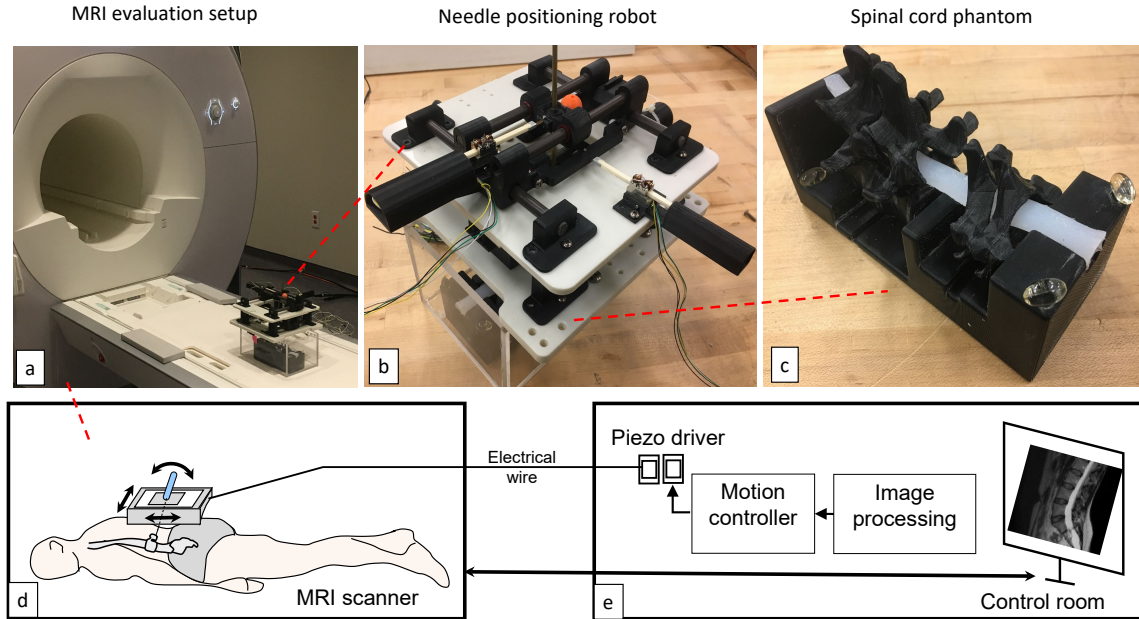


Figure 3.1: MRI visual feedback schematic, a) 3T MRI and robot, b) closeup of robot, c) silicone and ABS spinal phantom produced from CT data [51], d) patient orientation, e) control room diagram

needed for targeting of the spinal cord. A needle guide passes through the center of each ball joint, allowing 4 Degrees of Freedom (DOF) to be controlled. the robot is shown in Figure 3.2. The lower ball joint is fixed to the needle guide, while the upper ball joint allows the needle guide to slide through the center. The actuators are comprised of linear piezoelectric motors.

The Y axis actuator moves the entire X axis assembly along the outer guide rods, while the X axis actuator is mounted to this assembly, and moves only the center ball joint, collar and fiducial. Each actuator is centered between the guide rods, to avoid unbalanced loads on the drive rods. Guide rods are low friction polymer, and sleeve bearings are press fit into the X assembly components and collar to decrease friction.

The only difference between the upper and lower stages is in the diameter of the needle guide hole in their respective ball joints. The lower stage has a press fit, while the upper stage is a free fit, to allow the guide to slide freely. The lower base also has additional features for mounting above the spinal cord phantom used in this study. The full robot

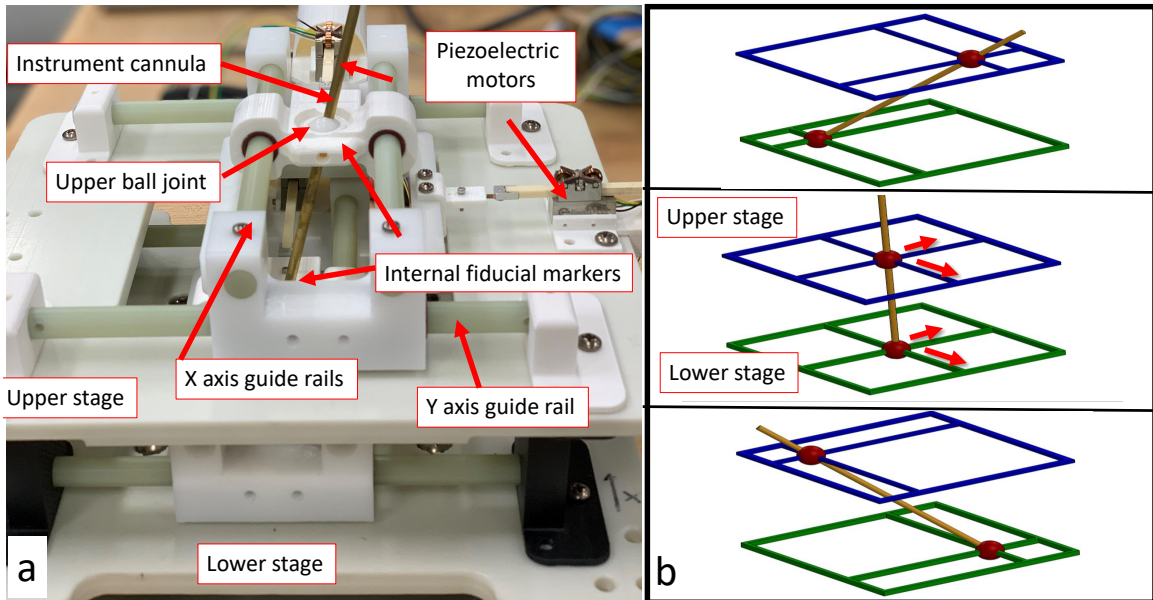


Figure 3.2: Parallel plane robot, a) robot and b) positioning mechanism

is shown in Figure 3.2a. Four rigid brackets connect the upper and lower stages, these brackets also provide the mounting points for the lower stage y axis guide rods.

The primary target for cellular therapeutics in the spinal cord is the ventral horn of the gray matter. Although the spinal cord as a whole is around 12mm in diameter [52], the ventral horn is much smaller, with a cross sectional area near 1mm^2 . For this reason, accuracy of the entire robot and visual feedback system must be better than 1mm. Time is a critical component of this system, as the primary motivation is to improve timing and accuracy of cellular therapeutic injection. The robot and feedback system should require at most 2 positioning updates to reach a desired trajectory, in order to keep scanner time under 15 minutes for the positioning portion of the procedure.

Because the primary materials of the robot will be transparent in MRI, only fiducial markers will be visible in the acquired images. Thus all calibration and control steps will involve the robot fiducials only. The implementation of a robot registration step, to find the transformation between robot and scanner coordinate frames is common, but can be manually intensive or technically challenging [44]. Locating fiducials on the needle axis allows

robot orientation agnostic control, as the configuration is defined only by the fiducials, not necessarily the robot frame itself. By also placing the fiducials into 2 parallel planes, it is feasible to select the image slice corresponding to each plane only a single time, allowing much more rapid acquisition of images.

To avoid remote actuation and the necessity of rotary actuators for controlling rotational degrees of freedom, a parallel plane mechanism was chosen. The parallel plane positioning concept is shown in Figure 3.2b. Both the upper and lower ball joints can move independently, controlling 4 DOF of the needle guide.

The mechanism consists of 2 parallel planar stages each manipulating a ball joint. The cannula runs through these ball joints, by actuating the 4 planar axes, 4 actuated DOF are achieved, the fifth DOF, needle depth, is controlled by the surgeon inserting the needle into the cannula. The sixth DOF, needle rotation, is irrelevant for this procedure. Because the actual distance between the ball joints is dependent on the orientation, the cannula is fixed in lower joint, while the cannula slides through the center of the upper joint.

The robot was fabricated from a variety of MRI safe materials using both conventional machining and fused deposition modeling (FDM) printing. FDM parts were printed in acrylonitrile butadiene styrene (ABS) plastic, while machined parts consisted of acetal resin. The needle guide was cut from 4 mm brass tubing. Fasteners were titanium and nylon. The completed robot is shown in Figure 3.2a.

3.2.2 Kinematics

The forward kinematics of the robot describe the mapping of actuator positions and insertion depth to the position and orientation of the needle tip,

The robot's actuator positions are described by the upper x and y axis positions, x_t and y_t , the lower actuator positions x_b and y_b , and the insertion depth of the needle from the center of the lower ball joint, l , the height between planes h , is 53 mm. R used above in (Equation 3.1), describes the Euclidean norm of the vector between the upper and lower

$$\begin{bmatrix} x \\ y \\ z \\ \theta_x \\ \theta_y \\ \theta_z \end{bmatrix} = \begin{bmatrix} -l(x_t - x_b)/R + x_b \\ -l(y_t - y_b)/R + y_b \\ -lh/R \\ \text{atan2}(y_t - y_b, h) \\ \text{atan2}(x_t - x_b, h) \\ \text{atan2}(y_t - y_b, x_t - x_b) \end{bmatrix}. \quad (3.1)$$

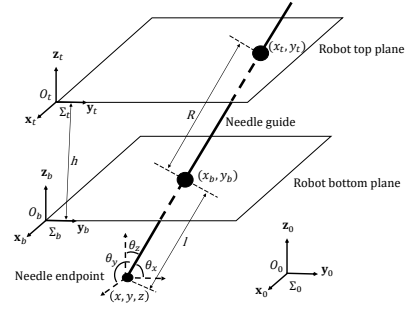


Figure 3.3: Forward kinematics diagram

ball joints. The variables $x, y,$ and z describe the position of the needle in the global fixed frame, while $\theta_x, \theta_y,$ and θ_z describe the roll, pitch and yaw angles of the needle in the global coordinate frame. From the robot morphology, it is clear that the latter 3, describing orientation of the needle, are not independent, as rotations about the needle axis cannot be controlled. All variables are shown in Figure 3.3.

From Equation 3.1, it is clear that the angular range of the robot will be determined by the travel of the upper and lower stages, as well as the distance between the two. Physical limitations constrain the minimum value for h , the height between the planes, while larger values reduce the angular positioning capability. This relationship is shown in Figure 3.4.

3.2.3 Image Jacobian

The image Jacobian is a critical component for effective control of the parallel plane robot, as visual servoing provides the important advantage of not being beholden to modeling error, as kinematics based control methods are. The image Jacobian relates small displacements of the actuators to motion of the fiducials

$$J = \frac{\partial C}{\partial M^T} \quad (3.2)$$

where C is the 4 DOF configuration of the robot fiducial markers in the image (camera) space, and M represents the 4 actuator (motor) positions in the robot space, $C = [C_{xt} \ C_{yt} \ C_{xb} \ C_{yb}]^T$, $M = [M_{xt} \ M_{yt} \ M_{xb} \ M_{yb}]^T$. Because the fiducials are rigidly mounted to the needle guide, this Jacobian matrix also relates the actuator positions to the needle

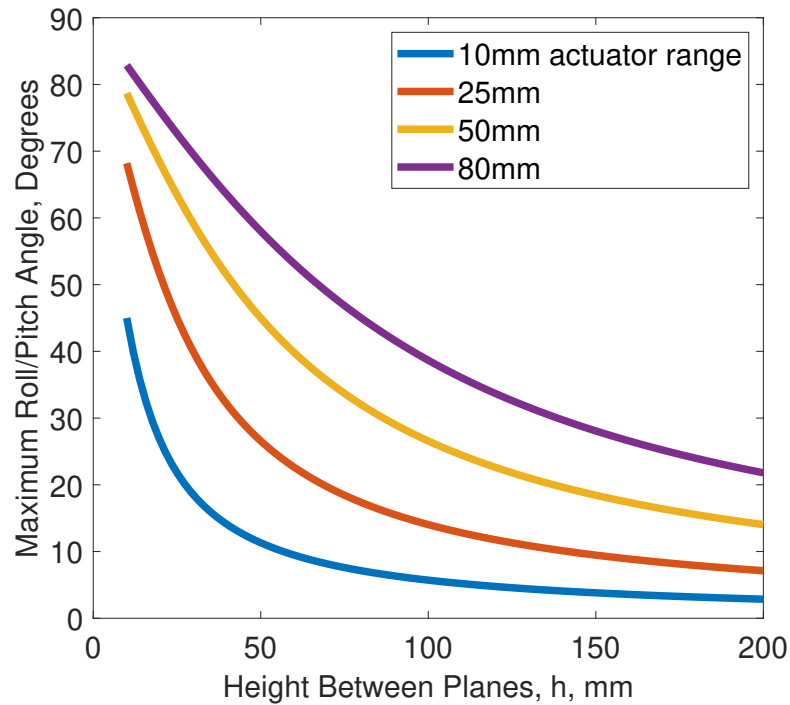


Figure 3.4: Positioning range for varied actuator travel and plane distances.

orientation. From Figure 3.5 and Equation 3.2, the mapping between the robot space and image space is contained within the image Jacobian, so the relative orientation of the two planes is immaterial to the positioning protocol. The use of the image Jacobian for control of the robot is further described in the following section.

3.2.4 Workspace analysis

The workspace of the parallel plane needle positioning robot is shown in Figure 3.6. The transparent surface is the reachable surface with any set of angles, while the solid surface is the reachable surface when the angle about the x axis, θ_x , is restricted to less than 15 degrees. The workspace shown was visualized by computing endpoint positions via the forward kinematics (Equation 3.1) for the full range of actuator positions with needle depth of up to 10 cm. Due to the height of the robot above the patient, and observed geometry of the lumbar vertebrae, this is a reasonable restriction.

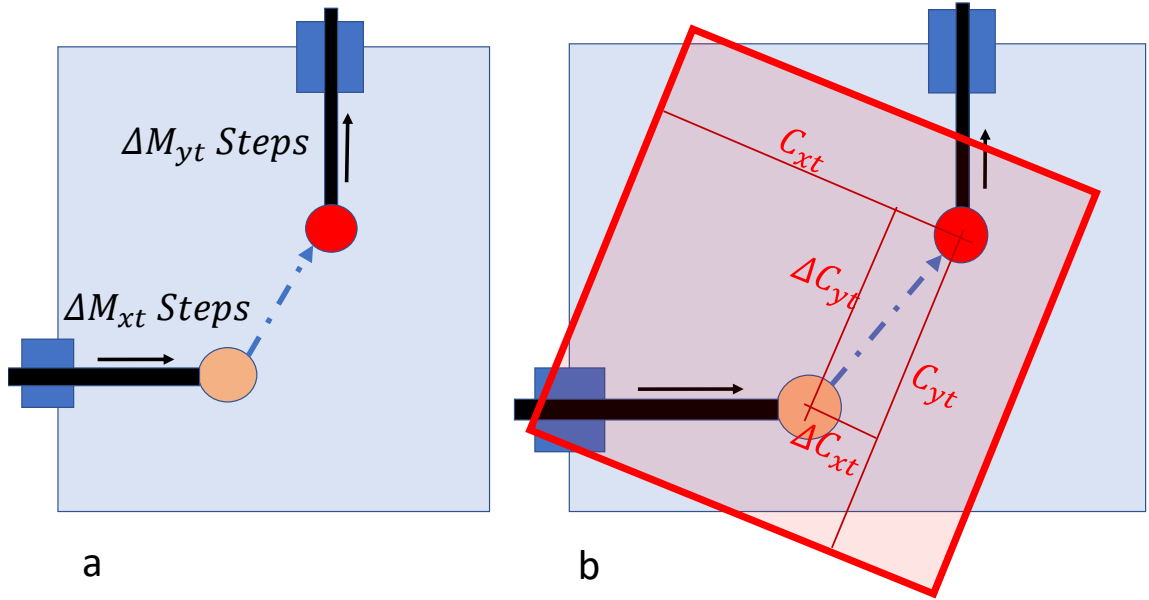


Figure 3.5: Top plane positioning variables, a) shows the robot positioning parameters, b) shows the image plane in red and positioning variables measured via image

3.2.5 Actuators

Positioning accuracy of the needle guide is the critical aspect of this robot. For this reason, direct drive linear motors were chosen to reduce backdrivability and backlash. Linear piezoelectric motors were chosen because of their MRI compatibility and high precision (PiezoLEGS 6N non-magnetic, MicroMo, Clearwater, FL).

These linear motors are uniquely suited for the desired high resolution positioning, as they have a step size of 4-7 μ m, consume no power when maintaining a fixed position, and are MRI compatible [53]. The ability to place these actuators inside the bore of the scanner allows a rigid link between drive rods and the robot frame, eliminating the need for gearing or a cable drive, and their associated backlash and deformation problems.

3.3 Control

A schematic of the visual feedback system is shown in Figure 3.1e. In this work, the visually tracked fiducials are rigidly affixed to the robot stages. Planar slices of the 3D

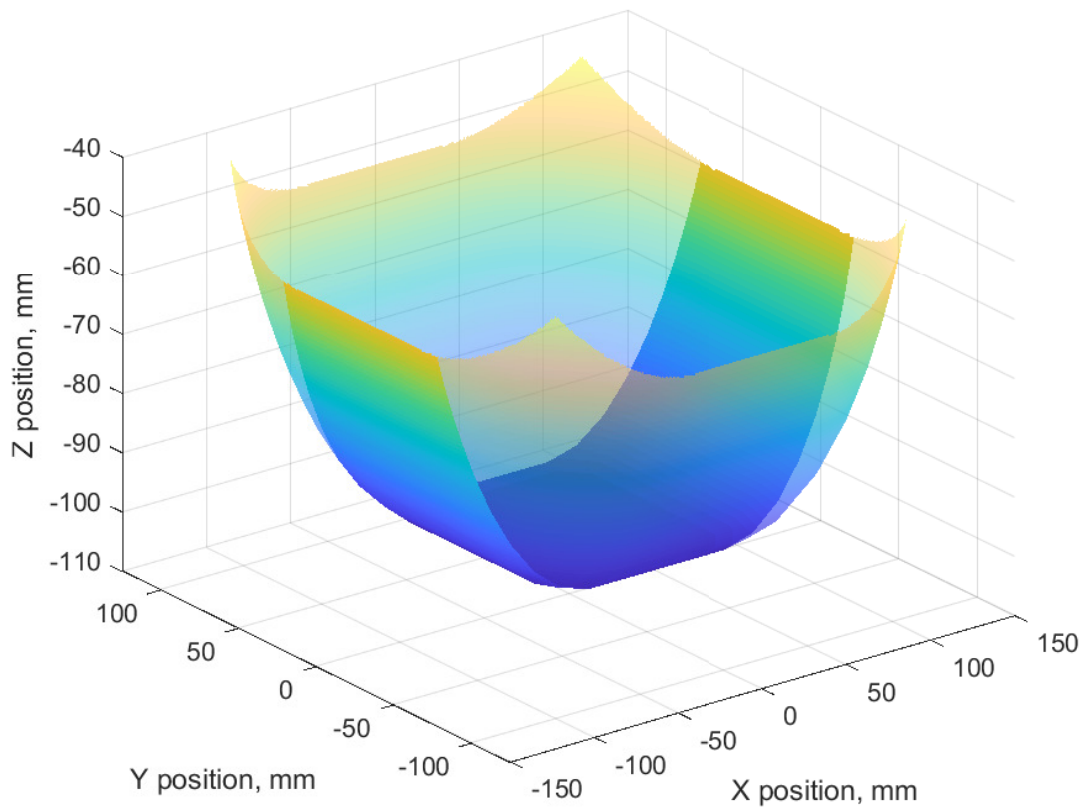


Figure 3.6: Workspace of the robot

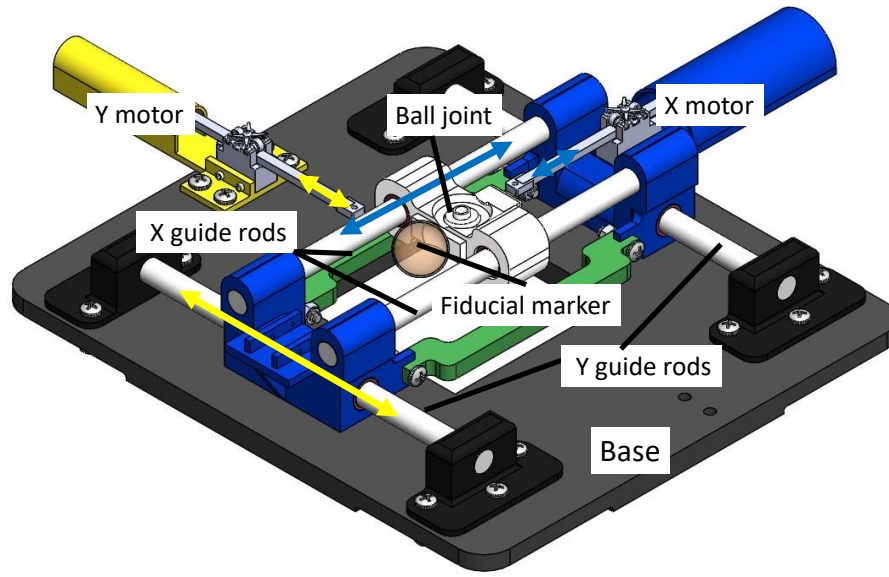


Figure 3.7: Robot stage design, x axis motion shown in blue, yaxis motion shown in yellow magnetization prepared rapid gradient echo (MP-RAGE) scan (1mm pixels, 1mm slice thickness) shown in Figure 3.29 are evaluated for the 2D pixel coordinates of the center of each of the upper and lower stage fiducials.

3.3.1 Fiducials

Critical to the the control of this robot in the MR environment is the image based feedback method. The materials used in the construction of the robot are not visible in the images, so additional fiducial landmarks must be placed on the robot in order to gain feedback about the robot's configuration within the scanner bore. The kinematics of the robot are centered around the 4 DOF position of the needle guide, with an additional DOF potentially necessary for other applications. Because of the critical nature of the needle guide orientation, a range of MRI contrasting fiducials were tested. The fiducials and their coronal slice views are shown in Figure 3.9. All of the fiducials consist of a hollow cavity which is filled with Vitamin E as a contrasting fluid and sealed. Gadolinium fiducials were also evaluated, but dilution inconsistency proved to negate the higher contrast benefits.

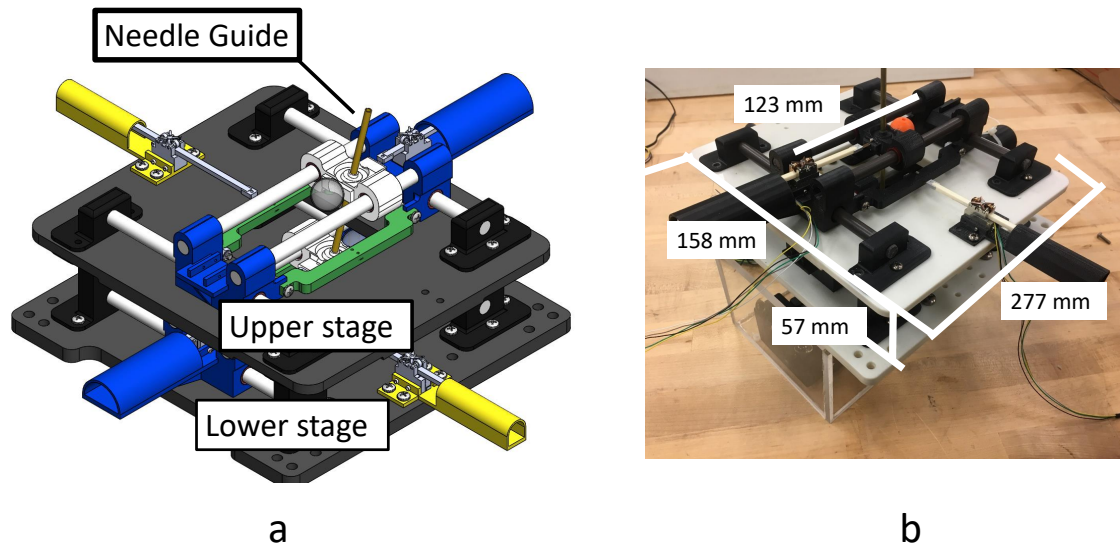


Figure 3.8: a) Full robot CAD model with upper and lower stages shown b) Robot with salient dimensions

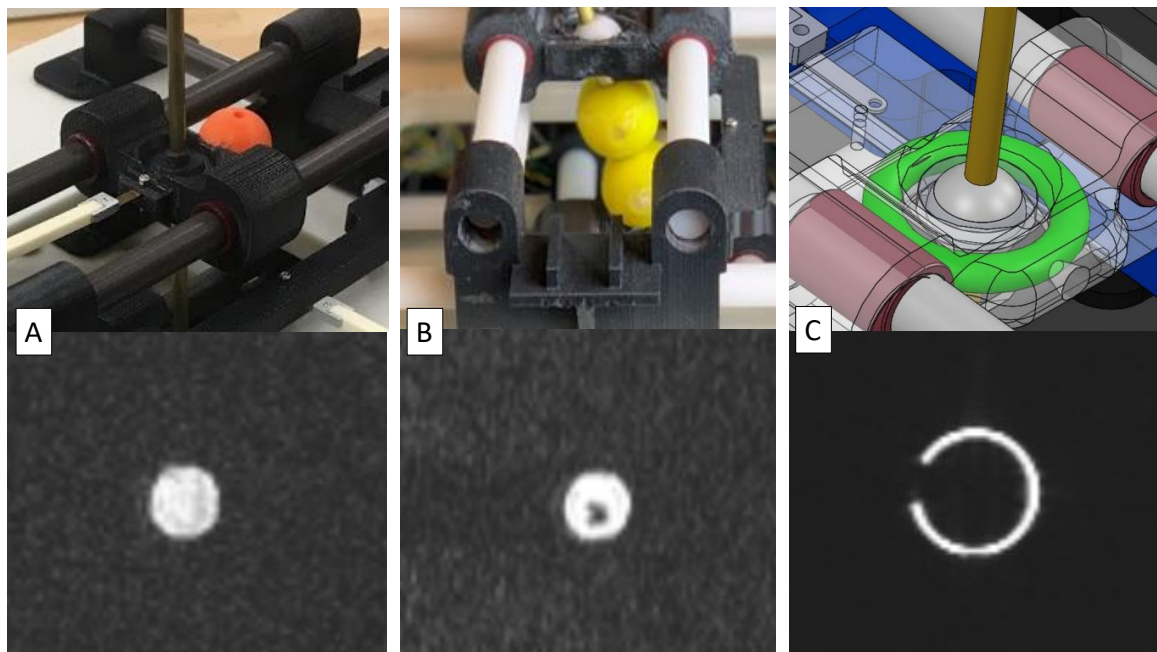


Figure 3.9: Fiducial markers used in this work, A) offset spherical fiducial, B) inline spherical fiducial, C) collar fiducial

Of the tested fiducials, the in-line fiducial performed the best. Challenges with 3D printing the collar components made the collar cavity fiducial inconsistent, and the offset

fiducial requires a different control process because the fiducial center is not co-linear with the needle trajectory.

3.3.2 Hysteresis and actuation variability

Although the visual servoing method described below is capable of effectively mitigating any shortcoming in the repeatability of actuator motions across the workspace, any variability in actuator motions would be expected to impact positioning time as well as any open-loop positioning use cases. The impacts to positioning time stem from errors in the estimate image jacobian, as a single actuator step size can vary across the workspace of the robot. Open-loop positioning is necessary for the super resolution imaging procedure detailed below, and thus actuation variability was assessed and described here.

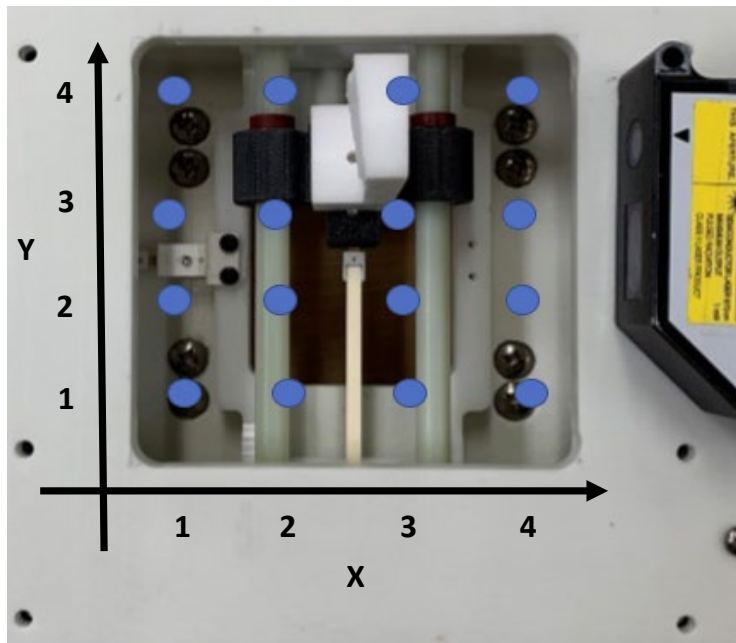


Figure 3.10: Single stage open-loop positioning performance evaluation setup

Because measurement of stage positions requires the use of a laser triangulation sensor, this assessment was only possible on a single stage of the robot. However, the construction is nearly identical, and similar results would be expected for both stages. The experimental setup for this evaluation is shown in Figure 3.10. The X and Y actuators were each stepped

forward and backward 1000 steps 10 times at each of the 16 points shown in the figure. The actuator directions are shown by the arrows along each axis. The position of the center laser target was measured after each movement. The target was rigidly mounted to a fixed version of the ball joint collar.

The results of the repeatability experiments are shown in Figure 3.11 and Figure 3.12. The Y axis actuator has a much larger step size variability than the X axis actuator, most likely due to higher frictional forces in the guide rods. There is also significant variability across the stage workspace in both actuators. These maps of repeatability could be used to determine suitable locations for jacobian estimation, as well as prediction of positioning performance for various robot configurations.



Figure 3.11: Repeatability of X actuator motions

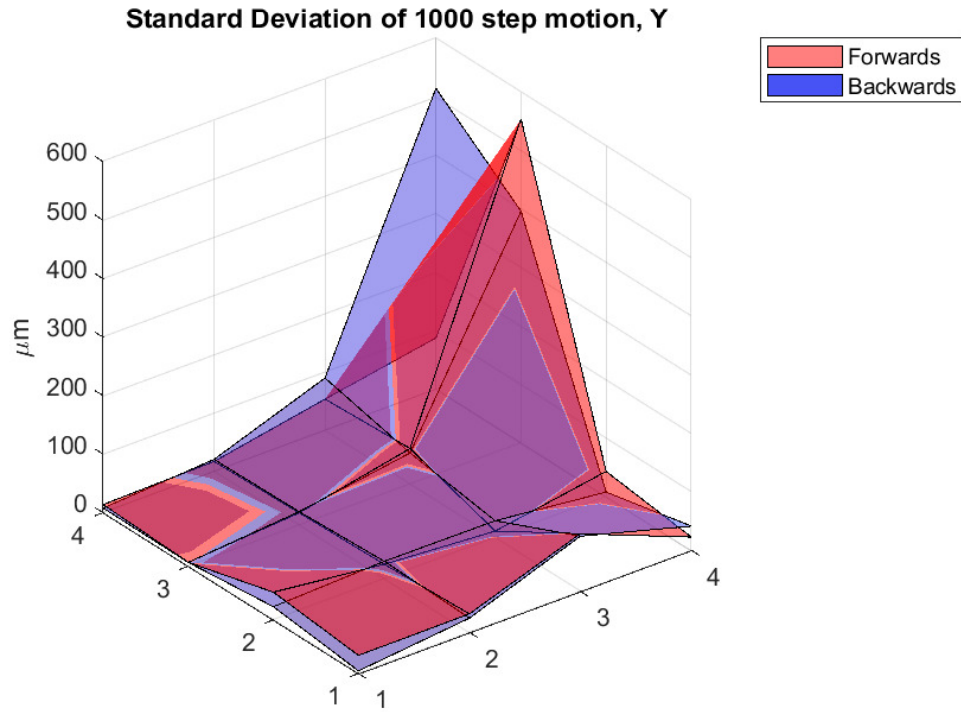


Figure 3.12: Repeatability of Y actuator motions

Additional results of the repeatability experiments are shown in Figure 3.13 and Figure 3.14. Hysteresis is a significant problem for the Jacobian based positioning described below, as the Jacobian maps changes in position to motor step counts without regard to direction. A potential solution is to estimate entries for negative error values and substitute these entries when the planar errors are negative. Although this approach has an associated cost in extra imaging time, it may reduce the number of loop iterations as well, and should be evaluated.

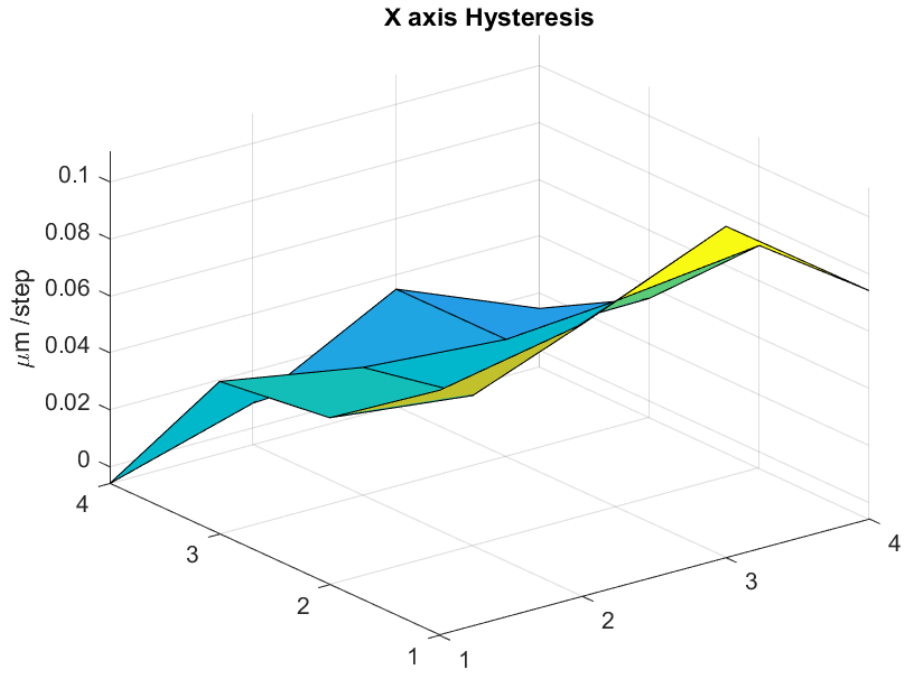


Figure 3.13: Hysteresis of X actuator motions

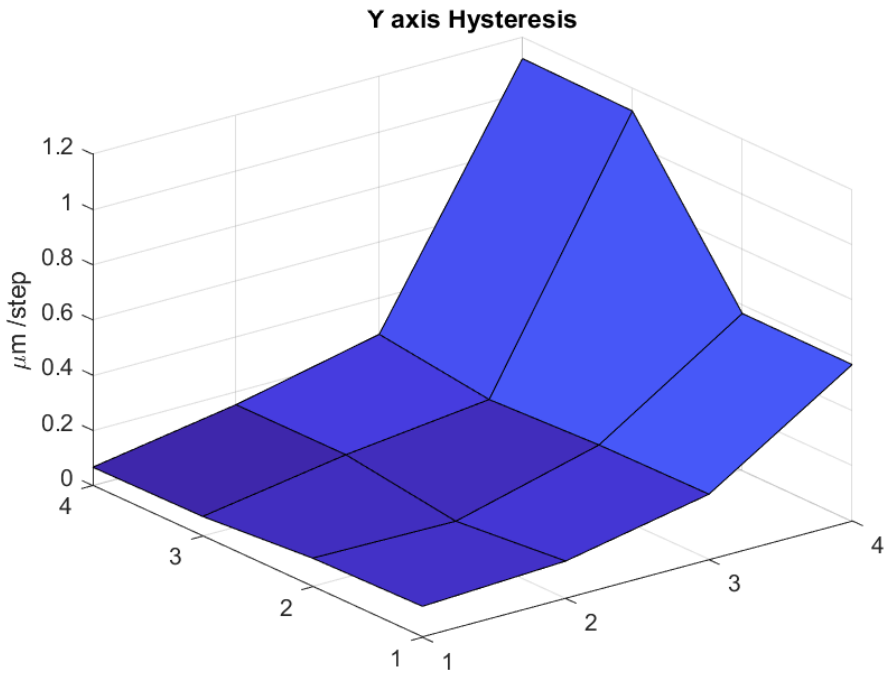


Figure 3.14: Hysteresis of Y actuator motions

A more detailed look at the hysteresis of the individual axes and configurations is shown in Figure 3.15. These curves show variability between both the individual motors and the points along the workspace of each motor. The range in hysteresis is from 22% in the Y axis at the (4,4) position to 2% in the X axis at the (4,1) location. The modeling of this hysteresis is a potential method for pre-compensation in actuator commands to reduce motion variability. One model that has been used successfully in piezoelectric actuation is a modified Prandtl–Ishlinskii model [54]. This model incorporates a vector of play operators $H_{r_H}(x, y, r_H) = \max(x - r_H, \min(x + r_H, y))$, with thresholds r_H where the displacement y is a function of motor steps x and H . A linear combination of superimposed H_{r_H} operators can be fit to experimentally determined continuous displacement-command curves in order to model hysteresis. This approach can be used to model the hysteresis in each actuator here, but practical considerations may limit its utility. Particularly, the source of hysteresis is likely the guide rods, and the forces can vary depending on robot configuration and assembly process. Because there is no direct position feedback from the actuators, measurements would have to be made in a laboratory setting before model based pre-compensation could take place in the MRI where the original sources of hysteresis may have shifted or changed. Essentially, the results shown in Figure 3.15 would be used to fit a vector of H_{r_H} values at each location in the actuator workspace, but these values may be incorrect once the robot is moved/reconfigured, and the limited resolution of MRI prevents validation in the scanner.

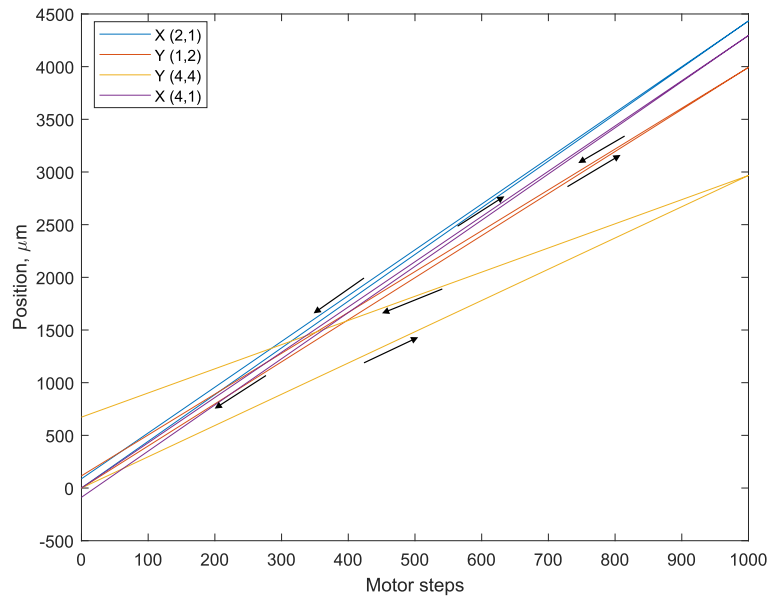


Figure 3.15: Representative hysteresis loops for 4 measurement positions

The results reported here characterize actuation variability and hysteresis for one stage of the robot. While the plots in Figure 3.11, Figure 3.12, Figure 3.13 and Figure 3.14 provide sufficient information to both assess the adequacy of prospective Jacobians and mitigate hysteresis by creating a negative error version, they likely do not always fit the robot. This is because the most likely cause of the variability is friction between the guide rods and linear bearings. The absolute positioning of the guide rods are dependent on the mounting brackets, which are moved each time the robot is assembled. Any prospective use of this characterization would require repeating the experiments detailed here, which is likely unfeasible.

3.3.3 MRI based visual servoing control

The image-based visual servoing control method implemented is listed as algorithm 1. There are two benefits to the use of this image based control method with needle guide mounted fiducials. 1) A kinematic model of the robot, and associated errors are not necessary, and 2) There is a lower requirement for hardware on the robot and in the scanner

bore.

The ability to avoid the use of a kinematic model stems from the nature of the image based control. Because the mapping between the robot's actuators and the robot's configuration is found from the images, all of the trajectory and target identification and control takes place in the scanner image space. This avoids a specific registration step in the initial setup and calibration of the robot. It also makes the positioning process more robust to shifting of the patient in the scanner bore, as any movement of the target can be captured at each step.

```
known: desired fiducial pixel coordinates, desiredFidCoords;  
initialize: jog each robot axis and note corresponding change in image pixel coordinates to  
obtain numerical approximation of image Jacobian matrix,  $J$ ; normPixelError = large  
value;  
while normPixelError > 1 do  
    Take MRI Image;  
    pixelErrorVector = actualFidCoords – desiredFidCoords;  
    normPixelError = ||pixelErrorVector||;  
    Update Actuators by  $-J^{-1}$ pixelErrorVector;  
end
```

Algorithm 1: Imaged-based visual servoing control

3.3.4 4 Axis repeatability

The repeatability of the robot was measured with a laser triangulation sensor (optoNCDT ILD2200-20, resolution: 0.3 μ m, Micro Epsilon, Germany). Although all 4 DOF were actuated, measurement took place at the needle endpoint along a single axis. All 4 actuators were stepped forwards and back 500 steps (\sim 2.5mm) in each of 5 robot configurations, Actuator stepping was done 10 times for each of the 5 configurations. The mean standard deviation of these motions was 36 μ m, with a range from 19-51 μ m for each of the 5 configurations shown in Figure 3.17. This shows that the open loop repeatability (3σ) of the robot is less than a sixth of the 1mm resolution of the MRI scanner.

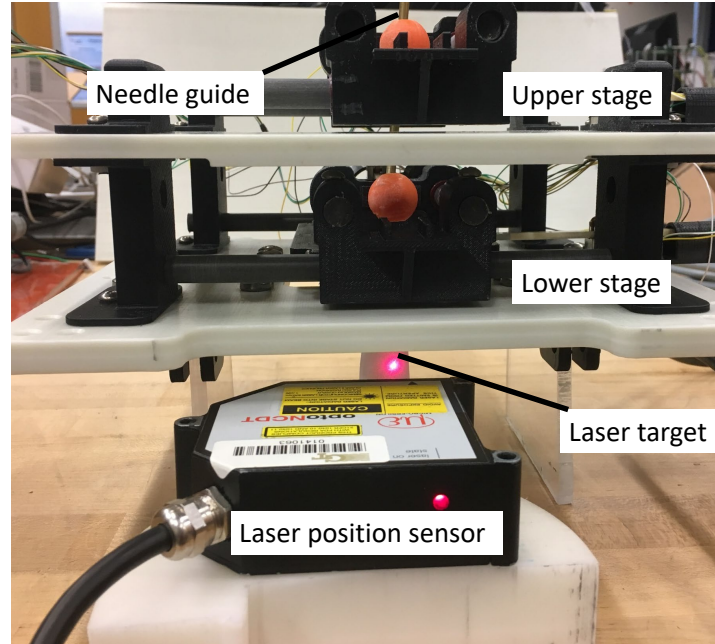


Figure 3.16: Laser position sensor experimental setup

3.3.5 Camera based positioning

The results presented above demonstrated that the robot is capable of positioning repeatability at least 6 times better than the capabilities of the MRI scanner. In order to better capture the positioning capabilities of the robot, camera based visual servoing was applied. A camera placed above the upper stage of the robot (Intel Realsense D435 RGB-D camera) captured the planar position of the upper stage fiducial, the lower stage could not be measured in all configurations, because of visual occlusion. For this reason, the position of the lower stage was fixed in the center of the workspace for the duration of the camera based experiments. The resolution of the camera was $105\mu\text{m}$ for the top fiducial. The visual servoing method presented in subsection 3.3.3 was then applied to move the upper fiducial from each of the 4 outer configurations shown in Figure 3.17 to the central (vertical) configuration, and from the central configuration to each of the outer ones. Aggregate results from these 8 trials are shown in Figure 3.18a. After 9 iterations, the fiducial reached the target position, corresponding to a maximum position error of $74\mu\text{m}$ (the diagonal of a pixel). This error is a significant improvement upon the previously developed spinal in-

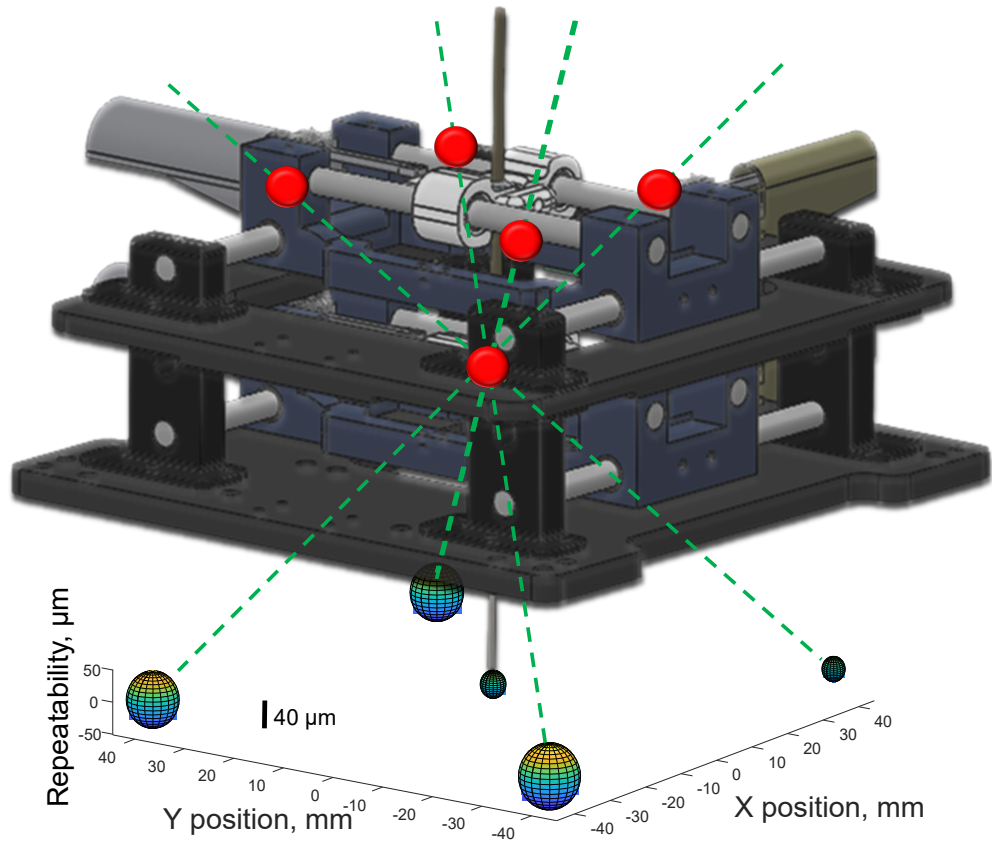


Figure 3.17: Repeatability results, red dots and green lines represent the 5 evaluated robot configurations, the plotted spheres have radii equivalent to the mean standard deviation for each of the configurations

jection robot [39]. Because the upper and lower stages are both identical in construction and not rigidly coupled, maximum errors should be the same in both stages when imaging feedback is applied equally, i.e., in the MRI scanner where visual occlusion is not present.

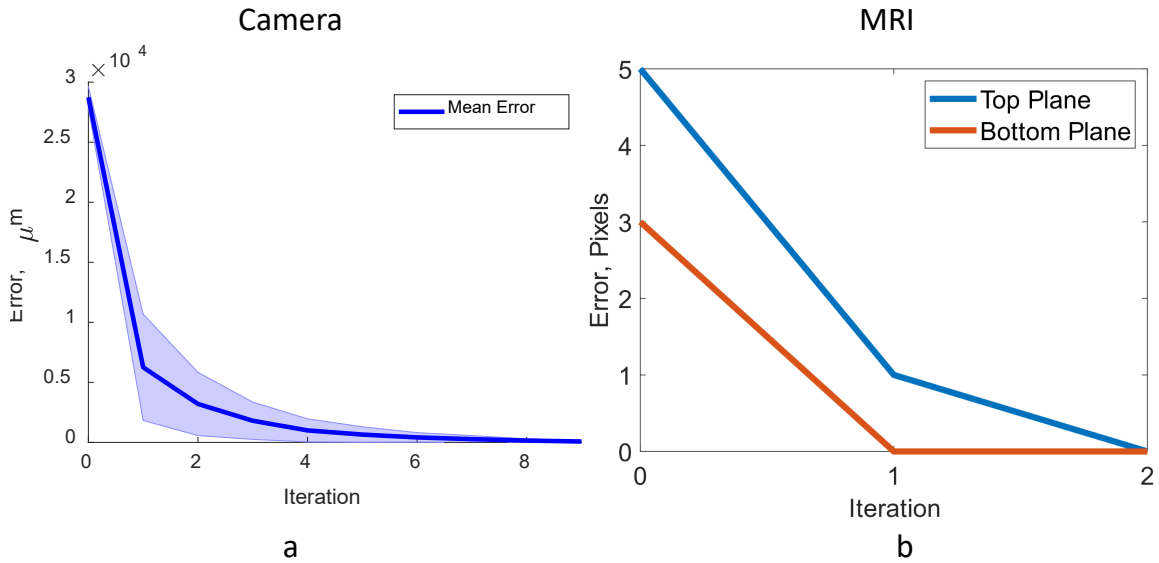


Figure 3.18: Positioning results for a) Camera based servoing and b) MRI guided servoing

3.3.6 MRI positioning feedback experiments

A validation of the entire system was performed in a 3 Tesla MRI. The same visual servoing method was applied as in the above experiments, but in this case, both the upper and lower stages were actuated. The target position was set manually, prior to the beginning of imaging, and chosen so that a stainless steel rod inserted in the guide tube would pass between the vertebrae and into the phantom spinal cord. A total of 6 images were taken, with an initial image to get the target positions, 2 to compute image Jacobians, and 2 more to move both stages back to the target position. A representative image is shown in Figure 3.29.

Positioning results from the last 3 images are shown in Figure 3.18b, with both the upper and lower stages reaching the target pixel after 2 updates. Targeting was confirmed by inserting the rod into the needle guide, and verifying that there was no contact with

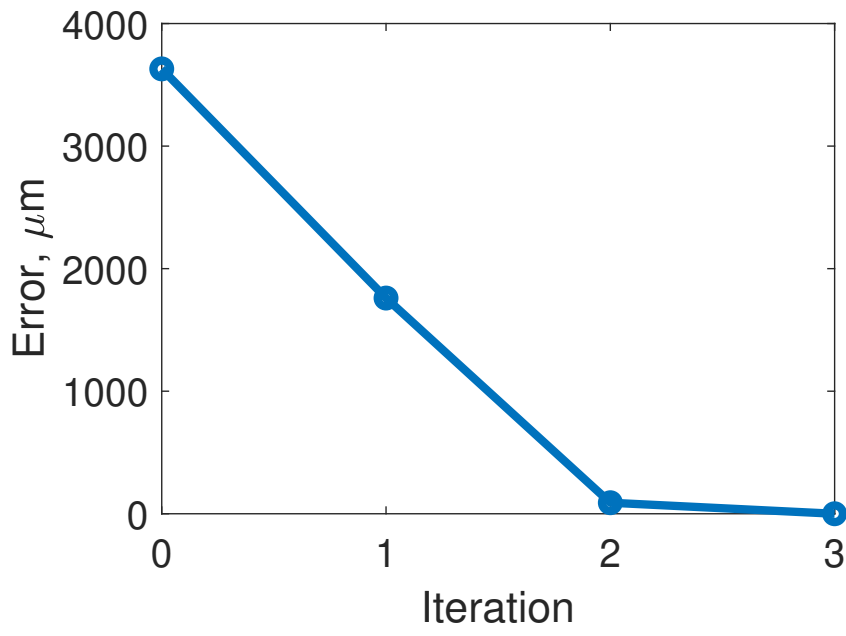


Figure 3.19: Positioning results with laser position feedback

the phantom vertebrae. In this case, the absolute maximum error is 0.7mm, or half the diagonal of a 1mm pixel.

3.3.7 Accuracy discussion

The robot accuracy was measured in two different experiments with two different image feedback methods. The MRI positioning experiments demonstrate that the system works as expected in the MRI environment. Only 2 position updates are required to reach a target pixel with both the upper and lower stages, indicating that the visual feedback system converges to a target within MRI resolution in a suitable time. Camera based positioning experiments showed that if the imaging feedback is provided at a higher resolution, the robot is capable of higher accuracy than the MRI, with 9 updates producing positioning with a maximum error of only 74 μm . In this case, accuracy of the robot is limited by imaging feedback, because the target pixel was reached in all 8 of the trials.

The most accurate measurements of the robot's repeatability were performed with the laser triangulation sensor. In this case, the needle guide position was measured directly,

instead of the upper and lower stages. This measurement then takes into account possible errors in positioning due to relative displacement of the needle guide and fiducials during movement. The repeatability tests showed that even with open loop operation of the actuators, the positioning repeatability is quite good, with a maximum standard deviation of only $51\mu\text{m}$, about $1/20$ of the pixel size produced by the MRI. The ability of the robot to repeatably produce positions with higher accuracy than a single MRI pixel motivates the future development of image reconstruction methods to provide super-resolution positioning in the scanner environment to surpass the current limitations created by the MRI scanner resolution.

Although the best available image feedback system, the RGB camera, had a resolution of $105\mu\text{m}$, the laser repeatability measurements indicated that higher accuracy positioning is likely possible. For this reason, the laser position sensor used to measure positioning repeatability was applied in a simple linear feedback positioning task. The robot was set in the vertical configuration at the center of the workspace, with the laser position sensor measuring the needle endpoint. A single actuator was then moved to an arbitrary position, ensuring that the endpoint stayed within the range of the laser sensor. From there, a basic linear feedback method was applied, with the results shown in Figure 3.19. The limitation again appears to be the resolution of the laser sensor (measurement resolution $9.4\mu\text{m}$), and not the accuracy of the feedback method or robot itself.

3.4 Target selection interface and system design

Selection of target trajectories is a challenging part of the injection procedure. In particular the small size of the target and complex occlusion by the vertebrae makes the selection of target orientation a challenging task. This task is normally performed via a combination of 2 dimensional views and 3 dimensional projections, as shown in Figure 3.20. A picture of the imaging interface is shown in Appendix B.

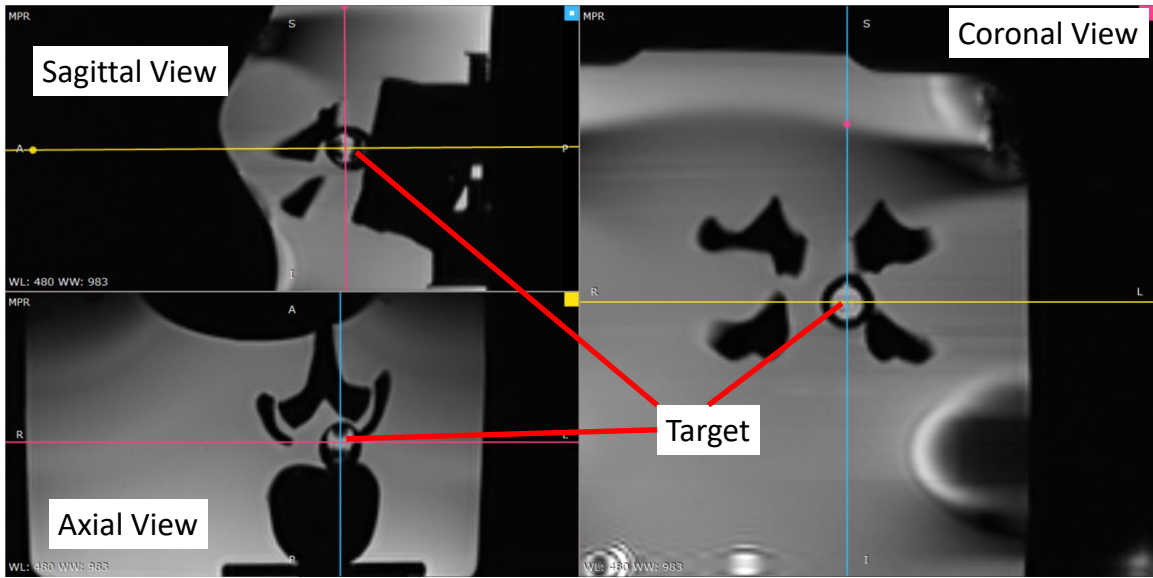


Figure 3.20: 2D planned needle trajectory with target, and current and target needle trajectories shown

3.4.1 Clinical preferences

The development of this robot and the associated control methods focused on the use of straight tools, both needles and cannulas for injections, as well as straight RFA probes. For targeting of the ventral horn of the spinal cord, the geometry of the obstruction means that little benefit is gained from non-straight (fixed or steerable) needles. Because any needle must pass between the lamina and through the associated ligaments and dura, a nearly straight trajectory is required. Clinical collaborators expressed reticence to apply non-straight tools to intraspinal injection, as all prior instances of this procedure, both open and minimally invasive utilized straight needles [34, 6]. Non-straight and steerable needles may have application to other prospective uses of the robot, as described in section 3.7.

3.4.2 Surgical freedom simulation

Instead of the cadaver experiments commonly used to evaluate surgical freedom, this work employed a simulation environment. A mesh model of the 3rd lumbar vertebrae was gen-

erated, and used as the basis for surgical freedom estimation. The model used was from an open source medical image database [51]. All potential (straight line) trajectories to reach a set target without obstruction by the vertebrae that fit within a 60 degree insertion angle were evaluated numerically. Surgical freedom was then estimated as the relative number of viable trajectories to reach the target. This was measured as a percentage of the available trajectories fitting within the region formed by a 60 degree insertion angle above the vertebrae (targeting the ventral horn from below the patient is not feasible). The simulation of trajectories was done via the COMSOL ray optics module.

Results from the surgical freedom simulations are shown in Figure 3.21 and Figure 3.22. 55940 of the 101500 tested trajectories resulted in a usable needle path, for a surgical freedom of 55.1% in the relevant angular restrictions. Each of the rays in Figure 3.21 represent a potential trajectory to reach the chosen target in the ventral horn, with the rays stopping at the vertebrae occluded. In Figure 3.22 the viable trajectories are represented by the blue dots, with the robot positioned above the vertebrae and an example needle path to the target shown in green. These results provide a useful guide for the user of the VR interface described in subsection 3.4.3, because the simulation provides an estimate for the regions where target trajectories will be found. The complexity and requirements of the geometric restrictions to the potential trajectories can be increased to account for sensitive soft tissues or other important anatomical features to avoid; however, this work only considered the immediate vertebral obstacle. For a more accurate estimation of the true relative surgical freedom, a more complex CAD model of the spine is necessary, however the basic computational steps are identical to those outlined above.

Future work will seek to more tightly integrate the surgical freedom estimation and robot control scheme. However, computation time limits the ability to make such estimations from the MR images directly. From the results presented, clinicians are given a starting point to reference before exploring patient specific trajectories in the VR environment.

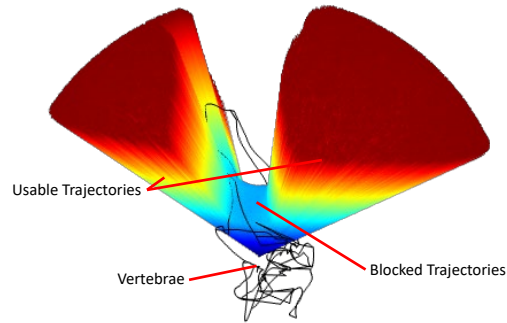


Figure 3.21: Surgical freedom simulation results with all potential trajectories shown

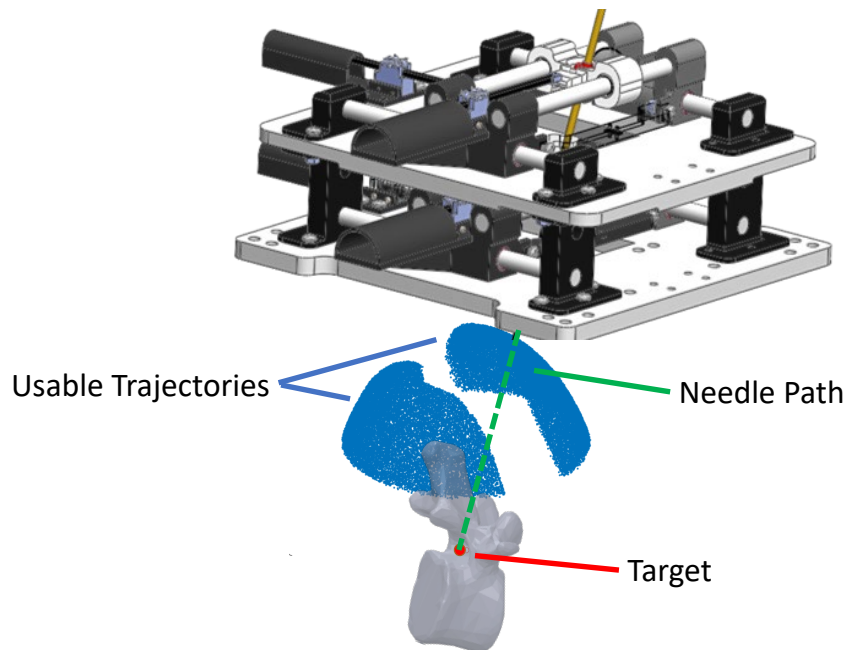


Figure 3.22: Surgical freedom simulation results with robot and vertebrae model, an example needle path is shown in green

3.4.3 VR environment for target selection

Although it is possible for experienced clinicians to select suitable trajectories in this manner, it is onerous, and must take place while the subject and robot are in the scanner, taking up a significant amount of the overall procedure time. For this reason, a virtual reality interface was developed to aid in visualization of the scan data, robot configuration identification and target trajectory selection. The system developed is shown in Figure 3.23.

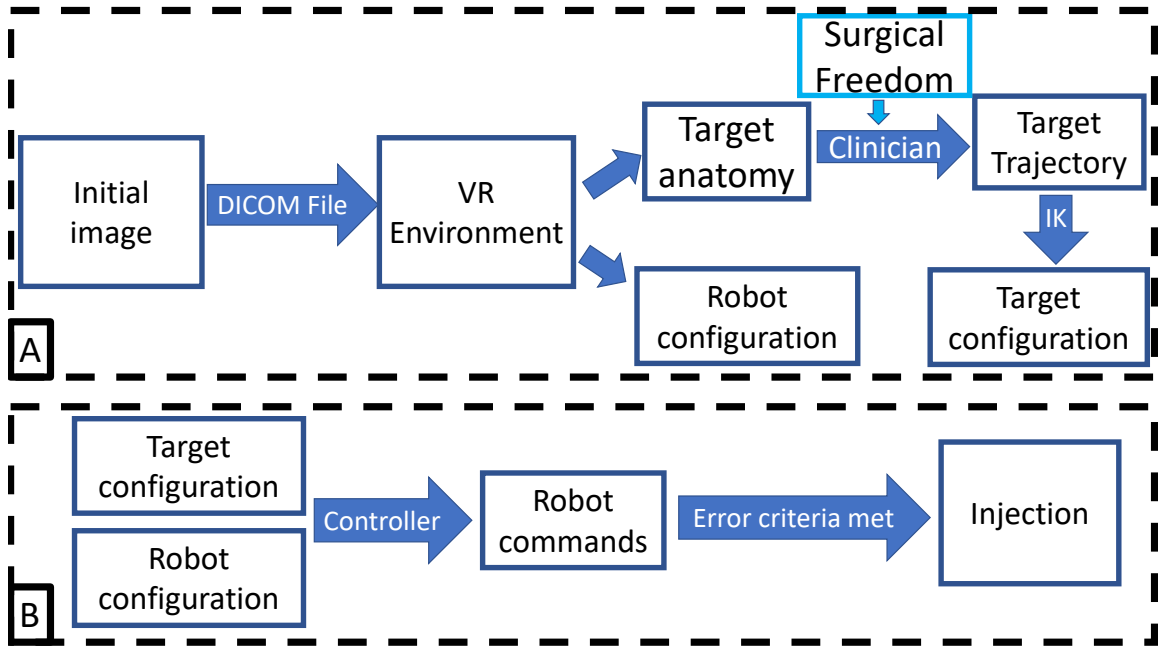


Figure 3.23: The VR guided system reported in this work, A) The image guidance system and B), the robot actuation scheme

Various MRI rendering solutions have been developed, many tailored to a particular area of interest. There is less work focusing on VR due to its emerging nature, however, there have still been some experiments [55, 56] that were of a similar nature to this work. In short, the data is combined into a 3D volume, which can then be rendered using various methods of volume rendering to merge points into a surface. Depending on the volume of interest and the data required, many techniques can be used. In this work, the DICOM file is parsed into a three dimensional image, which is then rendered via ray tracing, with optimizations that cause minimal effects to the rendered image. This procedure is performed twice, once per eye, to give the user the perception of depth, making VR more advantageous than traditional methods. There are other programs using similar techniques [56]; however, they were found to be incompatible with the robot configuration and kinematic calculations necessary for this project. Once the rendering solution is established, an additional critical component is the material segmentation. There have been many works relating to segmentation within MRI scans [57, 58], with varying degrees of complexity. VR provides

a unique ability for users to be able to intuitively perceive the depth within the MRI scan, as well as freely manipulate the model in six degrees of freedom . This greatly improves the speed of the targeting process when compared to traditional computer monitor based solutions.

Two main problems were present in earlier target trajectory generation experiments with the robots: 1) Estimation of the fiducial locations from the relatively coarse image slice separation and 2) determination of suitable trajectories to avoid obstacles in the anatomy. The implementation of a VR system into the image workflow aids in addressing both of these issues. Images are taken from the scan server as DICOM files, then fiducial locations and the target geometry are automatically assessed and displayed in a VR environment. This key automation step allows rapid and accurate assessment of the robot's current configuration, likely decreasing the number of iterative position updates needed to reach a given target.

The main benefit of performing the image guidance in the VR environment is the ease of visualization. The anatomy around the proposed target injection site, the spine, is both complicated and sensitive to disturbance. It is critical that clinicians are able to clearly and confidently visualize both the target and the robot. Traditional planar projections can allow for detailed inspection of specific anatomical features, but require significant spatial reasoning skill to accurately and reliably interpret and determine needle paths between the vertebrae and into a spinal target. Prior work has found that the performance of clinical radiologists is correlated with spatial reasoning ability [59] for this reason. The VR environment enables clinicians to better understand the anatomy and pick trajectories with confidence.

The VR system developed as part of this work is integrated into the existing MRI guided robotic device workflow. After an initial image is taken in the scanner, the image (in DICOM format) is then loaded into the VR interface (Unity 3D, Oculus Quest device). Immediately after loading, the image is rendered and the user can begin to interact with the

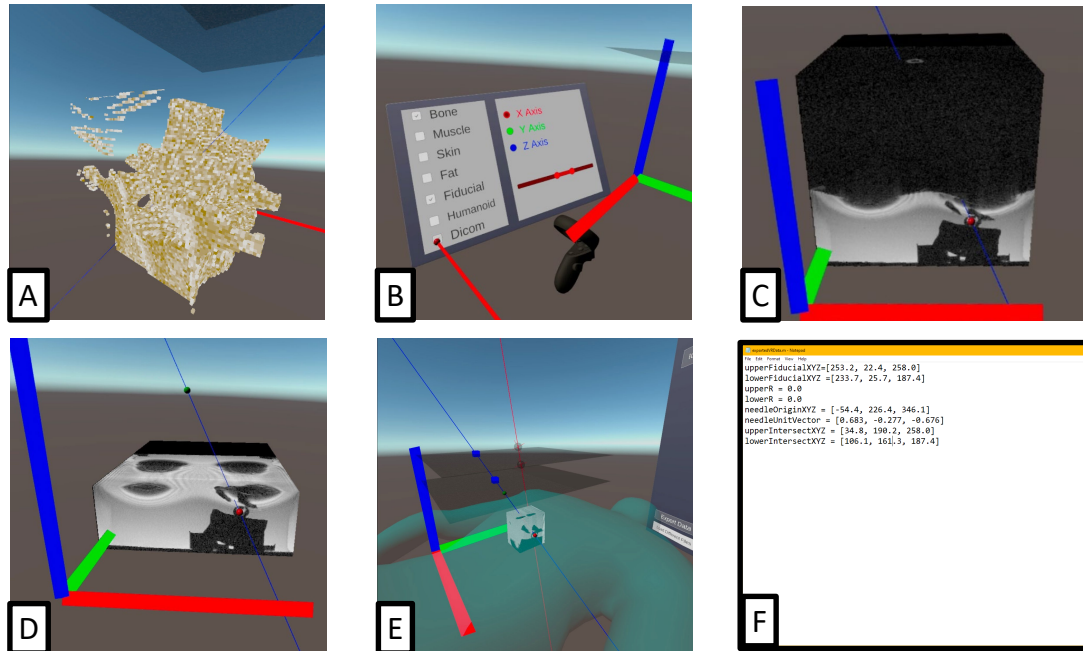


Figure 3.24: VR Image processing and procedural steps, A) DICOM data sampled for bone material, B) Material choice and reference frame selection interface, C) Full DICOM image of a gelatin phantom, D) Selected trajectory to the target D) Detected robot configuration, plane heights and target configuration, E) Program output to controller, current and targeted robot fiducial locations each in Cartesian form

image. For this project, each material type is given an adjustable minimum and maximum intensity, roughly mirroring the Hounsfield units (HU) of a CT scan. The render then uses these thresholds and the materials selected by the user to determine which sections of the volume are rendered. Secondly, a linear coloration transfer function is used to approximately color code each material type based on the aforementioned threshold values. Additionally, to aid in the viewing process, the user is able to ‘crop’ the volume via a set of sliders which controls the minimum and maximum viewable ranges of the x, y, and z coordinate axis. This can be used to easily view into the inside of a solid volume or a noisy scan where the thresholds are insufficient.

Finally, a ‘DICOM mode’ can be enabled which removes any material segmentation and coloration displaying the DICOM model in the typical greyscale of MRI scans. This mode used in tandem with the coordinate axis clipping can allow one to easily grasp the model and provide a 1:1 mapping with the traditional images the user may be more attuned

to.

The VR image workflow is shown in Figure 3.24. In the VR environment, the virtual vectors can be manipulated to reach a viable direction of the needle using controllers' grabbing functionality. Two moveable spheres are used to control the target needle direction as shown in Figure 3.24D. The red sphere represents the origin of the vector that should be placed to coincide with the target in the DICOM images. The green sphere will then be adjusted to decide the direction of the vector. A blue line will move along with the two spheres representing the desired needle direction. In addition, there will be two transparent spheres in the VR environment representing two fiducial spheres, and a greyscale plane is attached to each of the fiducials as shown in Figure 3.24E.

These spheres are automatically placed at the detected fiducial locations. Sphere detection uses a Hough transform to detect circles in three orthogonal planes. Since the fiducial's radius is known, the program will only detect a specific radius of a specific range (5-8cm) to increase efficiency. Once circles are detected in all 3 planes at the same location in a 3D model, the program will recognize this point as the fiducial center point. From the height of these centers, the robot planes are found. The positions of these spheres can also be adjusted freely by using the controllers' grabbing functionality. The blue cubes represent the target fiducial locations, which are the intersection points of the needle vector and the two planes. This representation also gives a clear view of the differences between the desired needle direction and the robot's fiducial spheres. Once the model has been manipulated to the desire of the user, the intersection points from Figure 3.24E are output as a set of vectors, shown in Figure 3.24F.

A phantom was developed consisting of 10% gelatin and an ABS plastic vertebrae. The phantom is shown in Figure 3.25 and Figure 3.26. The vertebrae model was 3D printed from a modified version of the third and fourth lumbar vertebrae [51]. A spherical cavity filled with vitamin E was placed in the location of the ventral horn of the spinal cord, creating a MR contrasting target. The phantom was developed only for evaluation of the

VR system, its mechanical and MR properties don't correspond to actual human tissue properties.

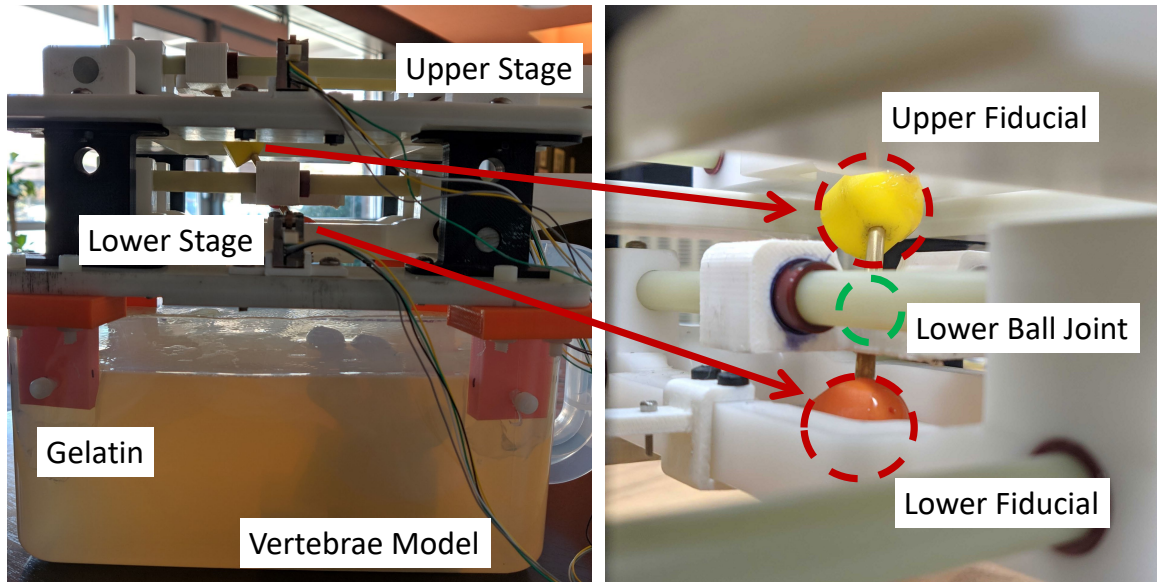


Figure 3.25: MRI phantom and contrasting fiducials mounted to the needle guide below each joint

To demonstrate the functionality of the developed system, an imaging experiment was carried out with the spine phantom and robot in a 3T MRI scanner (Siemens Prisma). The robot was rigidly mounted above the gelatin phantom as shown in Figure 3.25. A series of images was taken with the field of view set such that both the fiducial markers and phantom target were visible in the image field. The goal of the experiments was to follow the workflow in Figure 3.23A, with the captured images, needle path trajectories were to be selected using both the new VR system and a standard planar interface.

A planned trajectory from the VR environment is shown in Figure 3.27. The target in the phantom and blue line defining the desired trajectory were planned by a user. The gray planes and spheres represent the current robot configuration, with the blue squares showing the calculated target fiducial locations. This trajectory was found by exploring the VR environment and manipulating the target markers until the trajectory is not occluded by the

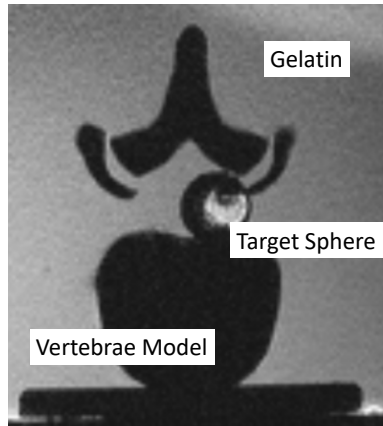


Figure 3.26: Axial MRI view of the phantom

vertebral bones. The user is able to interact directly with the images in an immersive environment, visualizing prospective trajectories as they are manually selected. The automated detection of robot configuration provides an immediate and intuitive visual cue for the user to mark the current robot trajectory, helping to increase spatial awareness.

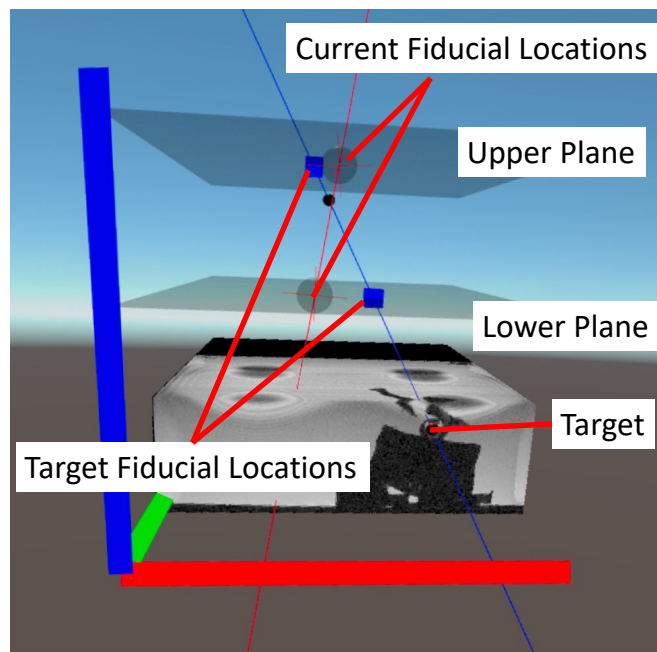


Figure 3.27: VR planned needle trajectory with target, and current and target needle trajectories shown

3.5 MRI imaging considerations

3.5.1 MRI image quality

The robot was assessed in a 3 Tesla MRI (Prisma-Fit, Siemens Healthcare, Erlangen Germany). Image quality was measured as the SNR reduction in a nickel sulfate solution cylindrical phantom. Three dimensional scans were performed under 2 different operating conditions, the first with only the phantom and RF coil (Body 18, Siemens Healthcare) in the scanner bore, and the second with the robot placed above the phantom. The imaging sequence used was the MPRAGE sequence, and scan parameters were identical throughout.

SNR was measured as the mean intensity in a 16cm^2 circular region in the center of the phantom, divided by the standard deviation of an identical region in air. The calculated SNRs were 244.06 for the control image with no robot, and 230.226 for the robot. This gives a SNR reduction of 5.7% for the robot, well within the 10% reduction criteria for MRI compatibility [41]. It is likely that shielding of the actuator cables would additionally mitigate the SNR reduction observed. The SNR was not measured during actual movement of the robot, as the information from each successive image is necessary to update the robot position, and thus the positioning protocol does not require simultaneous actuation and imaging. No movement of the robot due to induced electromagnetic forces was observed, and heating of the conducting elements was not observed.

3.5.2 Image and positioning time

Imaging time is the most significant contributor to overall procedure time, with each image taking 6.25 minutes to acquire. Robot actuation is comparatively short, 6s and 4s respectively for the updates shown in Figure 3.18b. This is comparable with a previously developed, but less accurate, spinal injection robot [39], and much faster than manual positioning methods and open surgery.

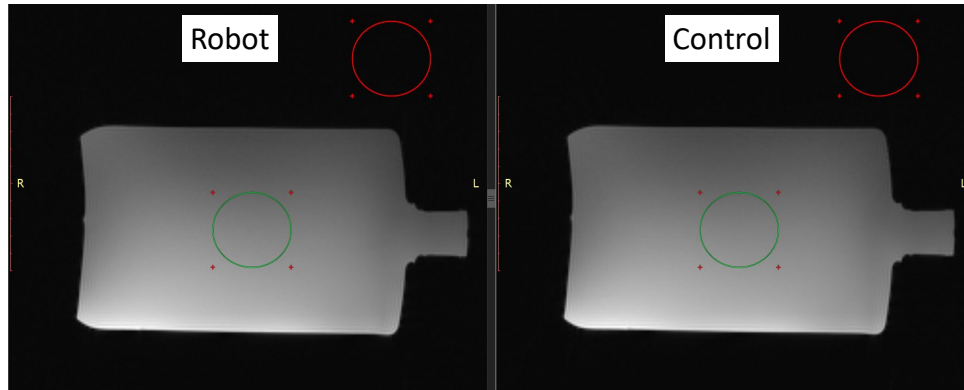


Figure 3.28: Images of the cylindrical phantom with and without the robot, regions used in the calculation of SNR are shown, with the signal intensity taken from the green circles and noise taken from red circles.

3.6 Super resolution positioning

Although the MRI sequence used during the injection procedure provides up to 1.0mm accuracy, the design of a robot with a significantly higher accuracy will allow super resolution (SR) injection. One SR algorithm that has found success across a number of imaging domains is iterative back propagation [47]. Previously reported SR MRI methods demonstrated promising results by inducing sub-pixel shifts in the scanner FOV then combining multiple images to produce a higher resolution reconstruction [48, 49]. However, the mechanics of most MRI protocols preclude the effective use of this type of sub-pixel FOV shift method along certain axes of the image [50]. In contrast, a robot capable of producing 3 dimensional spatial shifts with precision beyond the accuracy of the scanner will enable application of these methods along any image axis. Improved resolution of robot position through super-resolution reconstruction will enable injection repeatability beyond the scanner's imaging limits. Thus, the robot design process undertaken here aims to produce a system capable of accuracy an order of magnitude greater than that of the MRI. Preliminary experiments done in both benchtop and MRI environments produced promising results

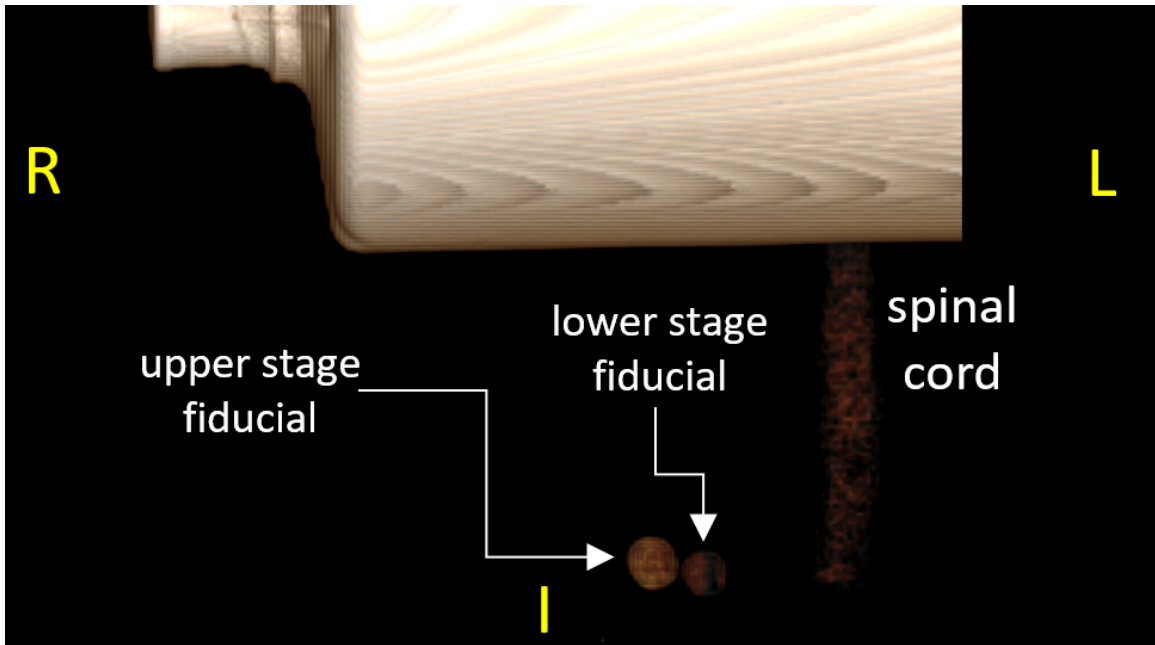


Figure 3.29: MRI view of stage fiducials and silicone spinal cord phantom, The vantage point shown is the one used for image-based visual servoing control.

showing improvement in positioning accuracy when SR positioning methods are used [60].

The robot is capable of sub-pixel movements because of the high precision actuators and direct drive design. Forward kinematics computes resultant small displacements in the fiducial markers. Note that this operation must be performed in an open-loop fashion as sub-pixel movements are essentially not visible in MRI. An arbitrary trajectory may be used to acquire a set of raw images as long as the displacements are known.

3.6.1 Super resolution offset matrix generation

To determine the spatial shifts for image reconstruction, coordinate points are generated randomly ranging from -1 to 1 pixels. The first point is where the first image is taken and is considered the origin point for the following coordinates. The movement in steps required to reach each of the random points is calculated by subtracting each point from the previous point and multiplying the difference by the inverse of the image Jacobian. The generated shifts will be stored in the offset matrix M_k for each of N images ($k = 1 \cdots N$).

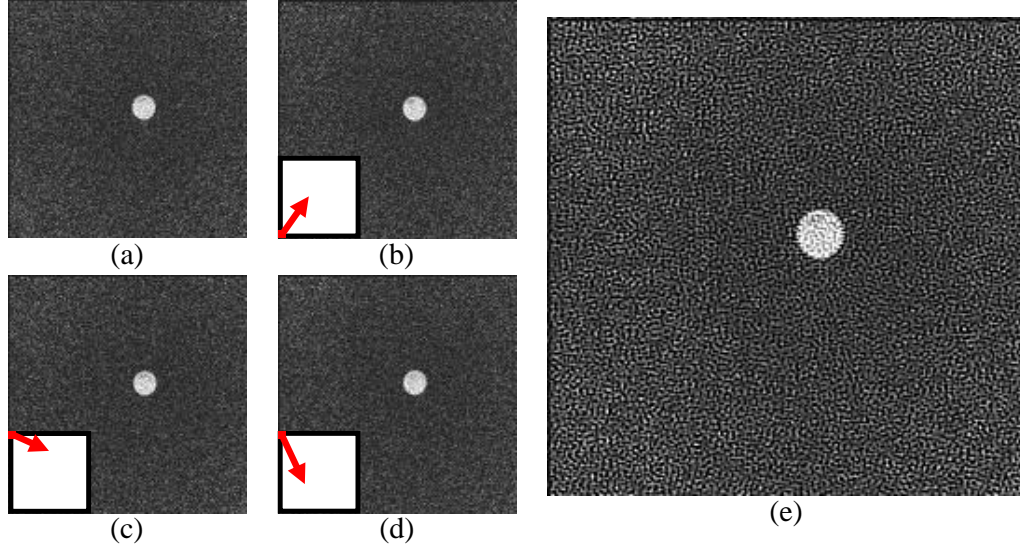


Figure 3.30: MRI SR reconstruction, a) first image with no spatial shift, b-d) three spatially shifted images with arrow representing magnitude and direction of spatial shift relative to first image. box represents 1 pixel e) SR reconstruction.

3.6.2 Super resolution image construction

The SR image is reconstructed using gradient descent optimization to minimize the error between the base resolution images, I_k ($k = 1 \dots N$), and the current best guess of the high resolution image to iteratively update the best guess of the high resolution image: $\hat{X} = \underset{X}{\operatorname{argmin}} \left(\sum_{k=1}^N \|D_k B_k M_k X - I_k\|_2^2 \right)$ where B_k is the blur matrix and D_k is the down-sampling matrix. This reconstruction was performed by an example code based on the IBP algorithm [61]. Stopping criteria is 100 iterations or when mean square error is below 0.01% of the mean square error before optimization.

For the experimental validation presented in later sections, four images ($N = 4$) were collected to double the resolution of the original images. Figure 3.30 shows the four images acquired with a vector arrow representing the spatial shift applied in each image with respect to the first image. After the 4th image is taken, the robot is returned to the first point and the SR image is reconstructed.

To measure the positioning precision with more fidelity than the images, a sharpened rod was pushed through the cannula to puncture a target mounted below the robot. A

Table 3.1: Workflow of benchtop and MRI experiments

Step	Description
1	Take image of robot in central position
2	Move robot and take images to calculate Image Jacobian
3	Create puncture and take image(s) at target position
4	Move robot to random point and take image(s)
5	Calculate error between current and target position
6	Move robot calculated error and take image(s)
7	Repeat steps 5 - 6 until error is less than 1, then create puncture
8	Repeat Steps 4 - 7 for desired number of punctures

flat sheet of paper clamped between an acetal resin plate and an ABS plate was used as the target so the punctures would be visible and the distance between punctures could be measured. The robot was attached rigidly on top of the target, as seen in Figure 3.31c.

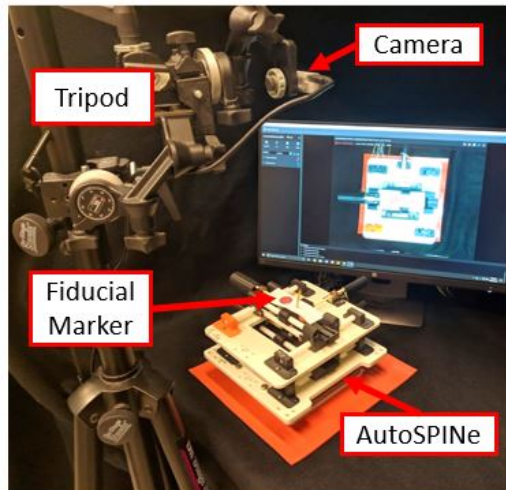
The bottom plane was kept stationary for the experiments to simplify the kinematics of the robot to single plane motion in two axes. This adjustment allows for the replacement of the two fiducials with a red circle printed on a small piece of paper (HP Laserjet 4700dn, 600dpi) mounted on the top plane. The printed fiducial ensures that there is a clear, flat circle to be found in the images, shown in Figure 3.31b. The benchtop (BT) experiments were designed to be repeated in MRI with minimal adjustments, so an RGB Camera (Intel Realsense) was mounted onto a tripod and placed over the robot, mimicking the coronal view in MRI, as seen in Figure 3.31a.

The camera used for the benchtop experiment has a native resolution of 640×480 pixels. Spatial resolution was set at 1.5 pixels per mm by placing the camera at a height of 33 cm. The images were downsampled using interpolation to match the spatial resolution of the MRI images which is 1 pixel per mm. The images were also cropped to match the FOV of the MRI, 128×128 pixels. An image acquired from this procedure is shown in Figure 3.31b.

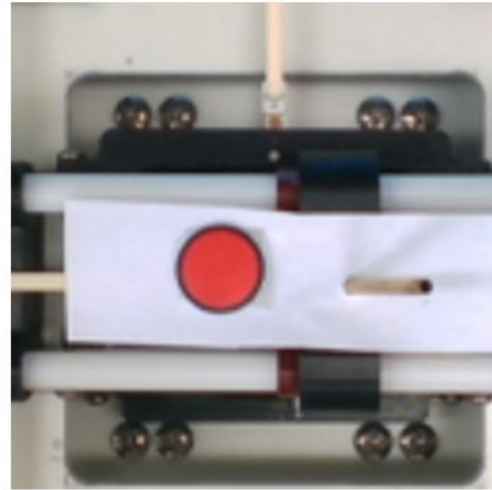
The experiments were performed as outlined in Table 3.1. The target position is considered to be the position of the fiducial markers when the first puncture in the trial is made.

For the bicubic interpolation trial, each image was interpolated to double the resolution and used for targeting and updates. The SR trial also follows the same procedure but for each image taken, the SR image construction procedure described in subsection 3.6.2 was followed to construct the SR image. An example of an SR image acquired from the benchtop experiments is shown in Figure 3.31d. 14 punctures were made in each trial to compare the positioning repeatability with the RGB camera base resolution, SR method, and bicubic interpolation. Each puncture point from the experiments is shown in Figure 3.32a. The distance of each point to the group means were calculated using a stereo microscope (Model S6D, Leica, Wetzlar, Germany)

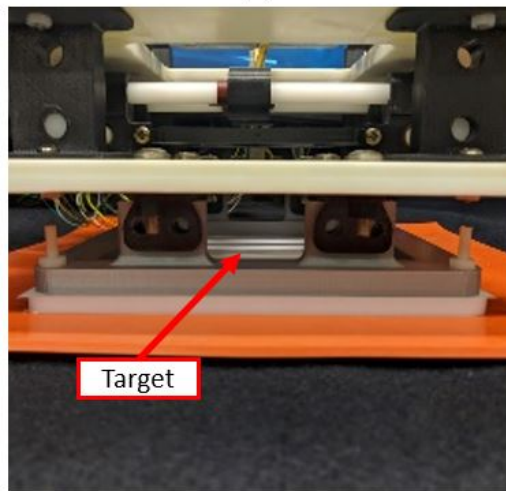
A two tailed F-test validates that the variances of the standard and SR groups are statistically different ($p < .05$). The standard deviations were 0.33mm and 0.18mm for the standard and SR targeting groups respectively, with the interpolation-based targeting group producing a 0.23mm standard deviation. The number of iterations and time needed for each puncture, as well as the puncture precision are summarized in Table 3.2.



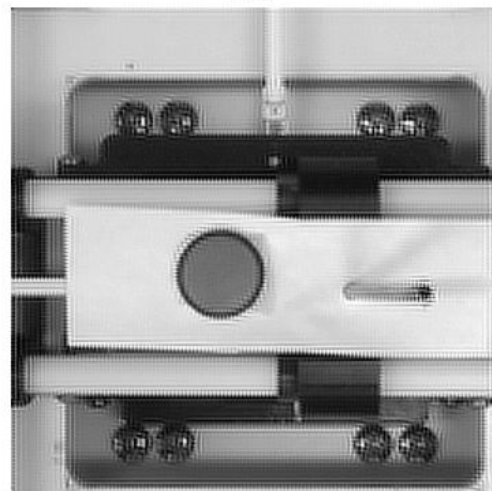
(a)



(b)



(c)



(d)

Figure 3.31: Benchtop experimental set up, b) Base resolution image acquired from experiment c) Target mounted below robot d) Super resolution image reconstructed from benchtop experiments.

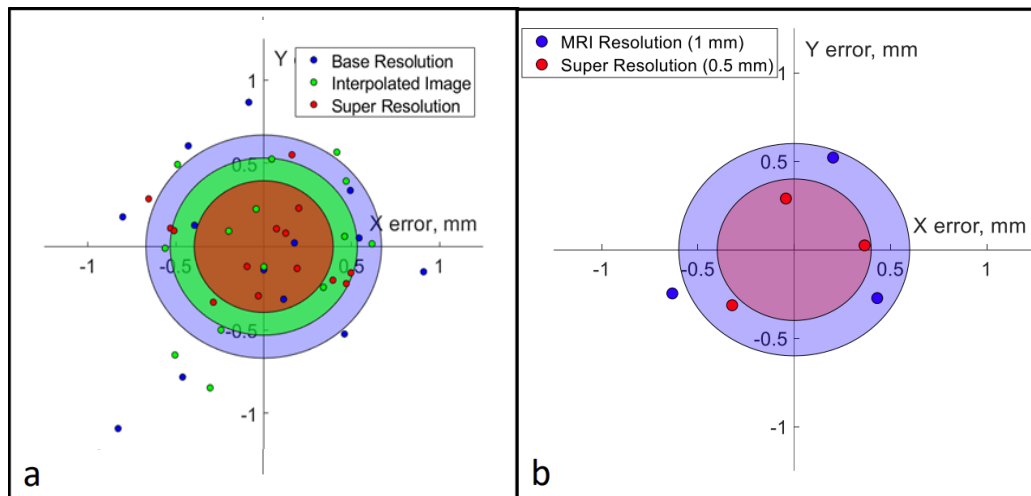


Figure 3.32: Experimental results, base resolution targeting in blue, interpolated targeting in green and super resolution targeting in red, circles represent the standard deviation of each group, a) Benchtop results, b) MRI results.

The MRI experiments were performed similarly to the benchtop experiments, with the robot secured rigidly onto the scanner bed as shown in Figure 3.33a. The fiducial marker used for the MRI experiments is shown in Figure 3.33b, mounted on the top stage of the robot since only two DOF positioning is considered for the experiments. Only one slice of the MRI images was used to calculate the centerpoint of the fiducial in that plane. A processed SR image with detected circle overlaid on image is shown in Figure 3.33c.

Three punctures were made in the base resolution experiment and the SR experiment. Experimental positioning results are shown in Figure 3.32b. Scanner time restrictions precluded collection of a statistically significant sample size, however, the standard deviation of the SR group was 33% smaller than that of the MRI resolution group, 0.60mm vs. 0.40mm. The number of iterations and time needed for each puncture are also summarized in Table 3.2.

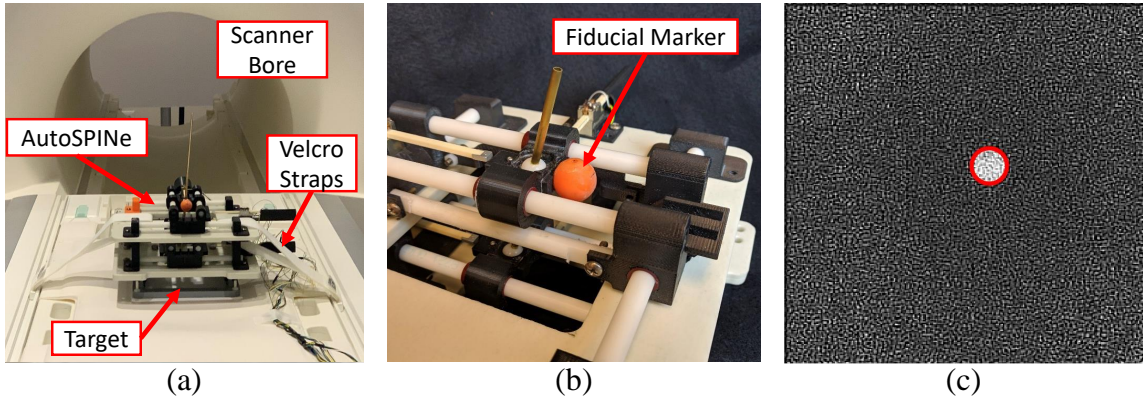


Figure 3.33: MRI experimental set up, b) Fiducial marker attached to top plane of robot, c) Super resolution image reconstructed from MRI experiments with a circle plotted based on image finding algorithm.

Table 3.2: Results of benchtop and MRI experiments

	BT	BT SR	BT BI	MRI	MRI SR
Number of iterations	1.08 (0.29)	1.58 (0.67)	1.17 (0.39)	2.00 (1.41)	1.50 (0.71)
Time (min)	1.08 (0.29)	4.75 (2.34)	1.08 (0.29)	7.00 (5.66)	26.50 (9.19)
Puncture precision (mm)	(0.33)	(0.18)	(0.23)	(0.60)	(0.40)

Mean (STD). Precision of needle puncture was evaluated by STD.

3.7 Applications beyond cellular therapeutics

Although the original application of this robot was the direct intraspinal injection of cellular therapeutics, the precision and MRI guidance capabilities are well suited to a number of other applications, some of which are described here.

3.7.1 Radiofrequency ablation

Radio frequency ablation (RFA) is a commonly used technique for the creation of a lesion in tissue. Because the RFA probes are small and typically lesions are localized to a specific target, there are a few RFA procedures that were explored as potential applications. One common procedure to treat low back pain is a median nerve ablation. In this proce-

ture the median nerve is targeted in a minimally invasive fashion. Although the procedure commonly takes place under manual fluoroscopy, X-ray or CT guidance, concerns about targeting accuracy, procedure time and radiation exposure may be alleviated by the introduction of an automated, MRI guided system. Reviews of the RFA literature have found that probe orientation is a determining factor in clinical outcomes [62], however currently, this orientation is controlled manually.

Another possible application is the treatment of osteoid osteomas. Osteoid osteomas are a benign tumor of the bone, most commonly occurring in children and adolescents. Treatment of the osteomas involves either surgical removal or RFA, with RFA usually preferable. Targeting of the nidus of the osteoma is critical to the success and viability of RFA, as errors in the probe positioning can have significant consequences for patients. The target nidus is typically small (under 2 cm), so image guidance is particularly important to ensure accurate location of the RFA probe.

Steerable needles have been developed for a variety of interventions, with both fixed and variable curvatures [63]. For RFA applications where the needle path is not as stiff or restricted as intraspinal injections, bent or steerable needles could potentially replace the straight needles/tools. In RFA, endpoint orientation is itself an important parameter beyond obstacle avoidance [62] and control of this orientation independent of trajectory may provide a significant benefit.

3.7.2 MRE

Magnetic resonance elastography is a novel MRI technique that enables estimation of tissue properties *in vivo*. A critical component of the imaging protocol is the creation of mechanical shear waves in the region of interest. These waves are typically created by an MR - conditional driver placed against the skin of the patient. By adapting the described robot design, the automated positioning of MRE drivers is another application, and is described in much more depth in Aim 3.

3.8 Aim 2 summary

This section presented the development and evaluation of a precise parallel plane robot for direct interventions. The use of a parallel plane positioning mechanism with direct actuation from linear piezoelectric motors produces a robot with linear positioning repeatability 6 times better than MRI resolution, ($3\sigma = 153\mu\text{m}$). The addition of positioning feedback allows accuracy up to the resolution of the imaging system, 74 microns in the case of an RGB camera, and 0.7mm in the case of the MRI scanner. Although the effect of the robot on SNR was minimal, full MRI conditionality testing should occur well before any human or animal subject experiments.

3.9 Future work

Although the developed robot and positioning system has been successfully demonstrated in the MRI environment[64, 65, 60], more experimental validation is necessary.

3.9.1 Animal model validation

Although not critical to the validation of the robotic positioning system itself, it is important to test the injection procedure on an animal model. A cadaver pig has been selected as the best candidate, and planning for this procedure is ongoing, in collaboration with GCMI (Atlanta, GA). Preliminary test fitting and positioning with respiration were performed as shown in Figure 3.34 on a live pig model. Positioning of the upper frame to align the cannula with a target on the skin was successful, but a lack of 3 dimensional internal images precluded more informative experimentation. Additional images of the pilot experiment are provided in Appendix B.

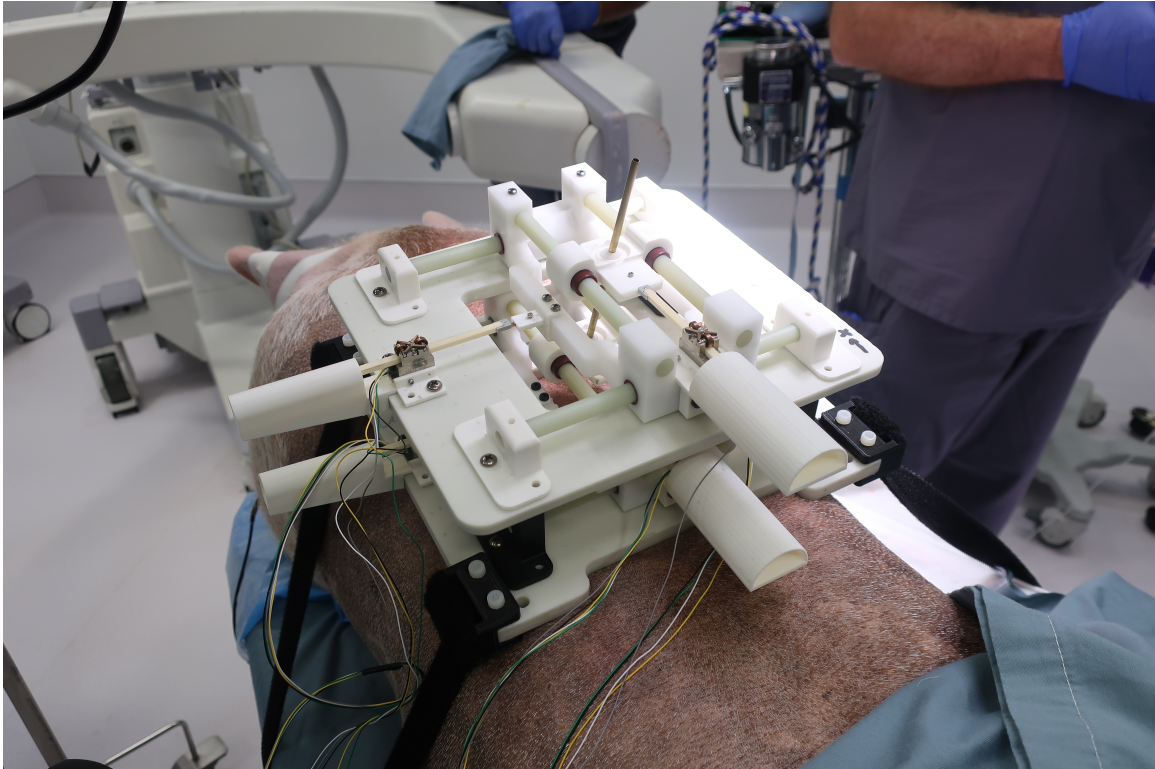


Figure 3.34: Animal model mounting and positioning pilot testing

3.9.2 Patient mounting

Patient mounting is a critical factor for the clinical use of this robot. Mounting must be stiff enough to counter the forces produced during the procedure. An experimental evaluation of lumbar punctures suggests axial forces around 5N [66]. A rigid 4 point mount was used for all phantom experiments, but is likely infeasible for use on patients. The prior manual device utilized pedicle screws, providing a secure method for mounting very close to the targeted anatomy [6]. While this method is likely to work for the robot as well, minimally invasive alternatives should be explored to reduce the burden on patients, and increase the potential applications of the robot. In the animal model pilot described above, the robot frame was mounted to the model with nylon straps and ABS brackets bolted to the lower base plate. This method is very fast to place, but allows for too much movement of the robot relative to the spinal cord. An intermediate option between rigid fixation and flexible mounts are Kirschner wires (K wires). These are semi-flexible rods that can be inserted

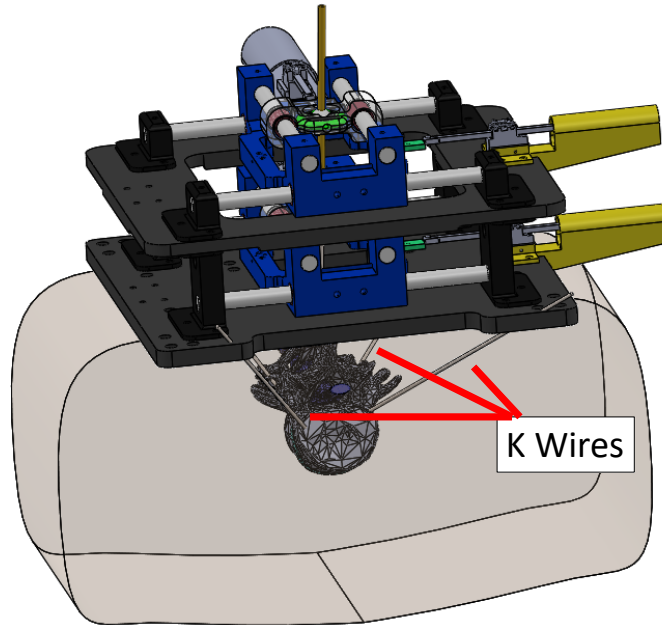


Figure 3.35: Robot mounting via K wire

into bone, and are commonly used for temporary fixation. A model of the spine, robot and K-wire mounting method is shown in Figure 3.35. K wire fixation is already a well established technique, and threaded K wires are capable of substantiating tension axial forces well above 100N without pulling out [67].

CHAPTER 4

AIM 3: MEASUREMENT OF IN-VIVO TISSUE PROPERTIES VIA THE DEVELOPMENT OF A NEW MAGNETIC RESONANCE ELASTOGRAPHY ACTUATOR

4.1 Magnetic resonance elastography background

Palpation of tissue to assess mechanical properties is one of the oldest medical techniques, and still in widespread use today[1]. For a large number of tissues, shear modulus is a clinically important mechanical property. Currently, this parameter is acquired by a non-invasive in vivo imaging technique, MRE, a phase contrast based MRI technique [68, 69]. MRE involves the generation of shear waves along the tissue of interest by an actuator and capturing of the displacement field, then calculation of elastograms through an inversion algorithm, a schematic is shown in Figure 4.1. The shear displacements are imaged via magnetic resonance imaging. The necessity of MRI compatibility significantly restricts available actuation modalities for this technique.

While previous work has primarily focused on the liver and brain, the intervertebral disc (IVD) is one of the important targets for MRE interrogation. Degenerative disc disease is a common cause of low back pain, and is present in up to 90% of older adults [70]. Degeneration of the IVD is often accompanied by structural changes, especially in the nucleus pulposus [71]. This has made the IVD and nucleus pulposus a target for MRE study. Previous research demonstrated the ability of MRE to distinguish between normal, mild, and severe degeneration of IVD [72]. Measurement of displacements transferred to the spine under different preloading conditions will enable early diagnosis of potential degenerative disc disease, which is the main cause of chronic back pain or low back pain. The small size of the IVD, along with the relatively high stiffness and shallow depth indicates that

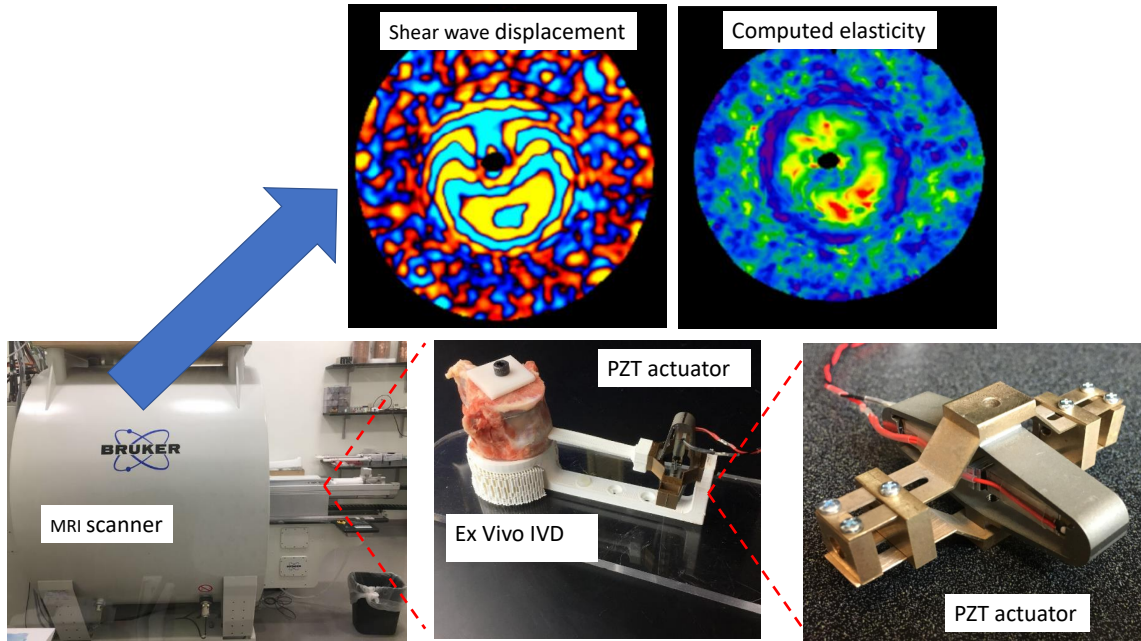


Figure 4.1: Magnetic resonance elastography imaging methodology

higher frequency excitation will result in improved elasticity measurements. Ex vivo MRE done on baboon spine at 1-1.5kHz showed promising results, but actuation developments are needed to obtain high-frequency results in vivo [73]. Actuator design is one of the most significant impediments to the clinical use of MRE in the IVD.

4.2 MRE actuators

4.2.1 MRE actuator specifications

MRE requires the production of mechanical displacements in the tissue of interest. In order for the displacements to be inverted and an accurate stiffness computed, it is critical that at least one wavelength fits within the dimensions of the region of interest. Wave speed is fixed for a given medium, so the only way to change the wavelength is by adjusting the driving frequency. In the planned application, the intervertebral disc, the smaller dimension of the disc is 2cm [74], and the velocity of shear waves in the disc has been reported as 3m/s [75]. The wave equation, $v = f\lambda$ can then easily be used to estimate the required driving frequency. The bare minimum case, where a single wave fits into the region of

interest is then a driving frequency of 150Hz, however a better option is to fit more than one wave in the disc. From the reported wave velocities in shear wave elastography [75], a range of frequencies was chosen so that for speeds up to 3σ (1.2m/s) above and below the mean, at least 5 wavelengths would fit across the IVD. This gives a maximum desired frequency of 1150Hz, with the lower end at 450Hz. Because increasing the minimum frequency increases the number of wavelengths, a margin was added to the upper end, and a desired frequency range of 600Hz - 1200Hz was chosen.

4.2.2 MRE actuator design

MRE actuator design has been a critical impediment to progression of the technique to small and stiff tissues. Mechanical characterization of deep-set smaller soft tissues has been limited due to wave attenuation and actuation frequency. Previous efforts have attempted to improve actuation technology, but have often involved force transmission methods that are inherently non-compact and frequency limited [76, 77]. Existing actuation methods include primarily remote electromechanical drivers and piezoelectric actuators, with limited work in pneumatic actuation. Electromechanical drivers require an alternating current to be passed through a coil that generates oscillatory motion. An extension is mechanically coupled with the moving coil through which the excitation is transmitted to the patient. Loudspeakers are commonly used as the actuation method, with pneumatic or rigid coupling to the patient. Some of the first MRE work involved a vibration motor rigidly coupled to a plate in the scanner bore by a long plexiglass rod [78]. The only actuation modality currently FDA approved is the pneumatic coupling of a loudspeaker type driver to the subject. This type of coupling solves the orientation and space constraints associated with rigid transmission rods, but is frequency limited because of the use of air as a transmission media. Nevertheless, pneumatic transmission systems are used clinically for MRE of the liver, as well as brain MRE in research settings [79]. Mariappan et al. demonstrated the concept of wave optimization in which phased-array drivers were used simultaneously. At certain

regions of interest, constructive wave interference was arranged by optimization of the timing of individual drive shafts [68]. Shrinking of the form factor of actuators should aid in future resolution enhancement methods by reducing placement constraints and increasing accuracy. In addition to the pneumatic transmission methods detailed above, pneumatic actuation methods have also been studied for MRE. Although work in this area is much more limited, two groups have presented designs utilizing unbalanced rotational mechanisms as MRE actuators [80, 81]. One design used a rotary ball actuator, in which air drives a polymer ball around a circular path [80], while the other used a 3D printed turbine [81]. Fundamentally, both designs include a rotary actuator driven by flowing air, resulting in an actuation frequency proportional to the driven rotation speed. This gives a truly pneumatic actuator with higher achievable frequencies than pneumatic transmission methods, with a reported maximum of 240Hz, still far too low for high resolution MRE of small tissues. It is possible that actuation frequency could be increased with a higher supply pressure, but with such high pressures and a rotational speed of 60,000 RPM for 1kHz actuation, safety will be difficult to ensure. Piezoelectric actuators have been explored as potential solutions to the transmission and frequency problems detailed in the preceding sections. Piezoelectric materials are MRI compatible, and MR safe actuators can be made from these materials, and safely placed in close proximity to patients with minimal image distortion [82]. Lever systems for displacement amplification combined with a piezo actuator [82], a piezoelectric bending element with needle positioned parallel to the plane surface [71], piezoelectric ceramic connected to a phantom surface with a slim plexiglass plate [83], and a piezoceramic actuator with a compliant mechanical amplifier [84] are few actuator setups that have been used for MRE measurements. The main problem with piezoelectric actuators is their effective displacement gets smaller as actuation frequency is increased. This is often mitigated by integration with displacement amplification structures. The viscoelasticity of soft tissues means that they exhibit frequency dependent behavior. This necessitates the use of multiple excitation frequencies during MRE for better mechanical characterization.

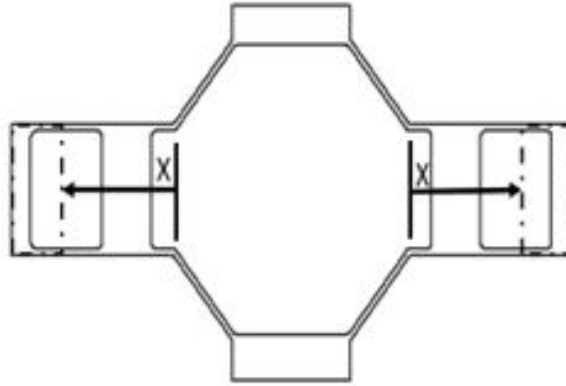


Figure 4.2: Tunable resonant actuator frame

While piezoelectric actuators for MRE have been proposed, they have fixed resonances, and thus are relatively bandwidth limited [84]. Sufficient displacement is only achievable over a small frequency range.

In this aim, we propose and develop an MRI compatible resonator whose resonance frequency was tunable. This allows a much larger range of MRE frequencies than previously developed actuators, allowing a larger number of tissues to be imaged.

Although piezoelectric actuators are capable of extremely accurate motion and high forces, they suffer from extremely small strains. The standard method to combat this is mechanical strain amplification. Detailed below is the design of a mechanical resonator with a tunable resonant frequency. The resonant frequency is adjusted by sliding the two masses on either side, changing both the inertial and stiffness characteristics of the actuator. The proposed design is shown in Figure 4.2. The resonator design was chosen to provide the amplified motion perpendicular to the actuation of the ceramic, as the dimension can be increased to increase the input strain. The length of the actuator frame was constrained by the bore diameter of the available small animal scanner for testing. The height was chosen to fit a commercially available actuator, and the thickness matched to available 655 bronze plate.

From this point, the wall thickness of the actuator was adjusted to capture the 600-1200

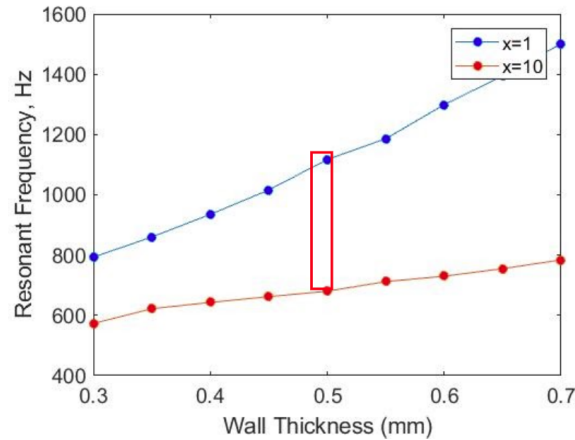


Figure 4.3: Effect of wall thickness in tuning range; red box shows the chosen value of 0.5 mm

Hz range estimated in subsection 4.2.1. FEM modal analysis was done on a preliminary model of the resonator to determine the thickness that would produce a resonant frequency range overlapping with the expected high frequency MRE range. The results are shown in Figure 4.3. From this, a thickness of 0.5 mm was used, as this gives a 680-1117 Hz resonance range. An implementation of the resonance frequency shifting design is shown in Figure 4.4. The sliding masses are embodied by the use of two linear piezoelectric actuators. In this case, scaled versions of Piezo LEGS 6N actuators are shown (PiezoMotor, Uppsala, Sweden), however any MRI compatible linear actuator is viable, as long as it fits within the geometric constraints. Tuning is not expected to take place at high frequencies, so even hydraulic or other slower actuators could be used. Linear piezoelectric actuators were chosen here because of the location precision required.

4.2.3 Finite element analysis

In addition to the parameter search detailed above, a modal analysis was performed to validate the resonant frequency tuning concept (ANSYS 19.1., Ansys, Canonsburg, PA). The first 4 modes of each fabricated frame and APA actuator were compared. To confirm that the piezo actuation does not excite the lowest two modes, a harmonic analysis was completed. The piezoceramic stack shown in Figure 4.4 and Figure 4.5 was replaced with

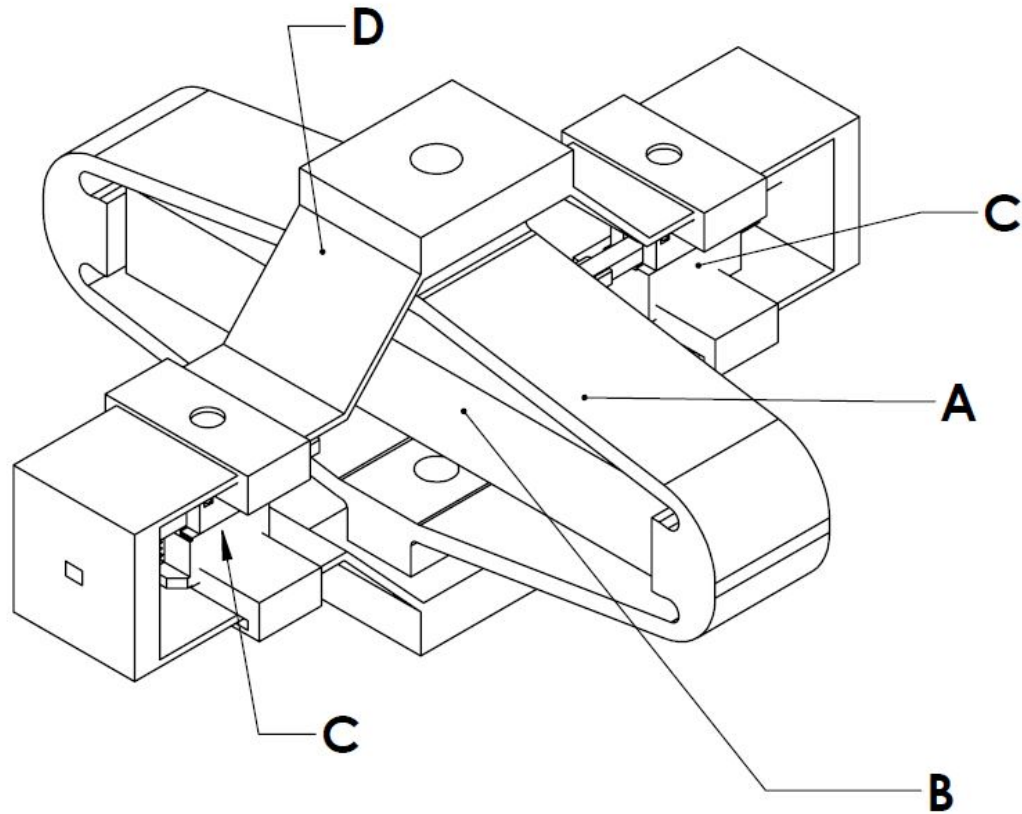


Figure 4.4: Resonance tuning mechanism; A) APA 150M frame, B) Piezoceramic stack, C) Linear piezoelectric actuator, D) 655 bronze frame

a set pressure on the contact faces of the APA actuator. This confirmed that the 3rd resonant mode was excited during actuation, providing motion along the desired axis.

Figure 4.6, Figure 4.7, and Figure 4.8 show the results of the modal analysis. Figure 4.6 shows the results for the first mass location, at the lower end of the range. Figure 4.7 shows results for the $x = 5$ mm mass location, roughly in the middle of the range, and Figure 4.8 shows results for the mass location at the upper end of the range. Figure 4.6 and Figure 4.8 represent the upper and lower bounds for the resonant frequency range of the actuator. Figure 4.9 shows the isometric views of the 3rd mode for each of the mass locations. A harmonic study confirmed that this is the dominant mode during actuation by the APA actuator's piezostack. Figure 4.12 shows the resonant frequency for each of the 3 locations.

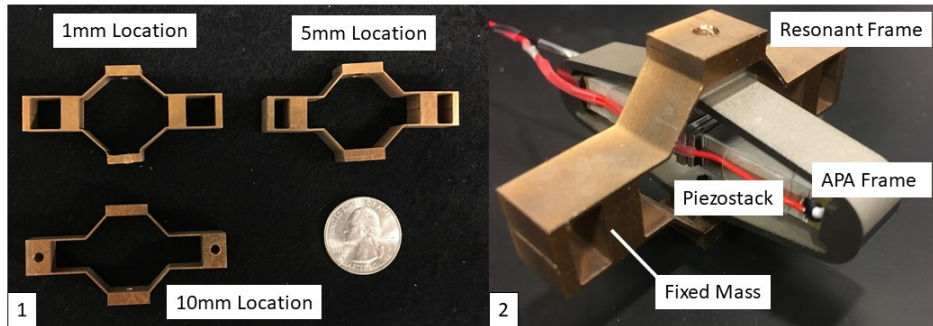


Figure 4.5: 1) Bronze resonant frames and 2) APA 150M actuator and resonant frame

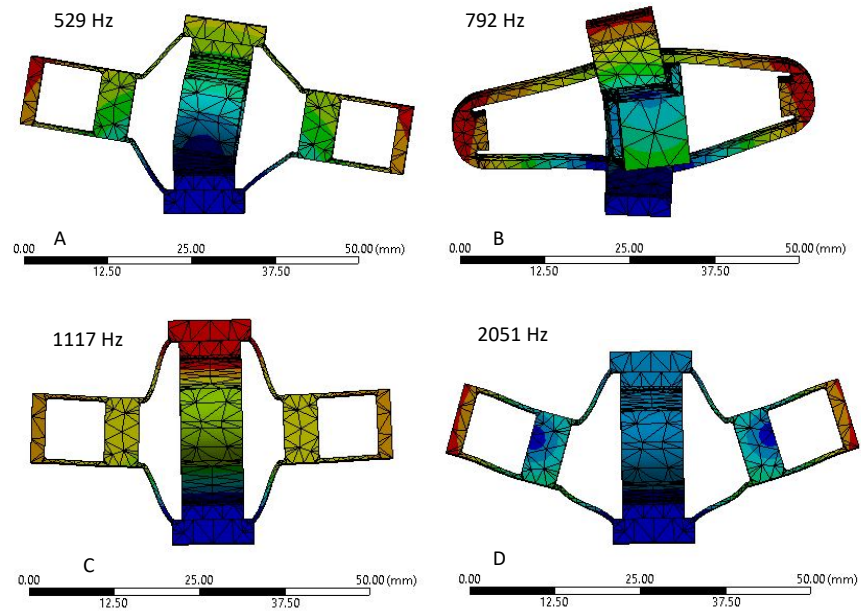


Figure 4.6: Mode Shapes and associated frequencies, 1 mm mass location

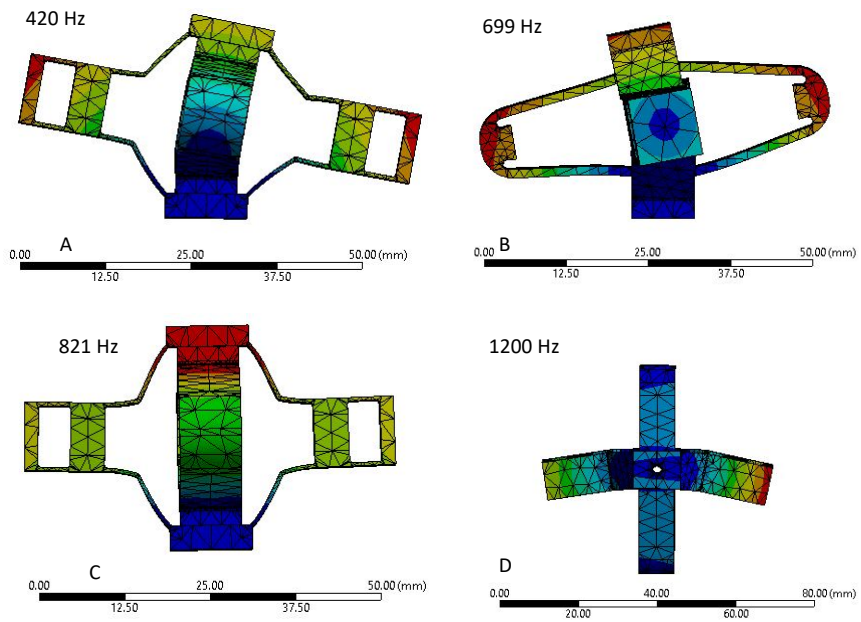


Figure 4.7: Mode Shapes and associated frequencies, 5 mm mass location

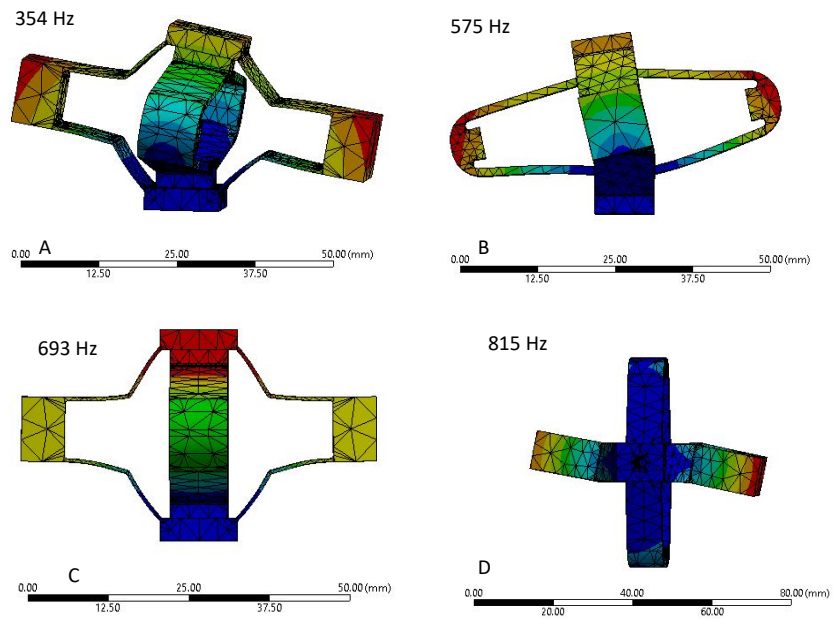


Figure 4.8: Mode Shapes and associated frequencies, 10 mm mass location

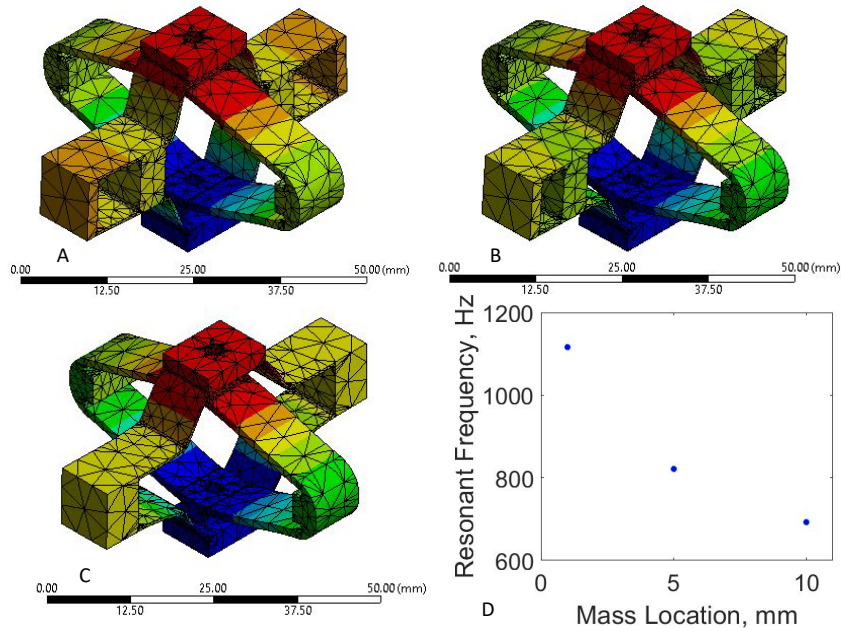


Figure 4.9: 3rd resonant mode displacement for each frame

4.2.4 Fabrication

For evaluation purposes, 3 fixed frames were machined from 655 silicon bronze as shown in Figure 4.5. Chosen mass locations were 1, 5, and 10mm, the lower, middle, and upper ends of the positioning range. This is analogous to the adjustment of mass locations by a linear piezoelectric actuator or another method. This resonant frame was combined with a commercially available amplified piezoelectric actuator (APA 150M, Cedrat Technologies). In practice, the resonant frame concept is not restricted to a particular choice of piezoelectric stack or amplifier. A continuously adjustable resonant frame was fabricated but not evaluated, and is shown in Appendix C.

4.2.5 Frequency tuning experimental validation

The simulation results presented in the preceding section were validated through experimental testing of 2 of the frames, the 1mm and 10mm versions, representing the full range of the proposed tunability. The piezoelectric actuator was driven by an amplifier (CA45, Cedrat Technologies), with a swept frequency sinusoidal input. The experimental setup is

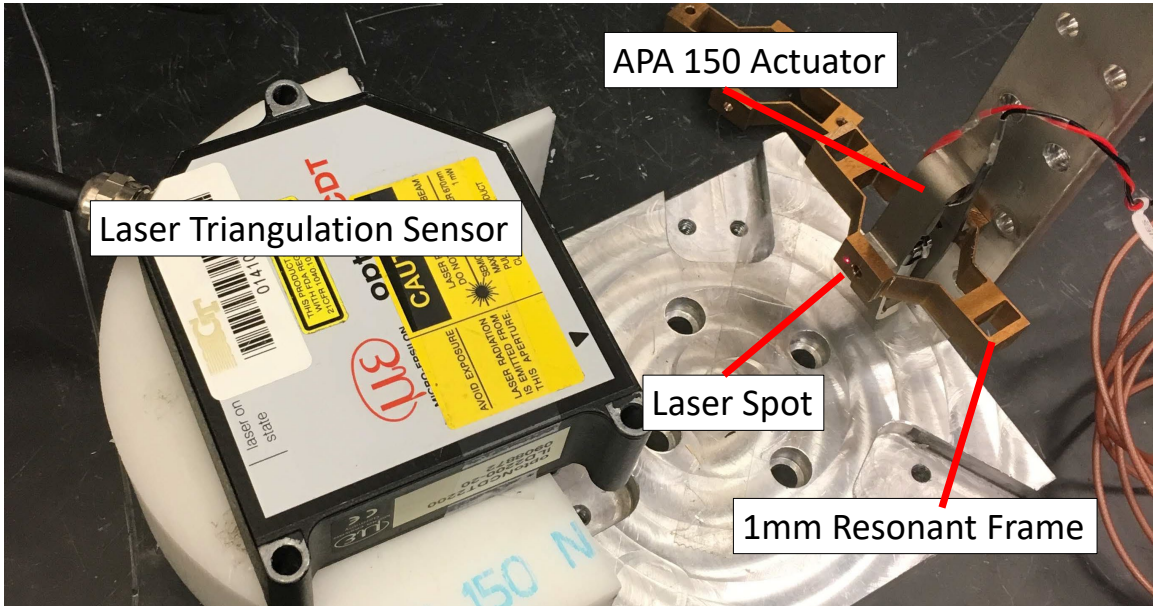


Figure 4.10: Experimental setup for MRE actuator resonant frequency measurements shown in Figure 4.10.

The laser triangulation sensor measured the position of the front face of the actuator with an analog output sampled at 5kHz (optoNCDT ILD2200-20, resolution: 0.3 μ m, Micro Epsilon, Germany). For each of the two frames, the driving frequency was swept in a window around the expected resonance over a 1 second period. 1.5 seconds of position measurements were recorded and saved, with the DFT computed in Matlab (fft).

The results of the experimental measurements for each frame are shown in Figure 4.11. Taking the peak of each spectrum as the resonant frequency, the resonant frequency of the frames is plotted and compared to the prior simulation results in Figure 4.12. Although there are minor differences in the range of adjustment and the exact resonance values, the experimental results match the simulated ones quite well.

4.2.6 MRI evaluation of piezoelectric drivers

A silicone rubber phantom was cast from DS30 and Ecoflex 00-50 silicone rubber (Smooth-On Corp. Indiana). The outer ring was poured first, with DS30, and then the inner region

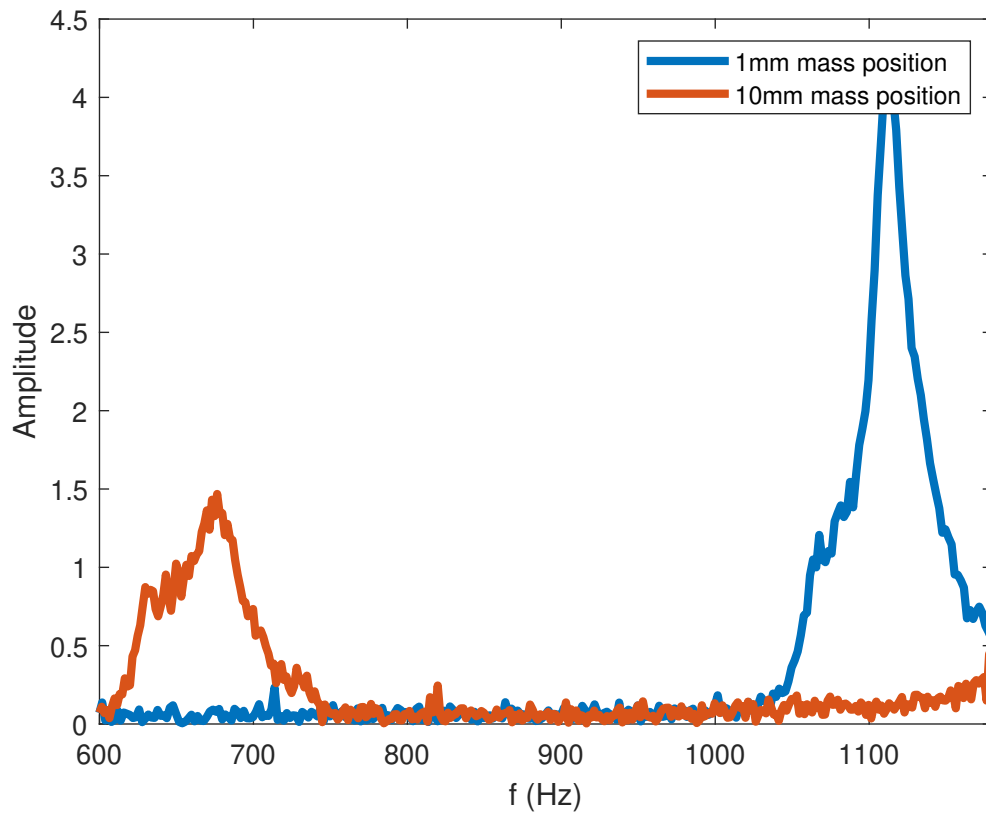


Figure 4.11: Amplitude spectrum for 1mm and 10mm frames

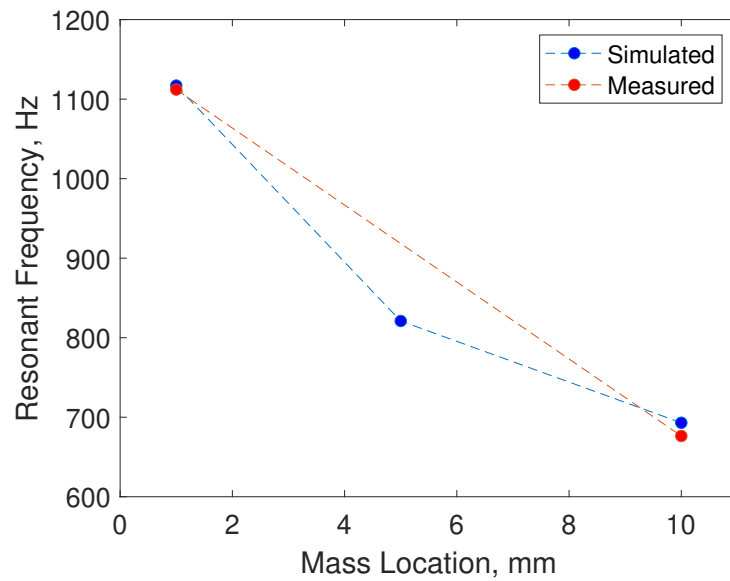


Figure 4.12: Estimated and measured resonant frequency for each mass location

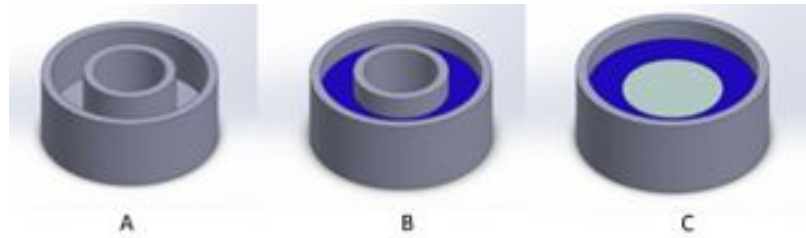


Figure 4.13: Silicone phantom and casting process

was poured from Ecoflex 00-50. The area and relative area of the two regions, as well as the thickness were approximately matched to the human intervertebral disc [74], a potential tissue for high frequency MRE imaging. The mold and 2 step casting process are shown in Figure 4.13. The silicone was degassed in a vacuum chamber to minimize bubbles. The mechanical properties of the individual silicone components and interface were not tested or compared to those of the IVD, as the phantom here only exists to validate the use of the piezoelectric actuators for MRE and assess any image artifacts.

Imaging was conducted in a 7T scanner (Bruker). The passive actuator was placed 10cm from a silicone rubber phantom, with a rigid polycarbonate connecting rod between the two, as shown in Figure 4.14. Imaging was performed in the Mount Sinai TMII Imaging core facility, NY.

Figure 4.15A demonstrates the MRI compatibility of the fabricated actuator assembly. The dark regions noted in the silicone are caused by air bubbles in the phantom. The small shading in the top of the image is likely caused by the active driver, a longer transmission rod could address this, although the depth of the IVD below the skin should also mitigate this effect.

Figure 4.15B shows the computed displacement field. A sharp division is seen between the two phantom materials. This is likely due to poor adhesion in the boundary region, due to the dissimilar materials or curing times. This interface is an important area of study, but phantoms and ex-vivo work to adequately capture the mechanical behavior of the biological boundary are still an active area of research [85]. It is not clear if there is wave transmission

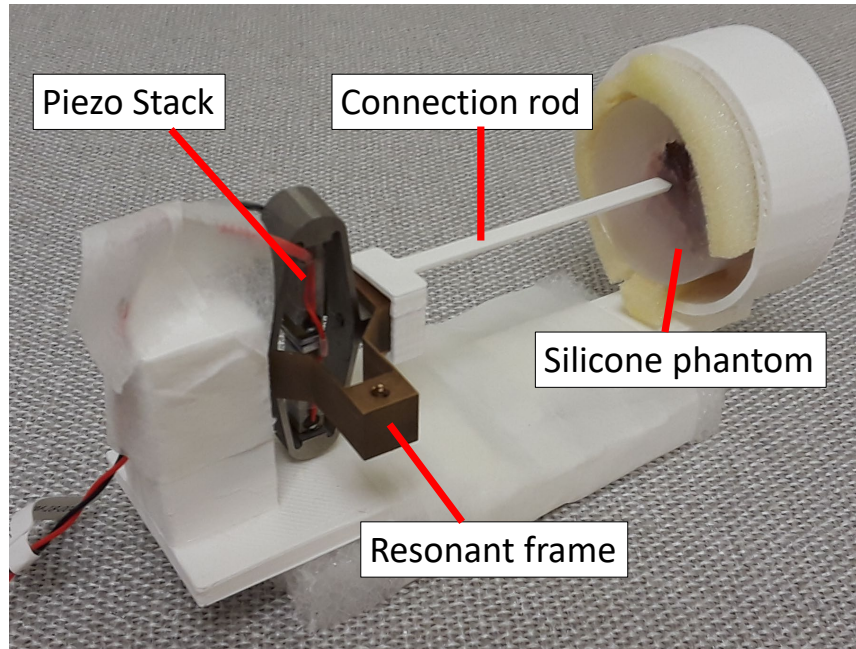


Figure 4.14: MRI evaluation setup

across the boundary between the materials, and what the properties of that transmission are. For this reason, the following analysis occurred only on the NP portion of the phantom.

The collected images were also processed in MREWave, an open source MRE inversion package. The region outside the phantom was masked with a magnitude masking function, and amplitude was bandpass filtered between 2 and 20 Hz using the built in Gaussian filter. Because of unknown scanner/protocol parameters (FOV and menc), only a rough stiffness value could be computed. The results are shown in Figure 4.15B and Figure 4.15C.

The mean shear modulus of the NP region of the phantom was estimated to be roughly 0.78kPa. A shear modulus for the silicone rubber used was not available, but instead was estimated from the available M100 value and the theoretical relationship between young's modulus and shear modulus and the estimated limit for Poisson's ratio in silicone rubbers (0.5) [86]. The known M100 value of 82kPa then results in an estimated shear modulus, G , of 27kPa. While the estimated and measured values differ, it is difficult to ascertain if this is due to temperature, non-linear behavior of the material with high strain rates, or an error in the inversion. Nonetheless, these results provide a promising first step for the use

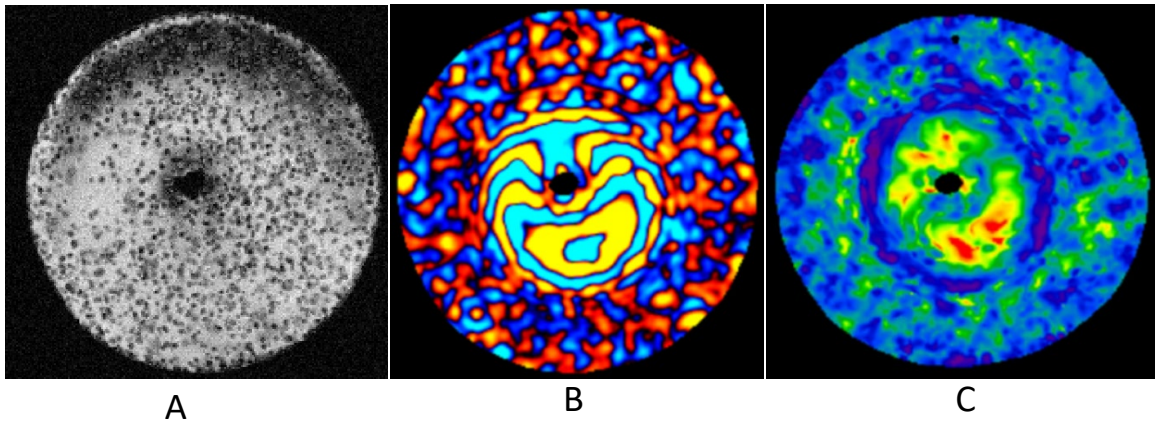


Figure 4.15: MRI evaluation images A) Magnitude image, B) Computed displacement image, C) Stiffness map, mean shear stiffness in the center ROI is 0.78 kPa

of tunable resonant actuators in MRE of the IVD.

4.3 5 DOF positioning of MRE actuators

The purpose of all MRE drivers, including the ones developed in this chapter is to produce sufficient shear waves in a specific region of interest. In the original application of MRE, the liver, this was a relatively large region of interest (ROI), with a 14cm diameter [87]. However, as applications of MRE expand beyond larger tissues to smaller and stiffer ROIs such as the intervertebral discs, the placement of shear waves in the tissue requires more intentional direction. For this reason, the robot designed in Aim 2 was adapted to the 5 DOF positioning of MRE drivers.

4.3.1 Planned procedure workflow

In the preceding aim, the expected workflow of the procedure necessitated the surgeon performing the injection, so the robot only required 4 DOF positioning rather than 5. Posi-

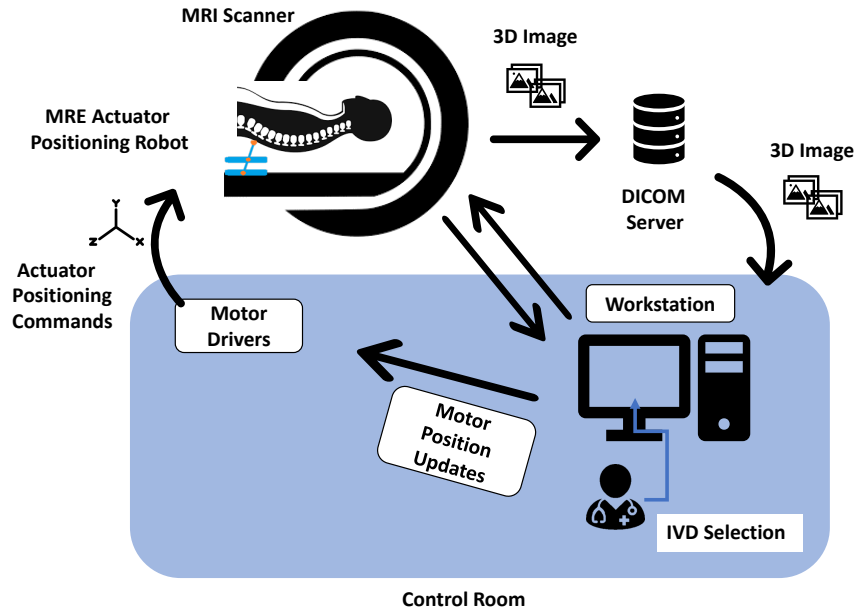


Figure 4.16: Workflow for robotic positioning of MRE drivers

tioning of the MRE driver must take place actively, while in the scanner bore, so the robot requires an additional degree of freedom. Positioning of the MRE actuator is a two stage process, with the first step using image jacobian based control to place the driver in the correct configuration against the patient, then a second positioning process to adjust the configuration based on the obtained MRE images. The workflow is shown in Figure 4.16

4.3.2 Mechanical design

The robot design in Aim 2 was modified for use in MRE actuator positioning. The same parallel plane mechanism is used, but a 5th DOF is added, with the actuator placed between the two ball joints. Because the needle guide is replaced by the 5th DOF actuator, the diameter of the ball joints and collars was increased as well. The CAD model and prototype robot are shown in Figure 4.17. Although the design is compatible with the original piezoelectric actuators, sub-mm accuracy is unnecessary for MRE driver positioning and hydraulic actuators were used for the MRI testing version of the robot. Each actuator consists of a rigidly mounted syringe, a connection tube and a syringe placed in the control

room. For the purposes of the MRI experiments, the actuators were positioned remotely, but manually operated. The reinforced delrin base plates were replaced with clear lexan, as the intended mounting of the robot is flush with the scanner table, not above the patient. The clear stages enable faster setup and initial orientation of the robot. The linear positioning of both stages is performed by hydraulic actuators (syringe-tube-syringe system). As the mechanical vibration source, an MR compatible piezo actuator (APA150M-NM, Cedrat Technologies) is used. This actuator is attached to the tip of the rod that mounts to the 5th DOF actuator and passes through the upper ball joint. The rod contains an internal fiducial cavity for determining the MRE actuator's position and orientation in the scanner. A representative MRI image showing the 3 dimensional view of the robot in the scanner is shown in Figure 4.18.

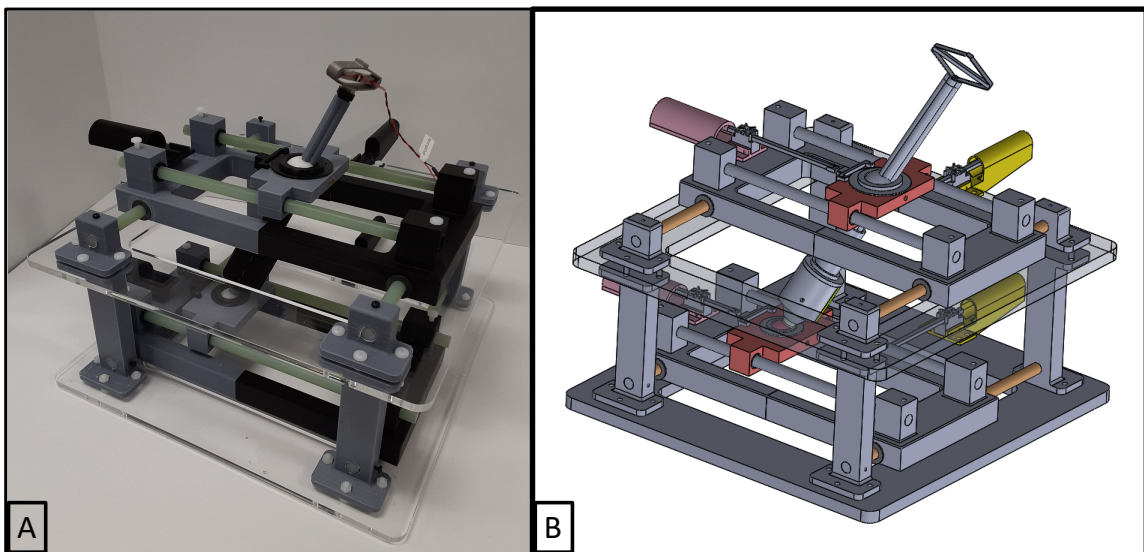


Figure 4.17: 5 DOF MRE actuator positioning robot, A) Completed prototype, and B) CAD model

4.3.3 Control

Jacobian inverse control was used, with visual feedback from the MRI images providing endpoint position measurements, and each of the 5 actuators controlling one DOF. The

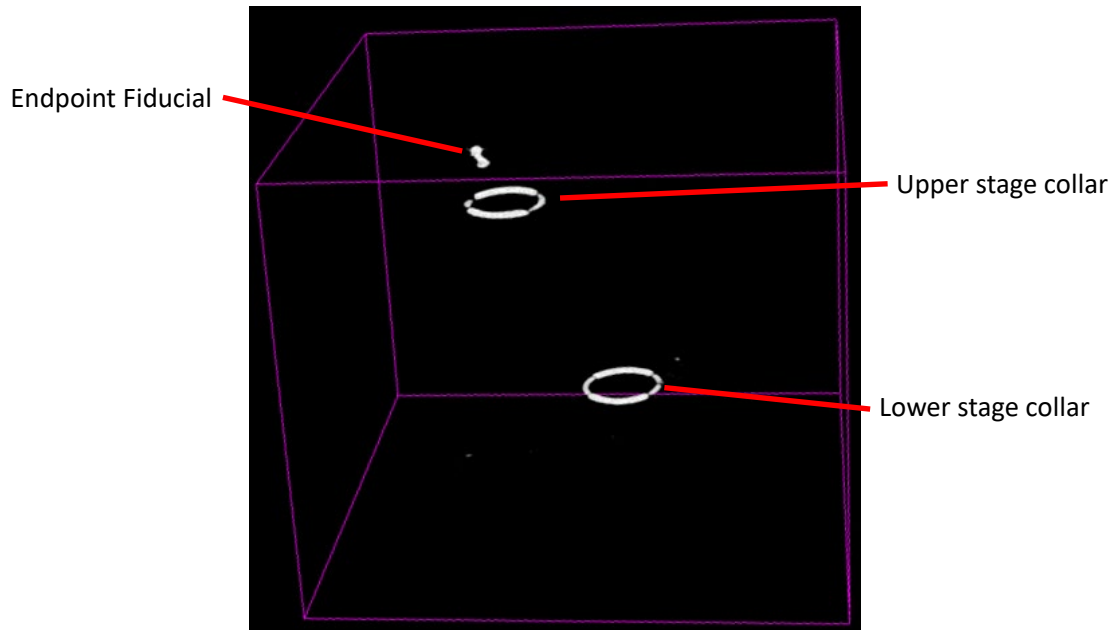


Figure 4.18: MRI scan of the positioning robot, with planar collar fiducials and endpoint fiducial.

Jacobian used comes directly from the image coordinate frame, and as the transformation between robot frame and image frame is not known *a priori*. The forward kinematics are given below, with the variables used shown in Figure 4.19.

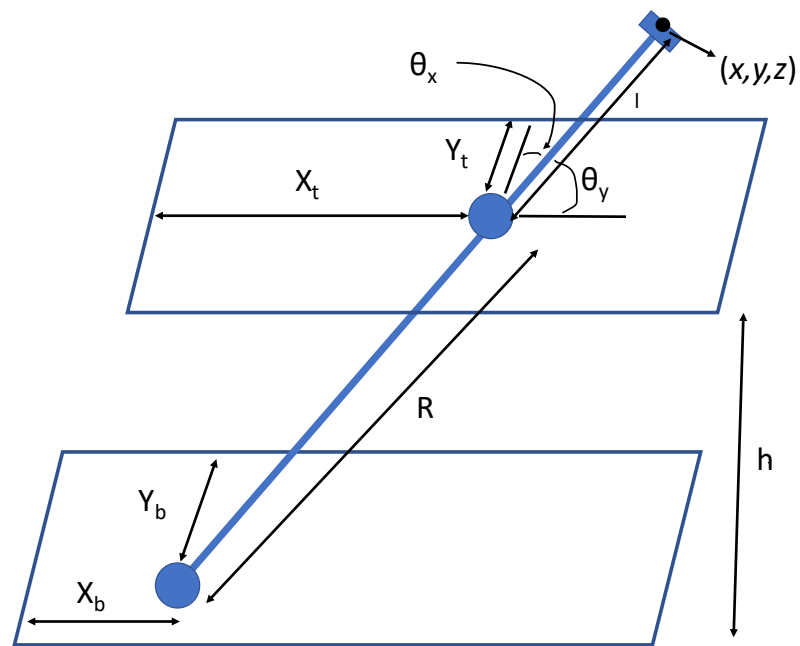


Figure 4.19: Kinematics diagram of the MRE positioning robot

$$\begin{bmatrix} x \\ y \\ z \\ \theta_x \\ \theta_y \\ \theta_z \end{bmatrix} = \begin{bmatrix} -l(x_t - x_b)/R + x_b \\ -l(y_t - y_b)/R + y_b \\ -lh/R \\ \text{atan2}(y_t - y_b, h) \\ \text{atan2}(x_t - x_b, h) \\ \text{atan2}(y_t - y_b, x_t - x_b) \end{bmatrix}. \quad (4.1)$$

For analysis and evaluation purposes, the kinematic Jacobian was computed by differentiating Equation 4.1, this is identical to the image Jacobian when the image and robot coordinate frames are aligned. The last line, θ_z was left out, as the z axis orientation is not salient to the robot or procedure.

$$\begin{pmatrix}
\frac{l(2xb-2xt)(xb-xt)}{2R^3} - \frac{l}{R} - \frac{l(2xb-2xt)(xb-xt)}{2R^3} + 1 & \frac{l(2yb-2yt)(yb-yt)}{2R^3} - \frac{l}{R} - \frac{l(2yb-2yt)(yb-xt)}{2R^3} + 1 & \frac{l(2yb-2yt)(xb-xt)}{2R^3} - \frac{l}{R} - \frac{l(2yb-2yt)(yb-xt)}{2R^3} + 1 & \frac{xb-xt}{R} \\
\frac{l(2xb-2xt)(yb-yt)}{2R^3} - \frac{hl(2xb-2xt)}{2R^3} & \frac{l(2xb-2xt)(yb-xt)}{2R^3} - \frac{hl(2xb-2xt)}{2R^3} & \frac{yb-yt}{R} \\
0 & 0 & 0 & 0 & 0 & 0 & -\frac{h}{R} \\
\frac{h}{(xb-xt)^2+h^2} & -\frac{h}{(xb-xt)^2+h^2} & -\frac{h}{(yb-xt)^2+h^2} & -\frac{h}{(yb-xt)^2+h^2} & -\frac{h}{(yb-xt)^2+h^2} & -\frac{h}{(yb-xt)^2+h^2} & 0 \\
0 & 0 & 0 & 0 & 0 & 0 & 0 \\
0 & 0 & 0 & 0 & 0 & 0 & 0
\end{pmatrix} \quad (4.2)$$

This 5 dimensional Jacobian relates actuator positions and the changes in position and orientation of the MRE driver. However, unlike the 4 DOF version, a single jacobian cannot be used for all potential targets in the workspace. The sign of the entries associated with the Z position and the change in X and Y due to motion of the 5th DOF actuator changes depending on the relative position of each pair of X actuators and Y actuators. For example, the sign of the first entry in the last column, $\frac{x_b - x_t}{R}$, clearly depends on the relationship between x_b and x_t . When the signs in the Jacobian are incorrect, the direction of computed updates will also be incorrect. This sign error will result in accumulated positioning errors if the target configuration is in a different quadrant than the initial configuration. The placement of additional fiducials to estimate the robot configuration and quadrant based Jacobian selection is a potential solution, but unnecessarily complicates and extends the imaging and positioning protocol. Instead, a two step positioning procedure was evaluated.

4.3.4 4 + 1 control scheme

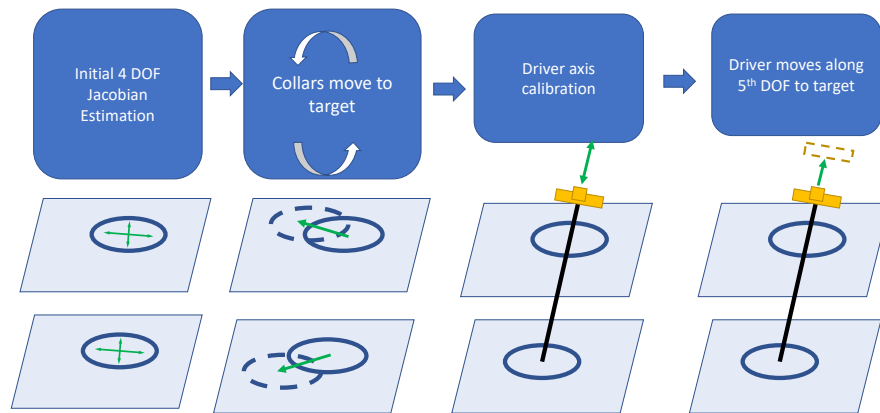


Figure 4.20: Two stage driver positioning process

Figure 4.20 shows the planned control method to produce 5 DOF positioning of the MRE driver in a two stage process. First, the two parallel plane actuators are controlled with a 4 DOF Jacobian to move the ball joint collars to a target position. Second, the driver

axis actuator is advanced to move the driver into contact with the skin and complete the positioning. This process can be used to effectively position the driver very close to the final target position. If another parameter is desired for servoing (such as maximizing the displacement field in a specific ROI) the 5 DOF jacobian can then be estimated in place and used for small adjustments near the initial target.

4.3.5 Benchtop positioning experiments

The control method and robot design were validated in a 5 DOF positioning experiment. The MRI conditional hydraulic actuator described above was replaced with a ferromagnetic DC linear actuator, due to availability constraints. The planar base used the same linear piezoelectric actuators as in Aim 2. The DC motor was controlled on a time basis with 1ms of power supplied compared to a single step of the rotary actuator. Throughout the rest of this section, "step" refers to a single step of the linear piezoelectric actuators as well as 1ms driving time of the linear DC motor. Position measurements were obtained via a 6 DOF magnetic tracker fixed in place of the MRE actuator and the robot endpoint. Only the first 5 DOF were used in the course of these experiments, replicating the information obtained from measurement of the 5 DOF endpoint fiducial in Figure 4.18. The experimental setup and positioning of the magnetic tracker are shown in Figure 4.21.

Positioning performance was evaluated in a mock positioning trial, with two different target positions from opposite quadrants of the workspace, due to the sign changes discussed above.

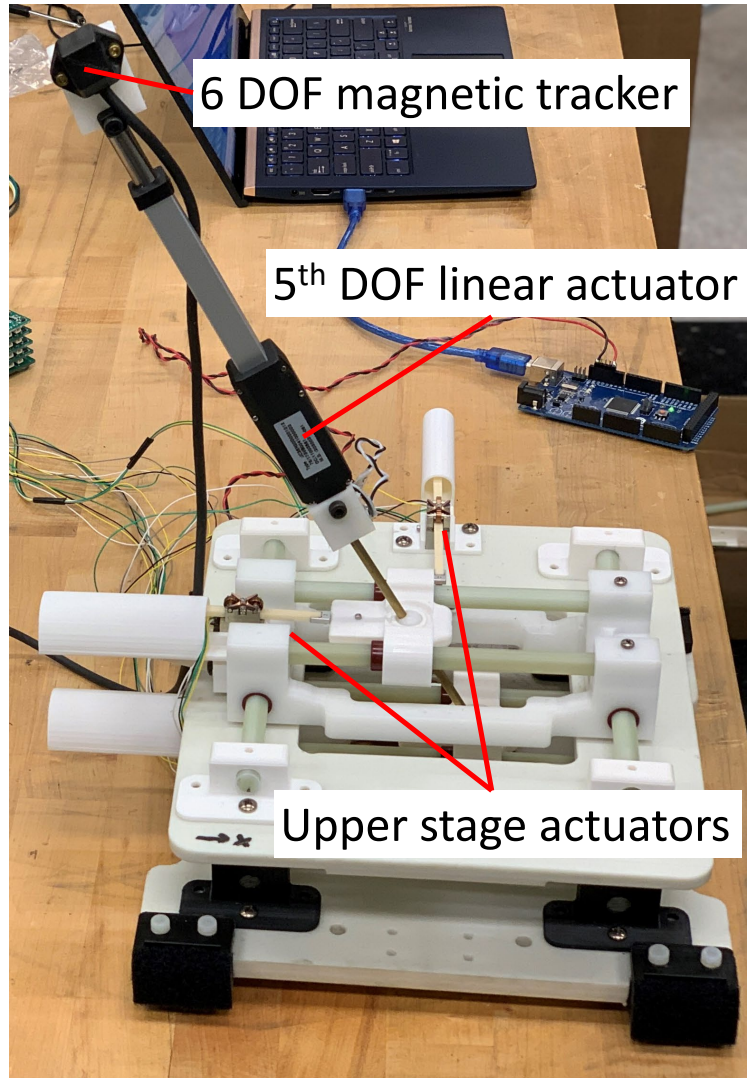


Figure 4.21: Benchtop experimental setup

The results of the positioning experiments are shown in Figure 4.22. After 10 iterations final errors were 3.55 mm and 0.89 degrees

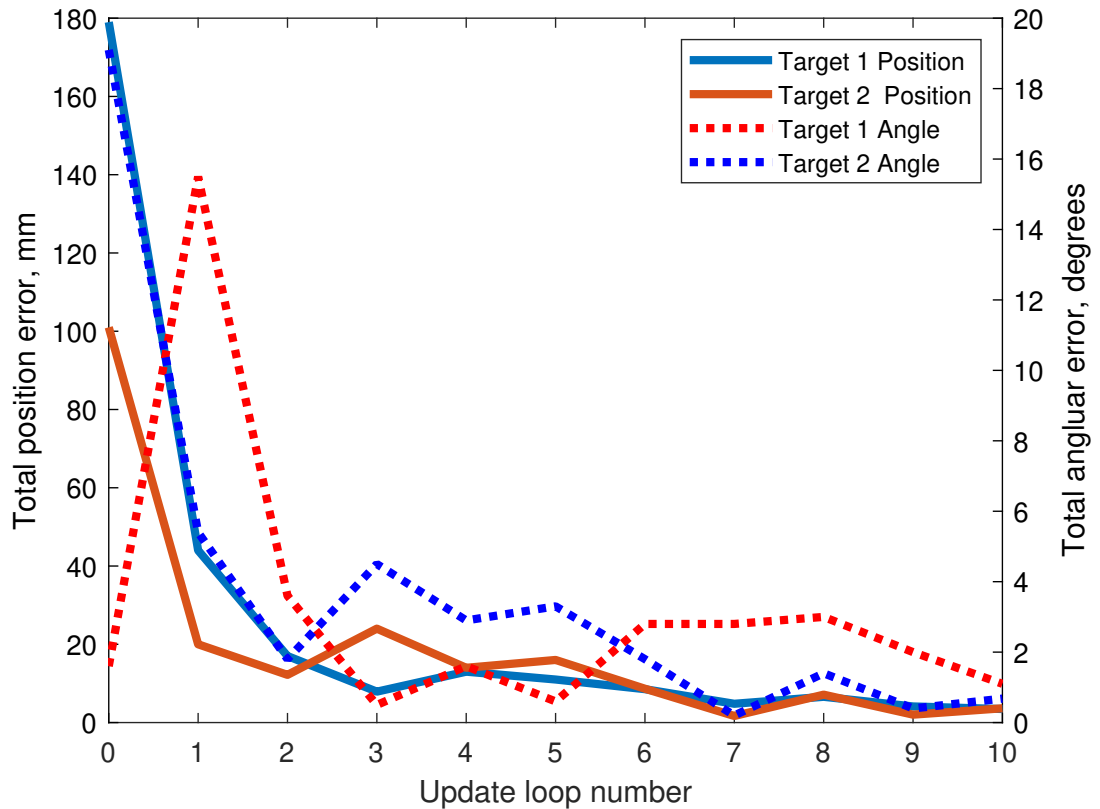


Figure 4.22: Benchtop experimental results, both position and orientation error over 10 updates for two different target locations

4.3.6 Two phase positioning control

In addition to the 5 DOF experiments performed above, the second control configuration of a 4 DOF planar positioning step, with advancement of the 5th DOF actuator as the final step was evaluated, as described above. Planar positions were measured via an RGB-D camera (Intel Realsense). In this case, a 4 DOF image Jacobian relating the planar position of each ball joint to the motion of the actuators was used. After each ball joint reached the desired location, the 5th DOF actuator was extended to place the endpoint at the target location. Location and orientation accuracy was measured via the visual fiducial shown in Figure 4.23. In the benchtop experiments reported, target locations and endpoint locations were experimentally determined prior to beginning the experiments, because of

visual occlusion caused by multiple components of the robot. In the MRI scanner, only the fiducials are visible, so target locations for the ball joints can be computed from a desired endpoint location and orientation.

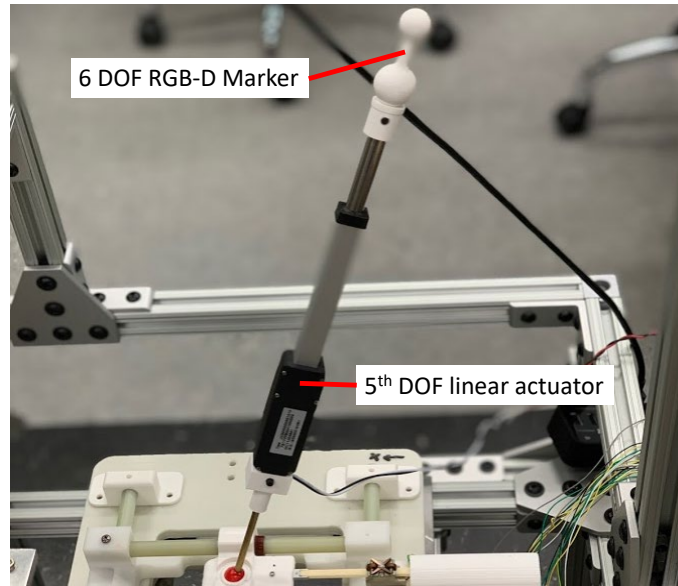


Figure 4.23: Benchtop RGB-D fiducial mounted to robot, endpoint position and orientation were found via the center positions of the two spheres

Positioning results are shown in Figure 4.24. After 7 updates with the 4+1 control method, final mean error was 1.8mm and 0.78 degrees. This level of accuracy is sufficient for positioning of an MRE actuator, and slightly better than the 5 DOF control method above.

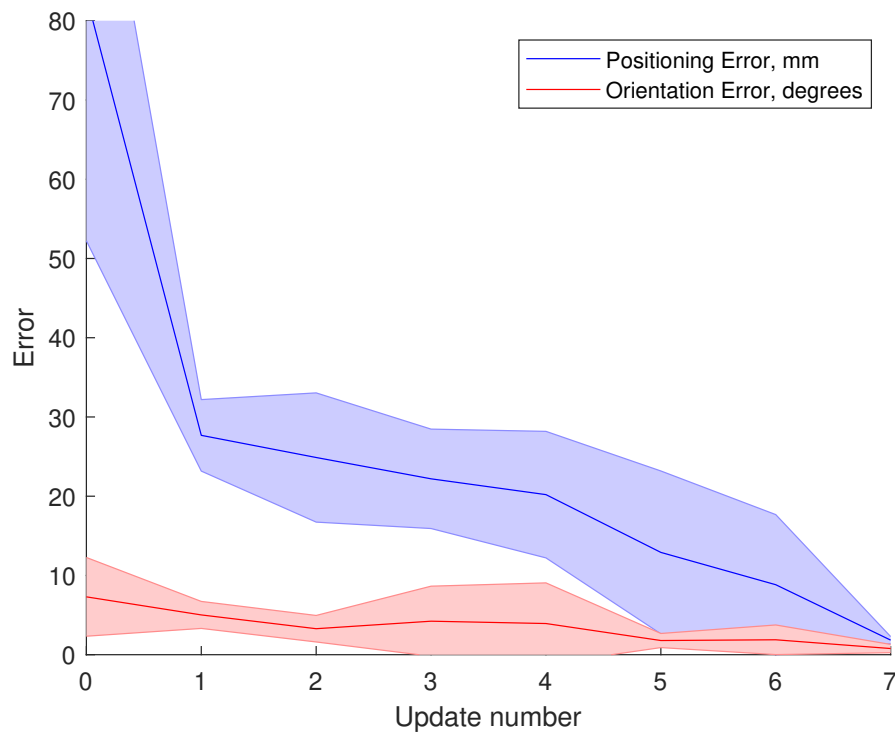


Figure 4.24: Benchtop experimental results, orientation and position over the planar and 5th degree of freedom positioning protocol, mean and standard deviation

4.3.7 MRI evaluation

To validate the conceptual basis for this portion section, the prototype robot was evaluated in a series of MRE imaging experiments. Experimental evaluation of the prototype system was performed in a 3T MRI (Siemens Trio), as shown in Figure 4.25. The 5 DOF frame was placed below a phantom structure containing a gelatin phantom, with the body RF coil placed above the phantom. Morphological and MRE sequences were utilized, with the morphological scans providing robot configuration confirmation. MRE scans were performed for each of the 3 robot configurations. Actuation was provided via the MRI compatible hydraulic actuators manually positioned so as to reproduce the effective range of the robot.

Figure 4.26 shows the clear differences in displacement fields achieved by varying the contact angle of the MRE driver. This result has not previously been demonstrated in MRE,



Figure 4.25: Experimental Setup.

and the applications are numerous. Particularly, orientation of the wave field will enable realization of advanced MRE techniques to investigate smaller and stiffer tissues located in regions of the body beyond the reach of traditional driver technologies.

4.4 Aim 3 summary

The results highlighted in the preceding section demonstrate the validity of the proposed frequency tuning mechanism. Over a small 10 mm adjustment range, a 436 Hz resonance range was observed. Because the change in resonance is continuous with the position of the mass, the entirety of this range should be usable for MRE imaging. Changes in the geometry, materials, and piezo actuator will enable adjustment of this range to specific applications. In addition, because the tunable resonator is similar in geometry to the typ-

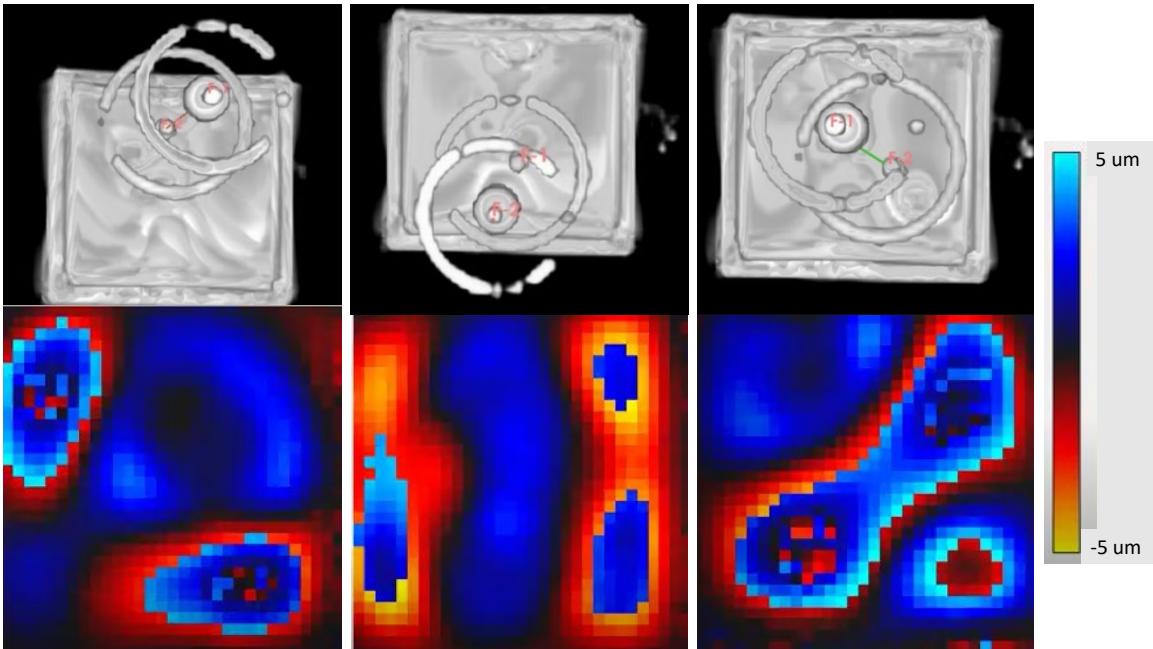


Figure 4.26: Displacement fields and associated robot configurations

ical mechanical amplifier, “stacking” or nesting of these structures should provide larger amplification ratios and an even larger frequency range.

The reported positioning results and pilot MRE experiments demonstrate both the feasibility and utility of an active MRE driver positioning system. The parallel plane platform and 4 +1 control method were capable of successful positioning with total position error under 2mm.

4.5 Future work

The initial results provide an important proof of concept for the tunable resonance actuator design [88] and active positioning robot. Future incorporation of multiple actuators on active positioning systems will enable more effective MRE of the IVD.

CHAPTER 5

CONCLUSION

In this work, precise robotics methods were applied to a variety of areas of the human neurological system. Analysis, classification and device development were used to aid in the diagnostic utility of the deep tendon reflex, while a robotic tapping device was used to modulate SSEPs with future applicability to rehabilitation. In the spine, an MRI guided robot was developed for intraspinal injections of cellular therapeutics. Because of the robot and control design, the robot can also serve as a platform for the development of super resolution positioning methods and other precise image guided interventions beyond the spinal cord. This work also detailed the design and evaluation of novel, tunable resonance drivers for MRE, as well as their combination with a 5 DOF robot for active driver positioning. These developments should aid in bridging the gap between current MRE methodologies and expanded regions of interest, particularly the IVD. The contributions of this work can be summarized for each aim as follows:

- Aim 1: The development of a tapping classification method and implementation in an assistive application, the characterization of human tapping performance, and the development of a robotic tapping device for repeatable stimulation and investigation of somatosensory evoked potentials.
- Aim 2: The development of a high precision MRI guided robot for direct interventions, contributions in MRI based feedback positioning.
- Aim 3: The development of tunable resonance MRE actuators enabling high frequency MRE targeting the IVD, development of the first active driver positioning robot for MRE

5.1 Future work

Future work towards these aims includes modeling and modulation of the SSEPs, application of the parallel plane robot to RFA and MRE, and continued development of high frequency MRE actuators. Preliminary work has started in understanding the therapeutic role of SSEPs, and leveraging the analysis and instrumentation development of this thesis will expedite that process. The results reported in Aims 2 and 3 demonstrate that the robot design is capable of producing high accuracy 4 and 5 DOF configurations, patient mounting, sterilization and other imaging modalities are all future avenues of research. The single actuator displacement results in Aim 3 motivate future exploration of arrayed drivers for even more targeted MRE imaging.

Appendices

APPENDIX A

SSEP PREDICTION FROM STIMULATION INTENSITY

As part of the work in Aim 1, modulation of the SSEP for therapeutic use was explored. In order to increase the understanding of the role that mechanical stimulation plays in the SSEP amplitude and waveform, ML methods were applied to prediction of the SSEP. Difficulty in the collection of paired stimulus-response data precluded statistical significance in the results, and the significant variability in individual response measurements limit the effectiveness of predictions without a much larger data set. Given that future advancements in MEG and EEG recording may enable noise reduction sufficient for single trial SSEP measurement [89], the methods applied here show significant potential for prediction of SSEPs. The content of this section is intended to both inform the reader of the potential for future work in this area, and give anecdotal support for future experimental and analytical methods.

A.1 Modulation of the SSEP

SSEPs record the sensory response to peripheral stimulation. The sensory response is measured as the electrical potential between the sensory cortex and a neutral location, recorded via electrodes on the scalp. Traditionally, SSEPs are produced by averaging hundreds of individual responses to produce a single plot of the mean response. This is done due to the significant noise present in individual recordings. A standard SSEP provides a clear indication of the sensory response to stimuli, however variability between individual stimulations is erased by trigger averaging of all trials together. Variability in stimulation intensity during DTR elicitation is expected, so an attempt was made to predict these variations in the evoked potential sensory response.

A.2 Prediction via LSTM

The goal of this work was to predict EEG recording's from hammer acceleration. As described in the previous section, there is an underlying relationship between the stimulation and response, but it is often obscured by variability and noise. LSTM networks were chosen because of their suitability for sequence prediction. Feature vectors consisted of normalized acceleration data for each tap. Response vectors consisted of EEG recordings. The network consisted of a sequence input, bidirectional LSTM layer, a dropout layer sandwiched between fully connected layers and a regression output layer.

A.2.1 Constant intensity prediction

The data used is the same data reported in the SSEP modulation section. 255 total recordings were available, split between training and testing the model. 200 pairs were used for training while 55 were reserved for testing.

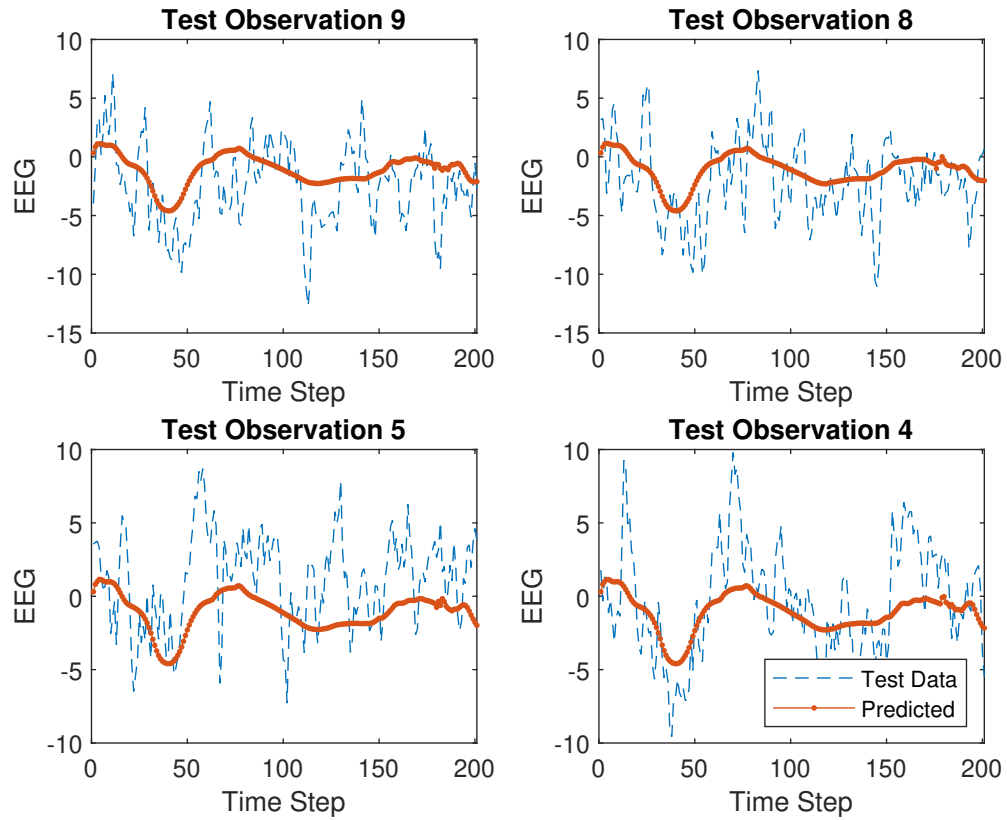


Figure A.1: Representative predictions and EEG data for 4 individual taps

Example prediction results are shown in Figure A.1. The higher frequency components of the recording are not well predicted, although this may be due to their random nature. A comparison of the individual predictions and trigger averaged SSEP is shown in Figure A.2. The individual predictions are very similar to the mean result, but with some individual variability.

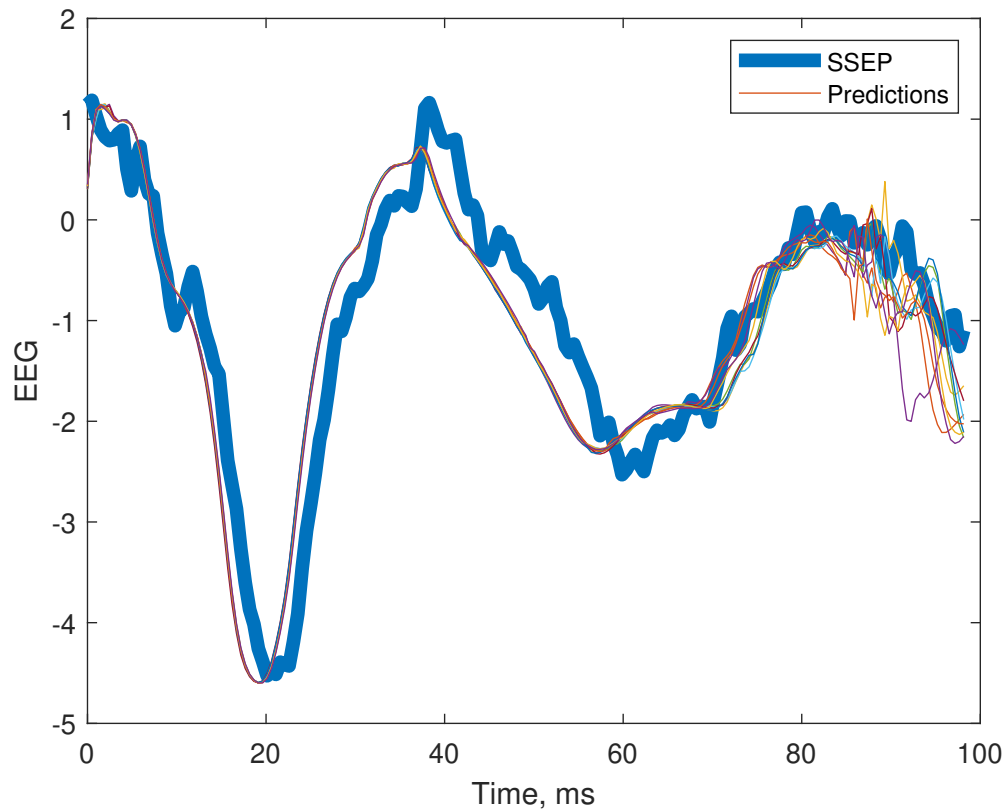


Figure A.2: Standard prediction method and LSTM network predictions of individual SSEPs

From the RMSE results shown in Figure A.3, the errors of the individual predictions were slightly lower than prediction directly from the SSEP, however that difference was not statistically significant. A potential explanation for this is that the robotic stimulation was so consistent that there was not a large amount of variation in the true sensory response, so the network produces a similar output for each tap, as differences are mostly attributable to noise rather than stimulation variability. Intentionally varied stimulation was evaluated next.

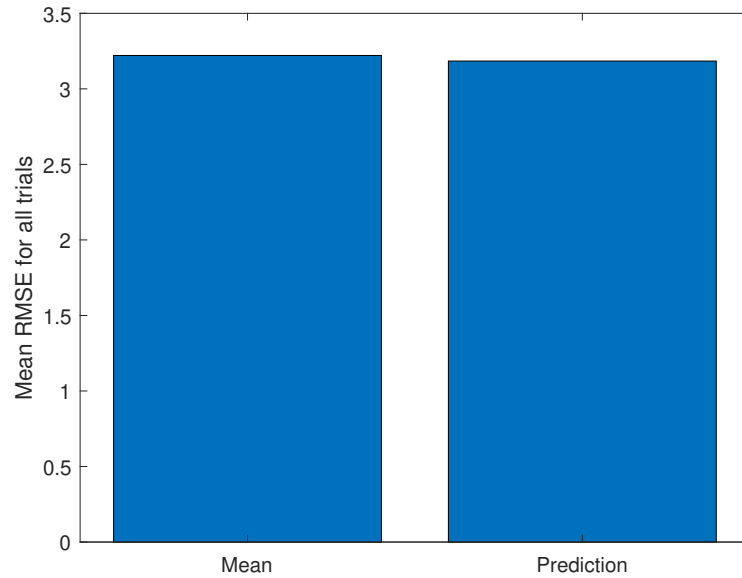


Figure A.3: Mean RMSE results for the prediction of individual EEG responses to tapping from acceleration, mean is the standard SSEP signal combining all stimulus averaged trials, prediction is the individual LSTM network prediction from hammer acceleration

A.2.2 Variable intensity SSEP prediction

The robotic stimulation variability was much lower than that of human stimulation, however intensity is also easily modulated, and has been shown to modulate SSEP amplitude [90]. For this reason all of the trials collected from a single subject at two different tapping intensities were combined into a single training set. 255 recordings were available at each intensity. 20 samples from each intensity were reserved for testing, and not used for network training. The same network structure was used as in the preceding section. Randomly selected individual prediction and EEG recordings from the 40 test pairs are shown in Figure A.4. The individual predictions vary slightly, with the one from the higher intensity tapping (observation 12) taking a slightly different form than the other 3.

From the results shown in Figure A.5, it is clear that the network is capable of predicting the general class of the two response modes from the hammer acceleration sequence data. The overall SSEP (green line) represents the SSEP in the absence of stimulation intensity

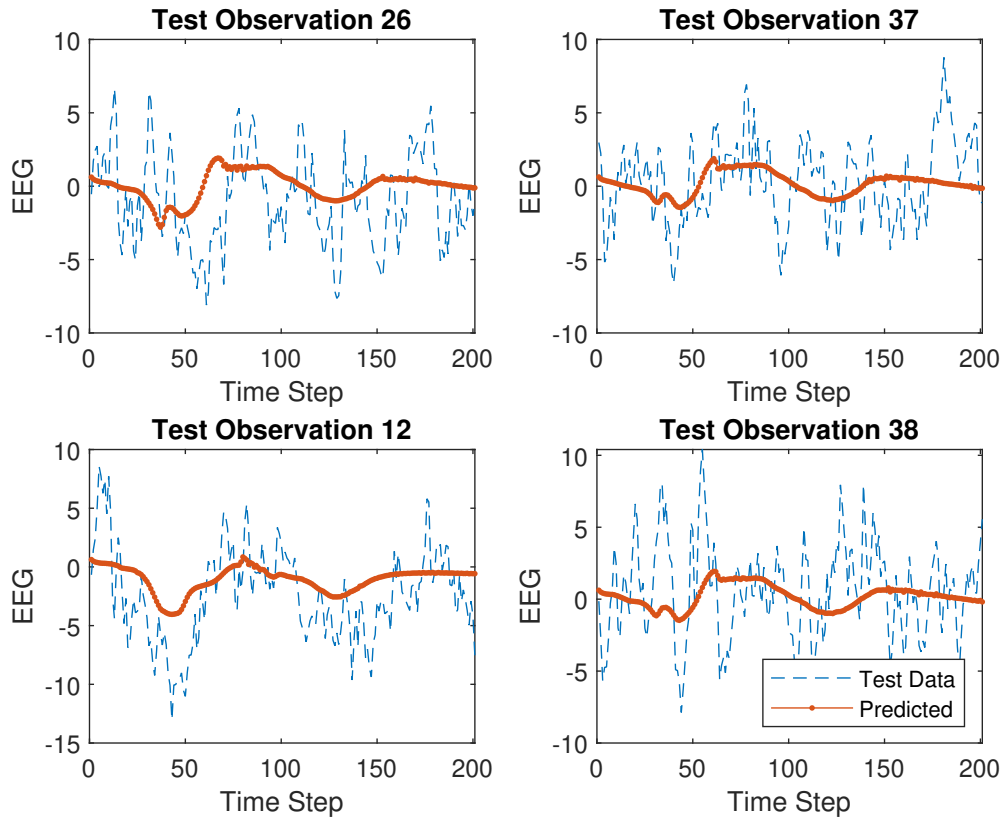


Figure A.4: LSTM predicted EEG and recorded EEG for individual trials at 2 tapping stimulation intensities

knowledge. The LSTM network gets much closer to the high and low intensity responses for each individual recording than the overall mean. While in this case, intensity was varied intentionally, these results provide good support for the potential use of LSTM networks for evoked potential prediction in other cases where stimulation intensity displays significant variability. Again, although the mean error was lower for the LSTM network based predictions, the difference was not statistically significant.

A.3 Future work

The results reported in this section were promising, but not statistically significant. The likely explanation is that the amount of noise inherent to EEG recordings makes direct prediction difficult or impracticable. Filtering of the data via both digital signal processing

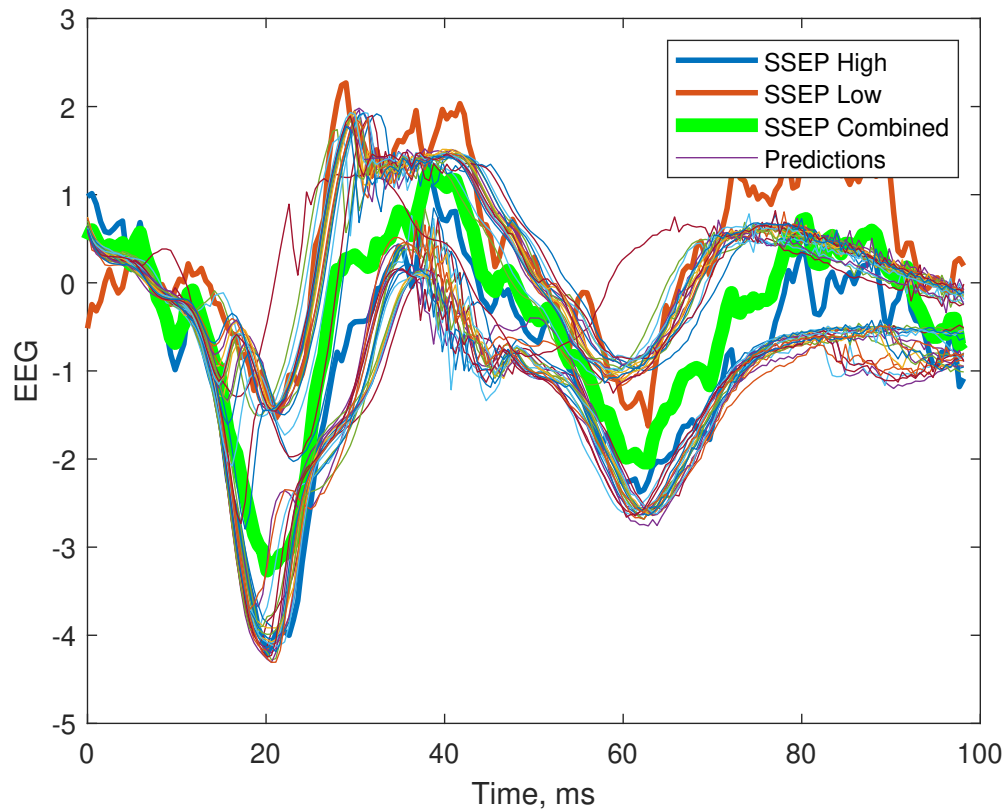


Figure A.5: Standard prediction method and LSTM network predictions of individual SSEPs

and hardware based noise reduction methods may help to reduce this problem. In addition recently published work on MEG (a magnetic analog to EEG) showed promise in producing single trial SSEP measurements [89]. The application of these methods to SSEP prediction in the future would likely aid in the clinical usefulness of this exercise. Any future work should also seek to understand and mitigate the challenges associated with recording SSEPs in many subjects.

A.4 Experimental subject considerations

Significant difficulty was encountered in successful recording of evoked potentials, while some of this is attributable to the sensitive nature of the hardware involved, subject variability seemed to play a role as well. During pilot evaluation of the methods reported, it was

not possible to obtain SSEP measurements from a number of the subjects (3/5), despite up to 3 separate sessions for some individuals. There could be multiple contributing individual factors such as hair thickness and style, as well as experimental comfort. This variability between subjects needs further study, and could encourage the use of needle electrodes or other subject screening and preparation methods.

APPENDIX B

ROBOT MOUNTING AND CONTROL IMAGES

While the selection of trajectories may appear easy when given a phantom, and clear view of the robot, in practice trajectory selection is much more difficult. Visual occlusion of the robot and difficulty interpreting the 2 dimensional images both impact the ability of the operator to select suitable trajectories. Figure B.1 is provided as a reference for this difficulty, and the motivation for the development of the VR system.



Figure B.1: Control room showing scanner, animal model and 2D image views

Additional images of the robot mounting and imaging setup for the animal model pilot are shown in Figure B.2, and Figure B.3.

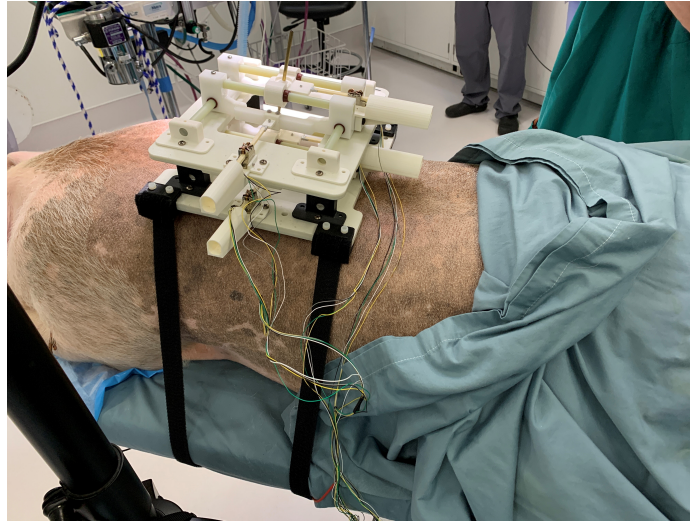


Figure B.2: Robot Mounting



Figure B.3: Camera setup

Figure B.4 shows a radiographic image of the robot mounted to the animal model,

the cannula is easily recognizable, however radiopaque fiducials are necessary if the MRI guided control scheme is to be implemented under CT.

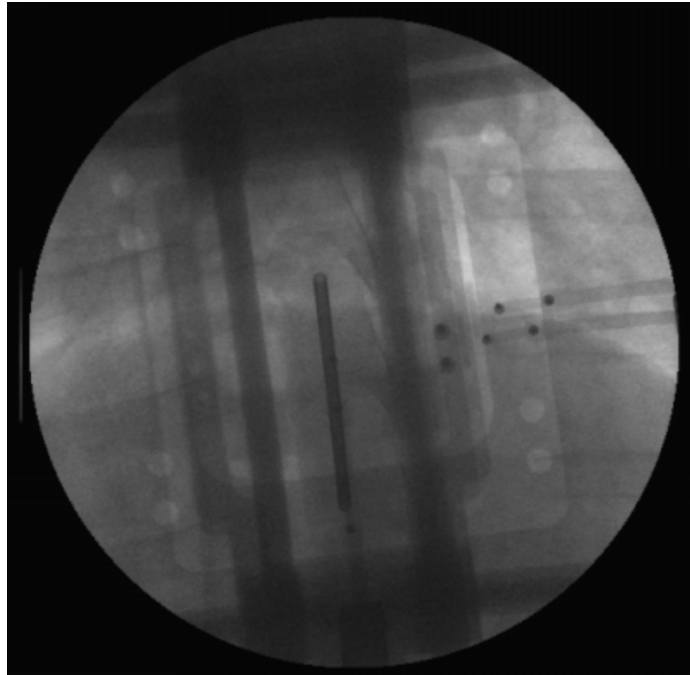


Figure B.4: Radiograph

APPENDIX C
ADJUSTABLE RESONANT FRAME

Figure C.1 shows the manually adjustable resonant frame, future work will evaluate the use of this frame in MRE.

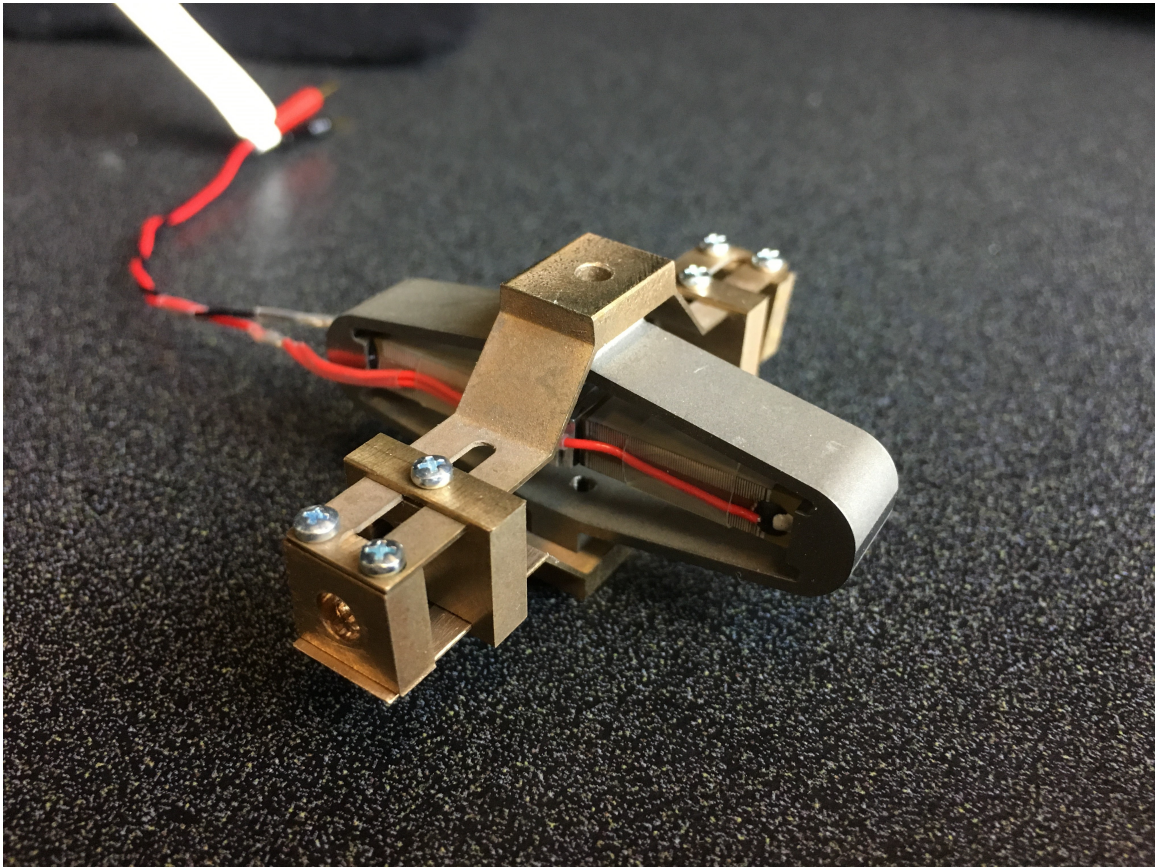


Figure C.1: Resonant frame

REFERENCES

- [1] H. K. Walker, "The origins of the history and physical examination," in *Clinical Methods: The History, Physical, and Laboratory Examinations*. 3rd edition, Butterworths, 1990.
- [2] F. Pinto, "A short history of the reflex hammer," *Practical Neurology*, vol. 3, no. 6, pp. 366–371, 2003.
- [3] S. Singh, S. K. Venkatesh, Z. Wang, F. H. Miller, U. Motosugi, R. N. Low, T. Hasanein, P. Asbach, E. M. Godfrey, M. Yin, *et al.*, "Diagnostic performance of magnetic resonance elastography in staging liver fibrosis: A systematic review and meta-analysis of individual participant data," *Clinical Gastroenterology and Hepatology*, vol. 13, no. 3, pp. 440–451, 2015.
- [4] Y. K. Mariappan, K. J. Glaser, and R. L. Ehman, "Magnetic resonance elastography: A review," *Clinical anatomy*, vol. 23, no. 5, pp. 497–511, 2010.
- [5] M. Janowski, C. Engels, M. Gorelik, A. Lyczek, S. Bernard, J. Bulte, and P. Walczak, "Survival of neural progenitors allografted into the cns of immunocompetent recipients is highly dependent on transplantation site," *Cell transplantation*, vol. 23, no. 2, pp. 253–262, 2014.
- [6] J. J. Lamanna, L. N. Urquia, C. V. Hurtig, J. Gutierrez, C. Anderson, P. Piferi, T. Federici, J. N. Oshinski, and N. M. Boulis, "Magnetic resonance imaging-guided transplantation of neural stem cells into the porcine spinal cord," *Stereotactic and functional neurosurgery*, vol. 95, no. 1, pp. 60–68, 2017.
- [7] G. E. Voerman, M. Gregorič, and H. J. Hermens, "Neurophysiological methods for the assessment of spasticity: The hoffmann reflex, the tendon reflex, and the stretch reflex," *Disability and rehabilitation*, vol. 27, no. 1-2, pp. 33–68, 2005.
- [8] H. K. Walker, "Deep tendon reflexes," in *Clinical Methods: The History, Physical, and Laboratory Examinations*, H. J. Walker HK Hall WD, Ed., Third, Butterworths, 1990, ch. 72.
- [9] S. J. Purves-Stewart, *Diagnosis of Nervous Diseases*. William and Wilkins, 1945, pp. 546–556.
- [10] W. Meinhold and J. Ueda, "Tendon tapping stimulus charecterization through contact modeling," in *ASME 2018 Dynamic Systems and Control Conference*, American Society of Mechanical Engineers, 2018.

- [11] A. Negrea and M. V. Predoi, “The elastic contact of a sphere with an elastic half-space, a comparison between analytical and finite elements solutions,” *“Politehnica” University of Bucharest. Scientific Bulletin. Series A. Applied Mathematics and Physics*, vol. 74, no. 4, pp. 69–78, 2012.
- [12] A. Wolters, A. Schmidt, A. Schramm, D. Zeller, M. Naumann, E. Kunesch, R. Bencke, K. Reiners, and J. Classen, “Timing-dependent plasticity in human primary somatosensory cortex,” *The Journal of physiology*, vol. 565, no. 3, pp. 1039–1052, 2005.
- [13] K. Kawahira, M. Shimodozono, S. Etoh, K. Kamada, T. Noma, and N. Tanaka, “Effects of intensive repetition of a new facilitation technique on motor functional recovery of the hemiplegic upper limb and hand,” *Brain Injury*, vol. 24, no. 10, pp. 1202–1213, 2010.
- [14] K. P. Blum, B. L. D’Incamps, D. Zytnecki, and L. H. Ting, “Force encoding in muscle spindles during stretch of passive muscle,” *PLoS computational biology*, vol. 13, no. 9, e1005767, 2017.
- [15] E. Kim, I. Kovalenko, L. Lacey, M. Shinohara, and J. Ueda, “Timing analysis of robotic neuromodulatory rehabilitation system for paired associative stimulation,” *IEEE Robotics and Automation Letters*, vol. 1, no. 2, pp. 1028–1035, 2016.
- [16] M. K. Chardon, W. Z. Rymer, and N. L. Suresh, “Quantifying the deep tendon reflex using varying tendon indentation depths: Applications to spasticity,” *IEEE Transactions on Neural Systems and Rehabilitation Engineering*, vol. 22, no. 2, pp. 280–289, Mar. 2014.
- [17] B. Karnath and M. Marinella, “Review of clinical signs: Woltman’s sign of hypothyroidism,” *HOSPITAL PHYSICIAN*, vol. 40, no. 1, pp. 31–32, 2004.
- [18] S. Manschot, L. van Passel, E. Buskens, A. Algra, and J. van Gijn, “Mayo and ninds scales for assessment of tendon reflexes: Between observer agreement and implications for communication,” *Journal of Neurology, Neurosurgery & Psychiatry*, vol. 64, no. 2, pp. 253–255, 1998. eprint: <http://jnnp.bmj.com/content/64/2/253.full.pdf>.
- [19] C. Marsden, P. Merton, and H. Morton, “Is the human stretch reflex cortical rather than spinal?” *The Lancet*, vol. 301, no. 7806, pp. 759–761, 1973.
- [20] K. B. Bhattacharyya, “The stretch reflex and the contributions of c david marsden,” *Annals of Indian Academy of Neurology*, vol. 20, no. 1, p. 1, 2017.
- [21] G. Cruccu, M. Aminoff, G. Curio, J. Guerit, R. Kakigi, F. Mauguiere, P. Rossini, R.-D. Treede, and L. Garcia-Larrea, “Recommendations for the clinical use of somatosensory-

- evoked potentials,” *Clinical neurophysiology*, vol. 119, no. 8, pp. 1705–1719, 2008.
- [22] L. G. Cohen, A. Starr, and H. Pratt, “Cerebral somatosensory potentials evoked by muscle stretch, cutaneous taps and electrical stimulation of peripheral nerves in the lower limbs in man,” *Brain*, vol. 108, no. 1, pp. 103–121, 1985.
- [23] A. Spitzer and D. Claus, “The influence of the shape of mechanical stimuli on muscle stretch reflexes and sep.,” *Electroencephalography and clinical neurophysiology*, vol. 85, pp. 331–336, 5 Oct. 1992.
- [24] G. Abbruzzese, A. Berardelli, J. Rothwell, B. Day, and C. Marsden, “Cerebral potentials and electromyographic responses evoked by stretch of wrist muscles in man,” *Experimental brain research*, vol. 58, no. 3, pp. 544–551, 1985.
- [25] N. Takeuchi and S.-I. Izumi, “Combinations of stroke neurorehabilitation to facilitate motor recovery: Perspectives on hebbian plasticity and homeostatic metaplasticity,” *Frontiers in human neuroscience*, vol. 9, p. 349, 2015.
- [26] D. Burke, S. C. Gandevia, and B. McKeon, “The afferent volleys responsible for spinal proprioceptive reflexes in man,” *The Journal of physiology*, vol. 339, no. 1, pp. 535–552, 1983.
- [27] G. Dawson, “Cerebral responses to electrical stimulation of peripheral nerve in man,” *Journal of neurology, neurosurgery, and psychiatry*, vol. 10, no. 3, p. 134, 1947.
- [28] R. P. Lesser, R. Koehle, and H. Lueders, “Effect of stimulus intensity on short latency somatosensory evoked potentials.,” *Electroencephalography and clinical neurophysiology*, vol. 47, no. 3, pp. 377–382, 1979.
- [29] H. H. Jasper, “The ten-twenty electrode system of the international federation,” *Electroencephalogr. Clin. Neurophysiol.*, vol. 10, pp. 370–375, 1958.
- [30] W. Meinhold, E. Kaplan, J. Ueda, T. Mori, and S.-i. Izumi, “An instrumented medical hammer with diagnostic, therapeutic and pedagogical applications,” in *ASME 2017 Dynamic Systems and Control Conference*, American Society of Mechanical Engineers Digital Collection, 2017.
- [31] W. Meinhold, S.-I. Izumi, and J. Ueda, “Automated variable stimulus tendon tapping modulates somatosensory evoked potentials,” in *2019 IEEE 16th International Conference on Rehabilitation Robotics (ICORR)*, IEEE, 2019, pp. 1025–1030.
- [32] E. Olsson and P.-L. Larsson, “A unified model for the contact behaviour between equal and dissimilar elastic–plastic spherical bodies,” *International Journal of Solids and Structures*, vol. 81, pp. 23–32, 2016.

- [33] P. Aimedieu Jr, D. Mitton, J. Faure, L. Denninger, and F. Lavaste, “Dynamic stiffness and damping of porcine muscle specimens,” *Medical engineering & physics*, vol. 25, no. 9, pp. 795–799, 2003.
- [34] J. D. Glass, N. M. Boulis, K. Johe, S. B. Rutkove, T. Federici, M. Polak, C. Kelly, and E. L. Feldman, “Lumbar intraspinal injection of neural stem cells in patients with amyotrophic lateral sclerosis: Results of a phase i trial in 12 patients,” *Stem cells*, vol. 30, no. 6, pp. 1144–1151, 2012.
- [35] L. Mazzini, F. Fagioli, R. Boccaletti, K. Mareschi, G. Oliveri, C. Olivieri, I. Pastore, R. Marasso, and E. Madon, “Stem cell therapy in amyotrophic lateral sclerosis: A methodological approach in humans,” *Amyotrophic Lateral Sclerosis and Other Motor Neuron Disorders*, vol. 4, no. 3, pp. 158–161, 2003.
- [36] M. Turkseven and J. Ueda, “An asymptotically stable pressure observer based on load and displacement sensing for pneumatic actuators with long transmission lines,” *IEEE/ASME transactions on mechatronics*, vol. 22, no. 2, pp. 681–692, 2016.
- [37] N. Hungr, C. Fouard, A. Robert, I. Bricault, and P. Cinquin, *Interventional radiology robot for ct and mri guided percutaneous interventions*, 2011.
- [38] G. S. Fischer, A. Krieger, I. Iordachita, C. Csoma, L. L. Whitcomb, and G. Fichtinger, “Mri compatibility of robot actuation techniques—a comparative study,” in *International Conference on Medical Image Computing and Computer-Assisted Intervention*, Springer, 2008, pp. 509–517.
- [39] A. Squires, J. N. Oshinski, N. M. Boulis, and Z. T. H. Tse, “Spinobot: An mri-guided needle positioning system for spinal cellular therapeutics,” vol. 46, pp. 475–487, 2018.
- [40] E. Hempel, H. Fischer, L. Gumb, T. Höhn, H. Krause, U. Voges, H. Breitwieser, B. Gutmann, J. Durke, M. Bock, *et al.*, “An mri-compatible surgical robot for precise radiological interventions,” *Computer Aided Surgery*, vol. 8, no. 4, pp. 180–191, 2003.
- [41] K. Chinzei, N. Hata, F. A. Jolesz, and R. Kikinis, “Mr compatible surgical assist robot: System integration and preliminary feasibility study,” in *International Conference on Medical Image Computing and Computer-Assisted Intervention*, Springer, 2000, pp. 921–930.
- [42] A. Melzer, B. Gutmann, T. Remmele, R. Wolf, A. Lukoscheck, M. Bock, H. Bardenheuer, and H. Fischer, “Innomotion for percutaneous image-guided interventions,” *IEEE Engineering in Medicine and Biology Magazine*, vol. 27, no. 3, pp. 66–73, 2008.

- [43] R. Monfaredi, R. Seifabadi, I. Iordachita, R. Sze, N. M. Safdar, K. Sharma, S. Fricke, A. Krieger, and K. Cleary, “A prototype body-mounted mri-compatible robot for needle guidance in shoulder arthrography,” in *5th IEEE RAS/EMBS International Conference on Biomedical Robotics and Biomechatronics*, IEEE, 2014, pp. 40–45.
- [44] R. Monfaredi, K. Cleary, and K. Sharma, “Mri robots for needle-based interventions: Systems and technology,” *Annals of biomedical engineering*, vol. 46, no. 10, pp. 1479–1497, 2018.
- [45] D. B. Comber, E. J. Barth, and R. J. Webster, “Design and control of an magnetic resonance compatible precision pneumatic active cannula robot,” *Journal of Medical Devices*, vol. 8, no. 1, p. 011 003, 2014.
- [46] C. Yiallouras, K. Ioannides, T. Dadakova, M. Pavlina, M. Bock, and C. Damianou, “Three-axis mr-conditional robot for high-intensity focused ultrasound for treating prostate diseases transrectally,” *Journal of therapeutic ultrasound*, vol. 3, no. 1, p. 2, 2015.
- [47] M. Irani, S. Peleg, *et al.*, “Motion analysis for image enhancement: Resolution, occlusion, and transparency,” *J. Visual Communication and Image Representation*, vol. 4, no. 4, pp. 324–335, 1993.
- [48] S. Peled and Y. Yeshurun, “Superresolution in mri: Application to human white matter fiber tract visualization by diffusion tensor imaging,” *Magnetic Resonance in Medicine: An Official Journal of the International Society for Magnetic Resonance in Medicine*, vol. 45, no. 1, pp. 29–35, 2001.
- [49] H. Greenspan, G. Oz, N. Kiryati, and S. Peled, “Mri inter-slice reconstruction using super-resolution,” *Magnetic resonance imaging*, vol. 20, no. 5, pp. 437–446, 2002.
- [50] K. Scheffler, “Superresolution in mri?” *Magnetic Resonance in Medicine: An Official Journal of the International Society for Magnetic Resonance in Medicine*, vol. 48, no. 2, pp. 408–408, 2002.
- [51] N. Mitsuhashi, K. Fujieda, T. Tamura, S. Kawamoto, T. Takagi, and K. Okubo, “Bodyparts3d: 3d structure database for anatomical concepts,” vol. 37, pp. D782–D785, 2009.
- [52] A. Frostell, R. Hakim, E. P. Thelin, P. Mattsson, and M. Svensson, “A review of the segmental diameter of the healthy human spinal cord,” *Frontiers in neurology*, vol. 7, p. 238, 2016.
- [53] PiezoMotor, *Piezo legs linear 6n*, ll1011D, Jan. 2019.

- [54] J. Ueda, J. A. Schultz, and H. Asada, *Cellular Actuators: Modularity and Variability in Muscle-inspired Actuation*. Butterworth-Heinemann, 2017.
- [55] D. Duncan, R. Garner, I. Zrantchev, T. Ard, B. Newman, A. Saslow, E. Wanserski, and A. W. Toga, “Using virtual reality to improve performance and user experience in manual correction of mri segmentation errors by non-experts,” *Journal of digital imaging*, vol. 32, no. 1, pp. 97–104, 2019.
- [56] F.-C. Adochiei, R.-I. Ciucu, I.-R. Adochiei, S. D. Grigorescu, G. C. Seritan, and M. Casian, “A web platform for rendering and viewing mri volumes using real-time raytracing principles,” in *2019 11th International Symposium on Advanced Topics in Electrical Engineering (ATEE)*, IEEE, 2019, pp. 1–4.
- [57] J. Kratky and J. Kybic, “Three-dimensional segmentation of bones from ct and mri using fast level sets,” in *Medical Imaging 2008: Image Processing*, International Society for Optics and Photonics, vol. 6914, 2008, p. 691 447.
- [58] J. Korhonen, M. Kapanen, J. Keyriläinen, T. Seppälä, and M. Tenhunen, “A dual model hu conversion from mri intensity values within and outside of bone segment for mri-based radiotherapy treatment planning of prostate cancer,” *Medical physics*, vol. 41, no. 1, p. 011 704, 2014.
- [59] W. Smoker, K. Berbaum, N. Luebke, and C. Jacoby, “Spatial perception testing in diagnostic radiology,” *American journal of roentgenology*, vol. 143, no. 5, pp. 1105–1109, 1984.
- [60] D. Martinez, W. Meinhold, J. Oshinski, A.-P. Hu, and J. Ueda, “Resolution-enhanced mri-guided navigation of spinal cellular injection robot,” in *2020 International Symposium on Medical Robotics (ISMR)(to appear)*, IEEE, 2020.
- [61] Victor May, *Image Super-Resolution - Iterative Back Projection Algorithm*, <https://www.mathworks.com/help/medical/creating-image-super-resolution-iterative-back-projection-algorithm.html>, [Online; accessed 9-September-2019], 2019.
- [62] B. J. Schneider, L. Doan, M. K. Maes, K. R. Martinez, A. Gonzalez Cota, N. Bogduk, and S. D. of the Spine Intervention Society, “Systematic review of the effectiveness of lumbar medial branch thermal radiofrequency neurotomy, stratified for diagnostic methods and procedural technique,” *Pain Medicine*, vol. 21, no. 6, pp. 1122–1141, 2020.
- [63] M. Scali, T. P. Pusch, P. Breedveld, and D. Dodou, “Needle-like instruments for steering through solid organs: A review of the scientific and patent literature,” *Proceedings of the Institution of Mechanical Engineers, Part H: Journal of Engineering in Medicine*, vol. 231, no. 3, pp. 250–265, 2017.

- [64] W. Meinhold, J. Oshinski, A.-P. Hu, and J. Ueda, "Design and fabrication of an automated spinal precision injection robot," *presented at the Biomedical Engineering Society Annual Meeting, Philadelphia, PA*, 2019.
- [65] W. Meinhold, D. E. Martinez, J. Oshinski, A.-P. Hu, and J. Ueda, "A direct drive parallel plane piezoelectric needle positioning robot for mri guided intraspinal injection," *IEEE Transactions on Biomedical Engineering*, vol. 68, no. 3, pp. 807–814, 2020.
- [66] S. Ambastha, S. Umesh, S. Dabir, and S. Asokan, "Comparison of force required for lumbar puncture with different gauges of spinal needle using fiber bragg grating force device," *IEEE Sensors Journal*, vol. 18, no. 19, pp. 8028–8033, 2018.
- [67] L. Tamiti, S. Braymand, N. Bahlouli, H. Jmal, and S. Facca, "Pullout strength of k-wires: Optimal solutions analysis," *Computer Methods in Biomechanics and Biomedical Engineering*, vol. 23, no. sup1, S288–S290, 2020.
- [68] Y. K. Mariappan, P. J. Rossman, K. J. Glaser, A. Manduca, and R. L. Ehman, "Magnetic resonance elastography with a phased-array acoustic driver system," *Magnetic Resonance in Medicine: An Official Journal of the International Society for Magnetic Resonance in Medicine*, vol. 61, no. 3, pp. 678–685, 2009.
- [69] G. Low, S. A. Kruse, and D. J. Lomas, "General review of magnetic resonance elastography," *World journal of radiology*, vol. 8, no. 1, p. 59, 2016.
- [70] M. Teraguchi, N. Yoshimura, H. Hashizume, S. Muraki, H. Yamada, A. Minamide, H. Oka, Y. Ishimoto, K. Nagata, R. Kagotani, *et al.*, "Prevalence and distribution of intervertebral disc degeneration over the entire spine in a population-based cohort: The wakayama spine study," *Osteoarthritis and cartilage*, vol. 22, no. 1, pp. 104–110, 2014.
- [71] W. C. Chan, K. L. Sze, D. Samartzis, V. Y. Leung, and D. Chan, "Structure and biology of the intervertebral disk in health and disease," *Orthopedic Clinics*, vol. 42, no. 4, pp. 447–464, 2011.
- [72] B. A. Walter, P. Mageswaran, X. Mo, D. J. Boulter, H. Mashaly, X. V. Nguyen, L. M. Prevedello, W. Thoman, B. D. Raterman, P. Kalra, *et al.*, "Mr elastography-derived stiffness: A biomarker for intervertebral disc degeneration," *Radiology*, vol. 285, no. 1, pp. 167–175, 2017.
- [73] E. I. Ben-Abraham, J. Chen, J. P. Felmlee, P. Rossman, A. Manduca, K.-N. An, and R. L. Ehman, "Feasibility of mr elastography of the intervertebral disc," *Magnetic resonance imaging*, vol. 39, pp. 132–137, 2017.

- [74] G. O’connell, E. Vresilovic, and D. Elliott, “Comparative intervertebral disc anatomy across several animal species,” in *52nd Annual Meeting of the Orthopaedic Research Society*, 2006.
- [75] C. Vergari, P. Rouch, G. Dubois, D. Bonneau, J. Dubousset, M. Tanter, J.-L. Gennison, and W. Skalli, “Non-invasive biomechanical characterization of intervertebral discs by shear wave ultrasound elastography: A feasibility study,” *European radiology*, vol. 24, no. 12, pp. 3210–3216, 2014.
- [76] K. Uffmann and M. E. Ladd, “Actuation systems for mr elastography,” *IEEE Engineering in medicine and biology magazine*, vol. 27, no. 3, pp. 28–34, 2008.
- [77] Z. T. H. Tse, Y. J. Chan, H. Janssen, A. Hamed, I. Young, and M. Lamperth, “Piezo-electric actuator design for mr elastography: Implementation and vibration issues,” *The International Journal of Medical Robotics and Computer Assisted Surgery*, vol. 7, no. 3, pp. 353–360, 2011.
- [78] C. J. Lewa, M. Roth, L. Nicol, J.-M. Franconi, and J. D. de Certaines, “A new fast and unsynchronized method for mri of viscoelastic properties of soft tissues,” *Journal of Magnetic Resonance Imaging*, vol. 12, no. 5, pp. 784–789, 2000.
- [79] C. L. Johnson and E. H. Telzer, “Magnetic resonance elastography for examining developmental changes in the mechanical properties of the brain,” *Developmental cognitive neuroscience*, vol. 33, pp. 176–181, 2018.
- [80] T. Numano, Y. Kawabata, K. Mizuhara, T. Washio, N. Nitta, and K. Homma, “Magnetic resonance elastography using an air ball-actuator,” *Magnetic resonance imaging*, vol. 31, no. 6, pp. 939–946, 2013.
- [81] W. Neumann, L. R. Schad, and F. G. Zöllner, “A novel 3d-printed mechanical actuator using centrifugal force for magnetic resonance elastography,” in *2017 39th Annual International Conference of the IEEE Engineering in Medicine and Biology Society (EMBC)*, IEEE, 2017, pp. 3541–3544.
- [82] K. Uffmann, C. Abicht, W. Grote, H. H. Quick, and M. E. Ladd, “Design of an mr-compatible piezoelectric actuator for mr elastography,” *Concepts in Magnetic Resonance: An Educational Journal*, vol. 15, no. 4, pp. 239–254, 2002.
- [83] J. Chen, C. Ni, and T. Zhuang, “Imaging mechanical shear waves induced by piezo-electric ceramics in magnetic resonance elastography,” *Chinese science bulletin*, vol. 51, no. 6, pp. 755–760, 2006.
- [84] A. Arani, A. Eskandari, P. Ouyang, and R. Chopra, “A novel high amplitude piezo-ceramic actuator for applications in magnetic resonance elastography: A compliant mechanical amplifier approach,” *Smart Materials and Structures*, vol. 26, no. 8,

p. 087 001, 2017.

- [85] S. Molladavoodi, J. McMorran, and D. Gregory, “Mechanobiology of annulus fibrosus and nucleus pulposus cells in intervertebral discs,” *Cell and tissue research*, vol. 379, no. 3, pp. 429–444, 2020.
- [86] P. Mott and C. Roland, “Limits to poisson’s ratio in isotropic materials,” *Physical review B*, vol. 80, no. 13, p. 132 104, 2009.
- [87] W. Kratzer, V. Fritz, R. A. Mason, M. M. Haenle, V. Kaechele, and R. S. Group, “Factors affecting liver size: A sonographic survey of 2080 subjects,” *Journal of ultrasound in medicine*, vol. 22, no. 11, pp. 1155–1161, 2003.
- [88] W. Meinhold, E. Ozkaya, J. Ueda, and M. Kurt, “Tuneable resonance actuators for magnetic resonance elastography,” in *2019 Design of Medical Devices Conference*, American Society of Mechanical Engineers Digital Collection, 2019.
- [89] G. Waterstraat, R. Körber, J.-H. Storm, and G. Curio, “Noninvasive neuromagnetic single-trial analysis of human neocortical population spikes,” *Proceedings of the National Academy of Sciences*, vol. 118, no. 11, 2021.
- [90] W. Meinhold and J. Ueda, “Tendon tapping location detection through impact modeling,” in *2019 International Symposium on Medical Robotics (ISMR)*, IEEE, 2019, pp. 1–7.

VITA

Waiman Meinhold was born in Santa Barbara, California. He attended UC Berkeley where he obtained a B.S in Mechanical Engineering while working in the laboratories of Professor Ruzena Bajcsy and Professor Masayoshi Tomizuka. He moved to Atlanta in 2016 to join the Biorobotics and Human Modeling Laboratory, advised by Professor Jun Ueda.